CHEMO-MECHANICS OF FUNCTIONAL THIN FILMS FOR LITHIUM-ION BATTERIES AND NEUROMORPHIC COMPUTING DEVICES

A Thesis

by

YUWEI ZHANG

Submitted to the Office of Graduate and Professional Studies of
Texas A&M University
in partial fulfillment of the requirements for the degree of

DOCTOR OF PHILOSOPHY

Chair of Committee,	Matt Pharr
Committee Members,	Sarbajit Banerjee
	Ying Li
	Choongho Yu
Head of Department,	Andreas A. Polycarpou

May 2021

Major Subject: Mechanical Engineering

ABSTRACT

This thesis investigates chemo-mechanics of functional thin films for lithium-ion batteries and neuromorphic computing devices. We provide synthesis details of several functional thin films, including textured V_2O_5, textured VO_2, epitaxial VO_2 (020), epitaxial VO_2 ($\bar{4}02$) and analyze their evolution of mechanical, structural, and chemical properties when subjected to external stimuli. Regarding batteries, we focus on two cathode systems: Li-S composites and sputtered V_2O_5 thin films. We monitor the evolution of stresses in both systems during electrochemical cycling and link these stresses to structural and morphological evolution. These studies provide insight into mechanics-based issues in high-capacity cathodes with an eye toward strategies that mitigate mechanical degradation and thus extend cycle lifetimes. Regarding neuromorphic computing devices, we investigate sputtered VO_2 thin films in the view of crystal structure and corresponding effects on mechanical behavior. We conduct in-operando measurements of stress and nanoindentation in VO_2 thin films as they undergo metal-insulator phase transitions during thermal cycling. We observe that tensile stresses develop in the film upon heating through the phase transformation, which is somewhat counterintuitive given the known volumetric expansion associated with this transformation. We explain this phenomenon through structural analysis. The experiments also indicate a critical film thickness (of around 600 nm) above which polycrystalline VO_2 thin films will fracture. A corresponding fracture mechanics analysis of thin films captures this observed phenomenon. Overall, our detailed mechanical investigation can provide guidance towards practical implementation of mechanically-robust VO_2 into devices.

ACKNOWLEDGEMENTS

I would like to thank my committee chair, Dr. Matt Pharr, and my committee members, Dr. Banerjee, Dr. Li and Dr. Yu, for their guidance and support throughout my Ph.D. period.

Thanks also go to my friends and colleagues and the department faculty and staff for making my time at Texas A&M University a great experience.

Finally, thanks to my mother and father for their encouragement for their patience and love.

CONTRIBUTORS AND FUNDING SOURCES

Contributors

This work was supervised by a thesis committee Professor Matt Pharr of the Department of Mechanical Engineering.

The XRD and Raman data analyzed for Chapter II and Chapter IV were conducted in part by Yuting Luo of the Department of Chemistry.

Nanoindentation data for Chapter V was conducted by Graduate student Cole D. Fincher of the Department of Mechanical Engineering.

XRD data analyzed for Chapter V was conducted in part by Rebeca M. Gurrola of the Department of Material Science and Engineering.

XPS data analyzed for Chapter V was conducted by Jungho Shin of the Department of Mechanical Engineering.

All other work conducted for the thesis (or) dissertation was completed by the student independently.

Funding Sources

Y. Zhang was supported by the Hagler Institute for Advanced Study (HIAS) at Texas A&M University.

Y. Zhang was supported by funding from the mechanical engineering department at Texas A&M University and the Texas A&M Engineering Experiment Station (TEES).

Y. Zhang was supported by the X-Grants Program: A President's Excellence Fund at Texas A&M University.

TABLE OF CONTENTS

Page

LIST OF FIGURES

CHAPTER I

INTRODUCTION

Battery chemistries beyond lithium-ion are required to meet growing demands for economic and sustainable energy storage/conversion for grid-scale energy storage, portable electronics, and electric vehicles. The vast majority of studies on Li-ion batteries have focused on improving their electrochemical characteristics. Mechanics-based issues have been largely overlooked or under-studied. Moreover, of the existing mechanics-based studies, relatively few have targeted cathode materials, likely due to their small volume expansion (~2-8%), compared to those of anodes (up to ~300%).[1–8] However, it is important to note that a strain larger than 0.1-1% is considered severe for brittle materials, such as are many of the cathode materials.[1] Thus, stresses generated during electrochemical cycling may result in fragmentation, disintegration and fracturing, and/or loss of contact to the current collectors, all of which can lead to severe capacity fade.[9–15] Indeed, even volume changes during electrochemical cycling of commercialized cathode materials, such as $LiCoO_2$ (2.6% volume change), $LiFePO_4$ (6.8% volume change), and $LiMnO_2$ (7.5% volume change) have been shown to produce mechanical degradation.[1–6,16] Herein, we investigate electro-chemo-mechanics of two promising high-capacity cathode materials: V_2O_5 and S.

Lithium sulfur battery

Sulfur has emerged as a leading candidate to replace conventional cathodes primarily due to its enormous capacity (1672 mAh/g), which is an order of magnitude larger than existing transition-metal cathodes (e.g., 272 mAh/g for $LiCoO_2$).[17–21] Combined with its abundance in the earth's crust, sulfur cathodes represent a promising low cost, light weight, and sustainable option for the next-generation of battery electrodes.[22–27] In addition to electrochemical mechanisms of degradation, sulfur cathodes may also be prone to mechanical degradation. In particular, an enormous volume expansion of ~80% accompanies the conversion of S to Li_2S.[18,19,21] Large volume expansions have resulted in mechanical degradation and corresponding capacity losses in many other electrode materials, such as $LiCoO_2$,[15] Si,[12,13,28–33] Ge,[34–36] graphite[37,38], and $LiMn_2O_4$[39,40], V_2O_5[41], among others. However, sulfur cathodes exhibit fundamentally distinct behavior in that previously studied electrodes remain in solid form throughout cycling during intercalation or conversion reactions, whereas sulfur undergoes solid-to-liquid, liquid-to-liquid, and liquid-to-solid phase transformations. The influence of such phase transformations on mechanics (e.g., stress levels) is unknown but could be significant given the predicted large volume changes during conversion reactions between S and Li_2S.

To fill these gaps in knowledge, we aim to provide fundamental understanding of mechanics in composite sulfur cathodes. To this end, we perform in-situ measurements of mechanical stresses generated during electrochemical cycling of composite sulfur cathodes. Additionally, we correlate these stresses to electrochemical, structural, and phase evolution via combined scanning electron microscopy (SEM), energy dispersive spectroscopy (EDS), and x-ray diffraction (XRD). These efforts offer insight into basic mechanisms underpinning structural changes and their ramifications in terms of mechanical degradation during electrochemical cycling of composite sulfur cathodes.

V_2O_5 thin film battery

Vanadium oxide (V_2O_5) is a promising material for next-generation cathodes and can be stabilized as different polymorphs with varying atomic connectivities.[42–47] Indeed, recent studies have suggested that several polymorphs of V_2O_5 are ideal candidates for hosting multivalent metal-ions with large volumes while maintaining excellent electrochemical performance.[48–51]

Likewise, ion-stabilized V_2O_5 with large interlayer spacing has shown enhanced electrochemical performance using pre-intercalation.[50,52–56] The theoretical capacity of V_2O_5 is an enormous 442 mAh/g, as it can host up to 3 Li atoms per formula unit (V_2O_5).[43,47] However, the extent of reversible intercalation has been found to be much lower.[43] The crystal structure of V_2O_5 remains intact if a voltage window is set such that cycling occurs only between the orthorhombic α-V_2O_5 and the δ-$Li_xV_2O_5$ phase.[43,44] As such, pristine α-V_2O_5 presents a model system to study discharging/charging-induced mechanical loading during electrochemical cycling, potentially without conflating the influence of crystal structure degradation.

To this end, we investigated the electrochemical and mechanical performance of V_2O_5 cathodes during electrochemical cycling. To deconvolute the influence of binders and carbon matrices on their mechanical response (i.e., to measure intrinsic properties of V_2O_5), we fabricated dense textured thin films of V_2O_5 by plasma sputtering. We then performed in-situ measurements of mechanical stresses generated during cycling under various electrochemical conditions. Post-mortem observation of samples cycled to different extents allowed for understanding the damage evolution in these systems. Likewise, we investigated the evolution of electrochemical properties, crystal structure, and morphology during extended cycling. Overall, this study links electrochemical, structural, and mechanical observations to develop mechanistic understanding of the root cause of capacity fade in V_2O_5 cathodes of Li-ion batteries.

Neuromorphic computing devices

Electron-correlated transition metal oxides exhibiting pronounced metal-insulator transitions (MIT) are excellent candidates to emulate the spiking behavior of biological neurons. VO_2 undergoes a first-order diffusionless and hysteretic transition from high-symmetry rutile phase R to low-symmetry stable M_1 (or metastable M_2/M_3) phase around T_c=340K.[57–61] Stemming from this behavior, Yi *et al.* demonstrated 23 types of biological neuronal behaviors through two channel devices of VO_2 as active memristors[62]. Much attention has already focused on tuning the transition temperature for various application.[63–66] However, VO_2 often suffers severe mechanical damage during thermal cycle.[67–73] Implementation of VO_2 into robust devices of practical utility requires a comprehensive understanding of the mechanical properties, as to ensure extended service life.

In this study, we performed nanoindentation on sputter-deposited thin films of VO_2 in both the VO_2-M (at room temperature) and VO_2-R (at 85°C) phases. We then used a multi-beam optical stress sensor to track the evolution of stress in-situ during thermal cycling. Informed by the elastic modulus E_f and accumulated stress σ_f during the thermal cycle, we implemented an analysis from fracture mechanics to predict a critical film thickness, below which no fracture will occur. We compared these predictions to experimental observations in the same system. We also investigated the effect of heating rate and cycle characteristics on the stress history. Finally, we performed some extended cycling testing to observe stress evolution and potential damage evolution in this system. Overall, we believe that our detailed studies from a mechanical perspective provide insight into the design of mechanically robust neuromorphic computing devices.

CHAPTER II

IN-SITU MEASUREMENTS OF STRESS EVOLUTION IN COMPOSITE SULFUR CATHODES[1]

Abstract

Owing to their enormous capacities, Li-S batteries have emerged as a prime candidate for economic and sustainable energy storage. Still, potential mechanics-based issues exist that must be addressed: lithiation of sulfur produces an enormous volume expansion (~80%). In other high-capacity electrodes, large expansions generate considerable stresses that can lead to mechanical damage and capacity fading. However, the mechanics of electrochemical cycling of sulfur is fundamentally distinct from other systems due to solid-to-liquid, liquid-to-liquid, and liquid-to-solid phase transformations, and thus remains poorly understood. To this end, we measure the evolution of stresses in composite sulfur cathodes during electrochemical cycling and link these stresses to structural evolution. We observe that nucleation and growth of solid lithium-sulfur phases induces significant stresses, including irreversible stresses from structural rearrangements during the first cycle. However, subsequent cycles show highly reversible elastic mechanics, thereby demonstrating strong potential for extended cycling in practical applications.

Introduction

Battery chemistries beyond lithium-ion are required to meet growing demands for economic and sustainable energy storage/conversion for grid-scale energy storage, portable electronics, and

---

[1] Reprinted with permission from "In-Situ Measurements of Stress Evolution in Composite Sulfur Cathodes" by Yuwei Zhang, Yuting Luo, Coleman Fincher, Scott McProuty, Garrett Swenson, Sarbajit Banerjee, Matt Pharr. Energy Storage Materials 16 (2019): 491-497. Copyright (2019).

electric vehicles. Sulfur has emerged as a leading candidate to replace conventional cathodes primarily due to its enormous capacity (1672 mAh/g), which is an order of magnitude larger than existing transition-metal cathodes (e.g., 272 mAh/g for $LiCoO_2$).[17–21] Combined with its abundance in the earth's crust, sulfur cathodes represent a promising low cost, light weight, and sustainable option for the next-generation of battery electrodes.[22–27]

Previous studies have implemented a number of *in-situ* techniques to study the electrochemistry and speciation of discharge products in lithium-sulfur batteries, including x-ray absorption near-edge spectroscopy (XANES)[74], electron paramagnetic resonance (EPR)[75], nuclear magnetic resonance (NMR)[76], Raman[77–79], UV/Vis spectroscopy[80,81], x-ray diffraction (XRD)[82–85], and x-ray fluorescence microscopy (XRF).[86] These studies have elucidated a range of electrochemical issues that cause degradation of the sulfur battery, most notably the shuttling of electrolyte-soluble polysulfides that leads to loss of active material,[87–92] the clogging of porous cathode architectures, and the electronically insulating nature of both S and Li_2S that results in poor kinetics and utilization of active material.[93–96]

In addition to electrochemical mechanisms of degradation, sulfur cathodes may also be prone to mechanical degradation. In particular, an enormous volume expansion of ~80% accompanies the conversion of S to Li_2S.[18,19,21] Large volume expansions have resulted in mechanical degradation and corresponding capacity losses in many other electrode materials, such as $LiCoO_2$,[15] Si,[12,13,28–33] Ge,[34–36] graphite[37,38], and $LiMn_2O_4$[39,40], V_2O_5[41], among others. However, sulfur cathodes exhibit fundamentally distinct behavior in that previously studied electrodes remain in solid form throughout cycling during intercalation or conversion reactions, whereas sulfur undergoes solid-to-liquid, liquid-to-liquid, and liquid-to-solid phase transformations. The influence of such phase transformations on mechanics (e.g., stress levels) is unknown but could be significant given the predicted large volume changes during conversion reactions between S and Li_2S.

To fill these gaps in knowledge, this paper aims to provide fundamental understanding of mechanics in composite sulfur cathodes. To this end, we perform in-situ measurements of mechanical stresses generated during electrochemical cycling of composite sulfur cathodes. Additionally, we correlate these stresses to electrochemical, structural, and phase evolution via combined scanning electron microscopy (SEM), energy dispersive spectroscopy (EDS), and x-ray diffraction (XRD). These efforts offer insight into basic mechanisms underpinning structural changes and their ramifications in terms of mechanical degradation during electrochemical cycling of composite sulfur cathodes.

Materials and methods

Cell preparation

We prepared sulfur-carbon composite cathodes through a spin coating process, with compositions of 50 wt.% sulfur nanoparticles (99.99% US Research Nanomaterials Inc.) as the active material, 40 wt.% TIMCAL Graphite & Carbon Super P (MTI Corporation) as the matrix, and 10 wt.% polyvinylidene fluoride (PVDF, MTI Corporation) as the binder. We created a dispersion of these components in *N*-methyl-2-pyrrolidone (NMP, MTI Corporation), followed by magnetic stirring for 3 h. Lastly, we spin-coated the prepared slurry at 1000 rpm for 1 min onto mirror-finished T304 stainless steel substrates (Metals Depot). After spin coating, we dried the resulting film at 45°C for 3 h. We used a profilometer (Veeco Dektak 150 Profilometer) to measure the thickness of composite sulfur cathode.

A two-electrode electrochemical test cell with a quartz window (MTI Corporation) facilitated simultaneous electrochemical and mechanical measurements, as depicted in Figure 1. We assembled this cell in an argon-filled glovebox with oxygen and moisture levels below 0.1 ppm. In addition to the sulfur composite working electrode described above, the battery consisted of a lithium metal ribbon (99.9% trace metals basis, Sigma-Aldrich) anode and a Celgard 2400 separator (MTI Corporation). The electrolyte was 1.0 M lithium *bis*-trifluoromethanesulphonylimide (LiTFSI, Sigma-Aldrich) in (1:1 v/v) 1,3-dioxolane (DOL, Sigma-Aldrich): 1,2-dimethoxyethane (DME, Sigma-Aldrich), with the addition of 0.5 wt.% $LiNO_3$ as an additive (Sigma-Aldrich). After assembly, we rested the cell for 8 h prior to electrochemical and mechanical testing to remove the influence of binder swelling on the stress measurements.

Structural characterization

X-ray diffraction patterns during cycling were collected in a Bragg-Brentano geometry using a Brucker D-8 Discovery diffractometer equipped with a Lynxeye detector (25 kV, 40 mA). After discharging/charging to the desired voltage or state of stress, we disassembled the cells inside the glovebox and washed the sulfur cathodes with anhydrous DME to remove any remaining polysulfides. Since the samples were sensitive to moisture and oxygen, we masked the samples with Kapton™ tape prior to removal from glovebox. A Cu Kα radiation source produced the XRD data, recording between 20 and 35° at a scan rate of 0.0083° s^{-1}.

Scanning electron microscopy (SEM, JEOL JSM-7500F) coupled with energy-dispersive x-ray spectroscopy (EDX, Oxford Instruments) enabled characterizing changes in surface morphology and elemental composition of the sulfur cathodes during cycling. As with the XRD measurements, we cleaned the samples with anhydrous DME prior to examination. Sealing the sample in Static-Shielding Press-to-Close Bags (McMaster-Carr) prevented contamination during transportation to SEM chamber.

Electrochemical measurements

Using a PARSTAT MC Multichannel Potentiostat (Princeton Applied Research), we conducted galvanostatic cycling at a C/10 rate between 2.8 V - 1.5 V vs Li/Li^+. [17,18] The C rate is based on the theoretical capacity of sulfur (1672 mAh/g).[17–19] All experiments were conducted at room temperature (25°C).

Mechanical characterization

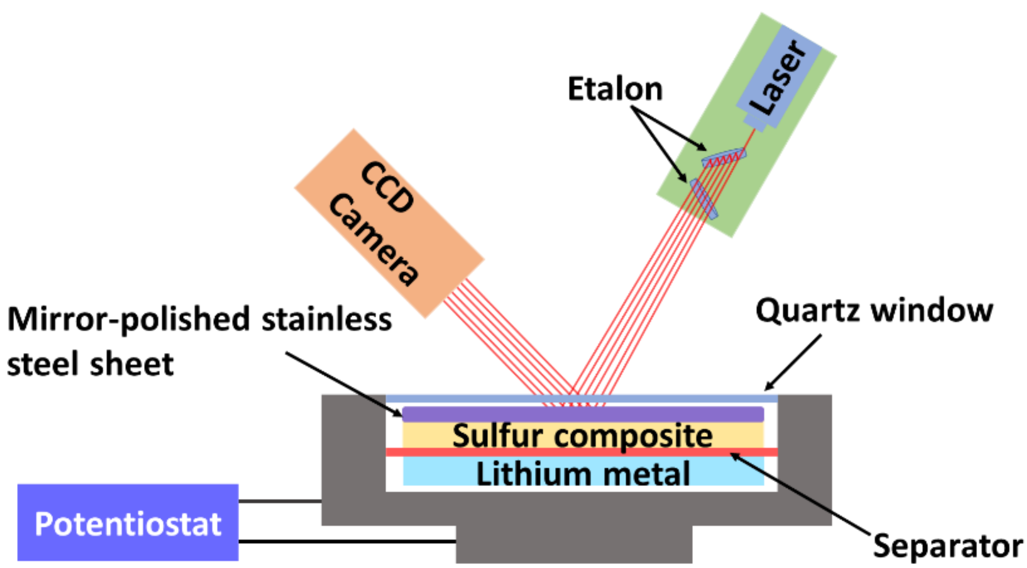

Figure 1 A schematic representation of the electrochemical setup, using a split cell with a quartz viewing window, in which in-situ multibeam optical sensing enables measurements of stress during electrochemical cycling.

A multibeam optical stress sensor (MOS) from k-Space Associates monitored the change in curvature of the sulfur cathode (ΔK) during electrochemical cycling, as shown in Figure 1. To measure this curvature, the MOS employs an array of laser beams that enables simultaneous illumination and detection, thereby greatly reducing noise caused by fluid motion in the electrochemical cell or by ambient vibrations. The cell was also placed on an antivibration table during testing. To account for the various media through which the laser beam passes in our setup (e.g., the air and quartz window), we calibrated the system using a calibration mirror (radius of curvature of 10 m) inside the electrochemical cell. Using Stoney's equation, we deduced the stress change within the composite cathode during cycling[97,98],

$$\Delta\sigma = \frac{E_s\, h_s^2}{6h_f(1-\nu_s)}\Delta K,$$

where E_s is the elastic modulus of the substrate(E_s= 203 GPa), h_s is the thickness of the substrate(h_s= 736 μm), ν_s is the Poisson's ratio of the substrate($\upsilon_{s= 0.29}$), and h_f is the thickness of electrode film (h_f= 70.3 μm) (measured via profilometry before the test). In this study, we take h_f as constant, such that the stress calculated is the nominal in-plane stress. Likewise, previous studies have shown that the thickness change is negligible for porous composite thin films fabricated through slurry deposition methods.[37,99–101] We also measured the thickness change before and after the lithiation, and found the variation to be negligible. Table 1 shows the values of parameters used in the above equation.

Results and discussion

Structural evolution during electrochemical cycling

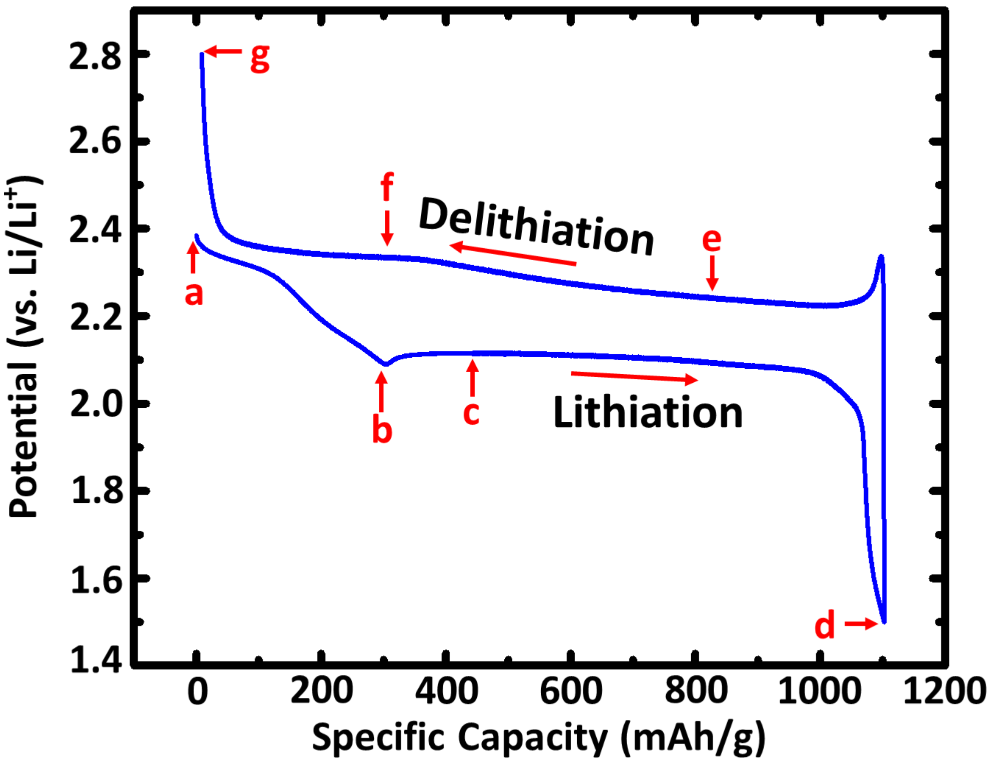

Figure 2 Representative potential response of a composite sulfur electrode during galvanostatic electrochemical cycling.

The cycling curve shown in Figure 2 highlights the complex compositional changes that occur during the charge/discharge process. Point (a) represents the state of the battery prior to any discharging. Points (b), (d), (f) and (g) are chosen based on notable electrochemical features, while points (c) and (e) are chosen based on mechanical features of interest to be discussed later. This cycling process, involving a series of phase discontinuities, is substantially more complex than found in many other cathode materials, i.e., in many others, simple intercalation/de-intercalation of lithium occurs during cycling.[15,37–40,102] To fully understand this complicated cycling process, we charged/discharged the composite sulfur cathodes to various extents while measuring the evolution of stresses and performed complementary structural characterization using SEM, EDS, and XRD.

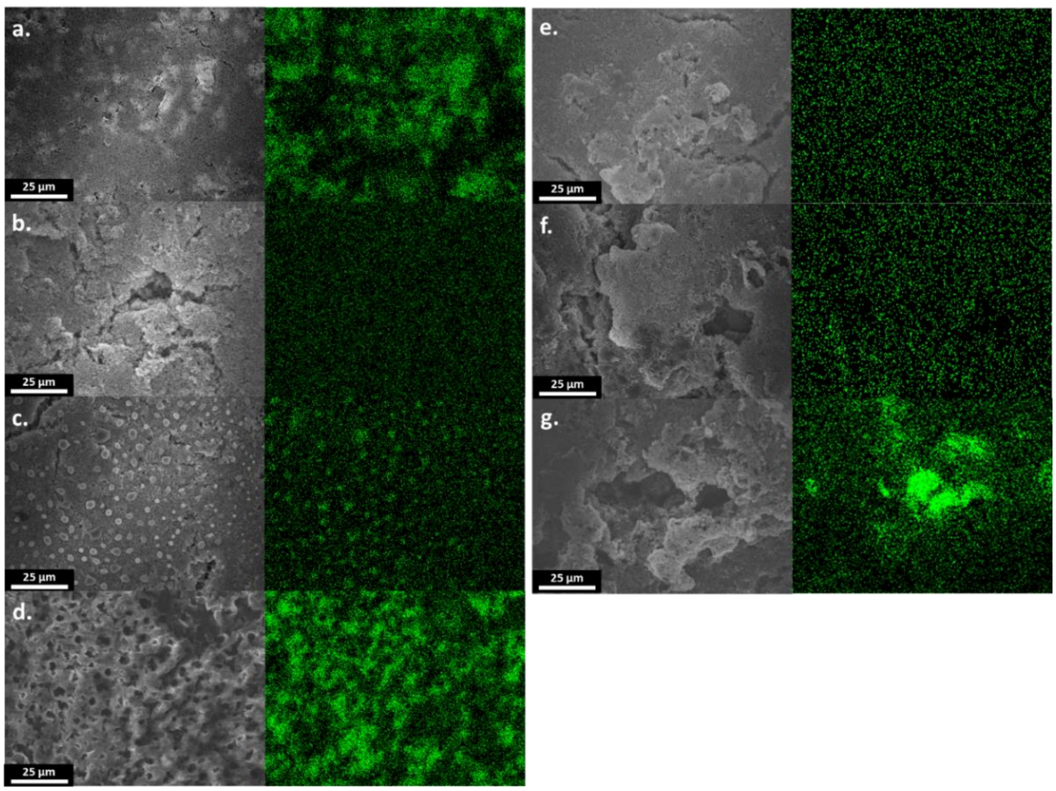

Figure 3 SEM and EDS images of a sulfur cathode at different states of charge during the first cycle. The green color in the EDS images indicates the presence of sulfur. The letters correspond to the states labeled in Figure 2, as follows: a) pristine sulfur composite prior to any discharge), b) at the beginning of the lower voltage plateau (2.1 V) during lithiation, c) one special point at the lower voltage plateau during lithiation, d) at the end of lithiation, e) one special point during de-lithiation f) at the beginning of the voltage plateau (2.33V) during de-lithiation g) at the end of de-lithiation.

Figure 3 shows SEM images and EDS maps of the surfaces of sulfur composite cathodes charged/discharged to the corresponding labels in Figure 2. We thoroughly rinsed the samples with dimethyl ether (DME) inside a glovebox prior to analysis by SEM. As a result, the SEM images only show the solid phases. Likewise, Figure 4 shows the XRD patterns of sulfur composite cathodes charged/discharged to the same extents corresponding to the labels in Figure 2. From Figure 3a, the pristine sulfur composite cathode appeared as a near-uniform film composed of a homogeneous mixture of sulfur, carbon, and PVDF. The corresponding XRD pattern at point (a) indicates that sulfur is crystalline orthorhombic α-sulfur prior to lithiation (Figure 4, label a). As the sulfur converted into electrolyte-soluble polysulfides near the beginning of lower discharge voltage plateau, a substantial portion of the sulfur disappeared, leaving voids within the carbon matrix (Figure 3b). Correspondingly, the XRD reflections disappeared, indicating the dissolution and electrochemical conversion of sulfur (Figure 4, label b). With further lithiation, solid products nucleated on the carbon matrix as small islands (Figure 3c). However, the corresponding XRD reflections provide no evidence of a crystalline phase (Figure 4, label c). Combining these observations suggests that a solid phase of either Li_2S_2 or Li_2S first formed as an amorphous phase. At the end of lithiation, the surface was almost entirely covered by solid-phase growth products (Figure 3d), similar to a previous study.[103] The corresponding XRD pattern shows new reflections, which can be indexed to the emergence of crystalline Li_2S (Figure 4, label d). Overall, these observations indicate that lithiation of sulfur involves dissolution of sulfur into electrolyte-soluble polysulfides, followed by thin film nucleation and growth of solid phases (between points b and d).

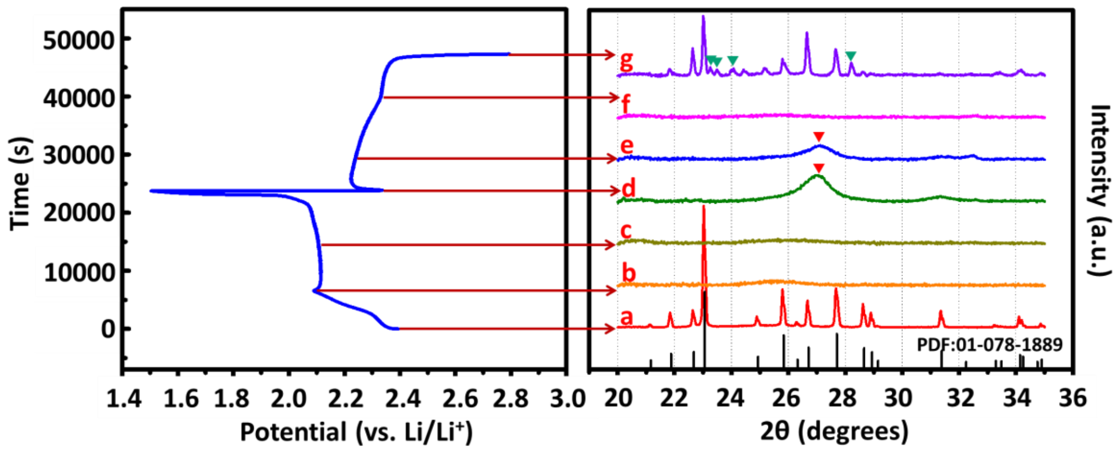

Figure 4 XRD patterns of a sulfur cathode at different potentials during the first cycle. The red triangles indicate a peak corresponding to Li_2S (PDF number: 00-026-1188). The green triangles indicate peaks corresponding to monoclinic sulfur (β-sulfur) (PDF number: 01-071-0137). The PDF shown in black (PDF number: 01-078-1889) corresponds to orthorhombic sulfur (α-sulfur).

Figures 3e-3g and Figures 4e-4g show the evolution of the cathode surface and corresponding phase changes during de-lithiation. Between point (d) and (e), the dissolution of the solid lithiated phases began, as indicated by a reduction in the sulfur signal from EDS (Figure 3e). The intensity of the peak corresponding to crystalline Li_2S concomitantly decreased significantly (Figure 4, label e), likewise indicating the dissolution of solid crystalline phases. By the time the charging plateau (2.33 V) was reached at point (f), most of the solid lithiated phases had dissolved, and the carbon matrix was clearly visible (Figure 3f). Moreover, no solid phase of crystalline Li_2S remained according to the XRD results (Figure 4, label f). At the end of de-lithiation (Figure 3g), solid sulfur appeared to re-deposit on the matrix, similar to previous studies.[84,85,103–105] At this point, the XRD patterns corresponding to both orthorhombic α-sulfur and monoclinic β-sulfur appeared (Figure 4, label g), indicating the presence of both polymorphs, consistent with other studies. [83,85] This incipient polymorphism of the deposited sulfur, reflecting the deposition of a metastable phase under conditions away from equilibrium, contributes to the significant difference in morphology before and after the first cycle (Figure 3a and Figure 3g).

Measurements of stress evolution during electrochemical cycling

Figure 1 shows the experimental setup used to measure stress changes during electrochemical cycling of composite sulfur cathodes. A multibeam optical stress sensor (MOS) monitored the change in curvature of the sulfur cathode (ΔK) during electrochemical cycling. The results from MOS measurements are shown in Figure 5 to Figure 7. Figure 5 shows the changes in stress in the sulfur composite cathode during the first five cycles of galvanostatic charge/discharge. We should note that these stresses represent the average stress in the composite film during cycling; they do not provide locally differentiable information (e.g., stress in sulfur *vs*. stress in PVDF). However, these measurements provide useful information regarding the overall mechanics in the system during electrochemical cycling. The stress generated during these five cycles was quite repeatable from cycle to cycle with the exception of the first cycle, i.e., barring the first cycle, features occurred at similar depths of discharge and with similar magnitudes in each cycle. We conducted multiple additional tests to confirm these trends. The first cycle may be different from the others due to the eight-hour resting period, e.g., the upper voltage plateau does not occur during the first cycle as seen in other studies.[17–21] However, this rest period is necessary to ensure that the binder swelling does not contribute significantly to stress measurements, as noted by Sethuraman et *al*. in a previous study.[37] As a result, binder swelling and/or self-discharge during the resting period may have produced stresses not accounted for here. Correspondingly, the hysteretic change in stress (apparently toward residual tensile stresses) during the first cycle may not be as significant as indicated, as attributed to stress generated during the resting period. Still, our results suggest that hysteretic stresses may occur during the first cycle, likely due to plastic deformation and/or structural evolution (e.g., as in comparing Figure 3a to 3g).

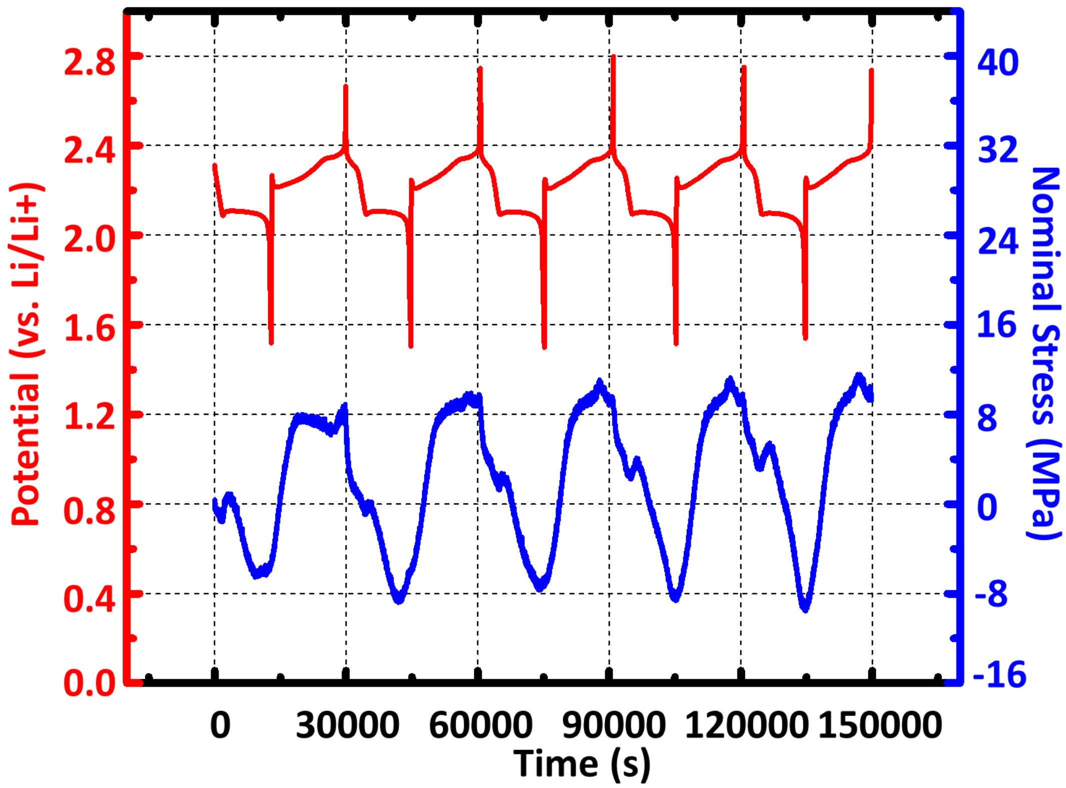

Figure 5 Potential and corresponding stress response during cycling of a composite sulfur cathode.

Additionally, the stresses generated here are substantial but are significantly smaller than those observed in other high-capacity systems, such as Si[12,106] and Ge[35]. These stresses are comparatively small for a number of reasons, due to both the composite nature of this cathode and likely intrinsic to sulfur itself. First, this cathode is a composite that employs relatively compliant binders, which tend to reduce stress levels compared to that intrinsic to the pure active material as has been demonstrated in other systems. For instance, Sethuraman *et al*. reported the yield stress in a silicon composite anode of 12 MPa (using PVDF as binder), which is approximately 100x smaller than the 1.25 GPa reported for a pure (binder-free) silicon thin film.[100,107] Additionally, composites with relatively compliant binders exhibit low stresses, e.g., as found in comparing the stress levels in a composite silicon anode battery using CMC (70 MPa) and PVDF (12 MPa) as binders.[100] Second, this composite has a porosity of nearly 30%. Thus, stresses are largely accommodated by growth into the pores of the structure, reducing the stresses that are generated, i.e., some stress-free strains occurred. As a result, denser sulfur cathodes will undoubtedly suffer from even larger stresses, which underscores the importance of microstructural/geometric design of sulfur cathodes to prevent mechanical damage. Additionally, these relatively small stresses likely have some contributions from processes intrinsic to sulfur. In particular, lithiation/de-lithiation of sulfur produces solid-to-liquid and liquid-to-solid phase transformations, distinct from other high-capacity systems (e.g., Si[12,106] and Ge[35]). As determined in this study, these solid-to-liquid and liquid-to-solid transformations occur by dissolution and thin film-growth-type-processes, respectively. These types of transformations likely produce intrinsically smaller stresses than occur in systems that undergo purely solid-phase-growth, such as in Si[12,106] and Ge[35].

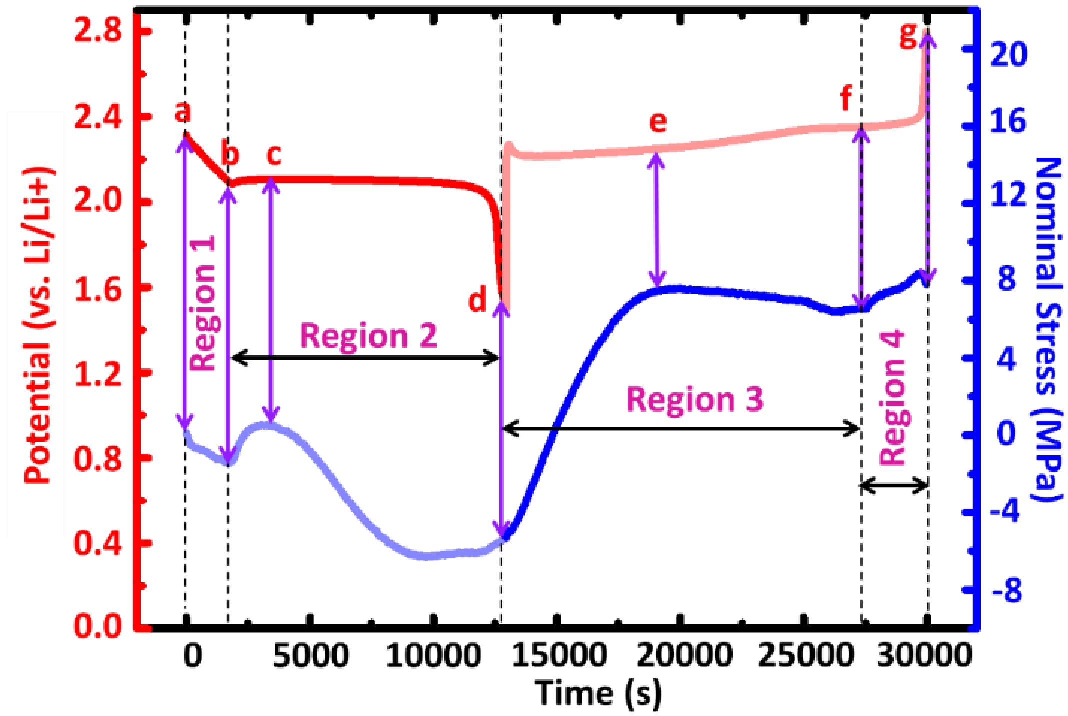

Figure 6 Potential and corresponding stress response during the initial cycle of a composite sulfur cathode.

To further highlight specific details of the mechanics, Figure 6 displays a zoomed-in view of the stress evolution during the first cycle. The stresses presented represent changes in stress relative to a reference stress, which we take as the stress at the beginning of the first discharge. To reiterate, the upper voltage plateau during lithiation is absent due to self-discharging during the resting period. Thus, along with residual stress in the film from the fabrication process, the choice of reference state may influence the absolute value of the stress. As seen in Figure 6, lithiation of the cathode lead to at least two different types of mechanical behavior. In Region 1, the conversion of solid sulfur into liquid polysulfides produced compression relative to our reference state. In this region, the dissolution of solid sulfur removed residual stresses from fabrication and resting (which were apparently tensile here). Next, the stresses generated in

Region 2 reflect typical stress evolution during thin film nucleation and growth processes[108–110]. Namely, solid-phase island formation and coalescence (as seen in Figure 3c) initially induced relative tension between points b and c. As more species were deposited (points c to d), a couple of mechanisms may have contributed to the induced compressive stresses: 1) As Li_xS solids continued to deposit, the inevitable incorporation of atoms from the electrolyte into the interface between solid Li_xS and the carbon matrix created a compressive stress in the film, as observed in lithiation of other battery systems and are typical of thin film growth.[12,39,107,111] 2) Solid-phase conversion of Li_2S_2 to Li_2S was initiated, leading to ~30% volumetric expansion.[112] More specifically regarding (2), SEM and EDS (Figure 3c) indicate that some kind of solid phase has formed at this depth of discharge, but XRD (Figure 4, label c) indicates that this phase is amorphous and a clear differentiation between Li_2S_2 or Li_2S is thus not possible. Thus, the increasing compressive stress during the segment (c)-(d) may correlate with the conversion of Li_2S_2 into Li_2S. Lastly, as point (d) was approached, the slope of the stress-vs.-time curve gradually approached zero. If nucleation/growth continued, compressive stresses would likely continue to build up during (c)-(d). We propose two potential mechanisms that may have contributed to the relatively flat curve near the end of lithiation: 1) The driving force for introducing additional excess interface atoms decreased with increasing compressive stresses, eventually producing a steady-state balance. 2) Further lithiation caused plastic yielding in solid lithium sulfide, as has been predicted in simulations.[113]

Likewise, de-lithiation also exhibited at least two different types of mechanical behavior. First, in Region 3 the dissolution of solid Li_2S lead to a near-linear relative increase in stress (toward tension) during the segment (d)-(e), which likely represents removal of the stresses that developed during lithiation. After dissolution of the active solid phases, during segment (e)-(f) or

Region 3, lower order liquid polysulfides converted to higher order polysulfides, which had little effect on the stress since all of (or the majority of) the phase changes occurred in the liquid state. By comparison, in Region 4, as the higher order polysulfides began to deposit back onto the cathode as crystalline sulfur, relative tensile stresses initially occurred in the cathode (shortly after point (f)), followed by relative compression as the sulfur film was regenerated albeit with a different morphology and phase. In this sense, Region 4 can also be regarded as thin film nucleation and growth process, similar to that of Region 2.

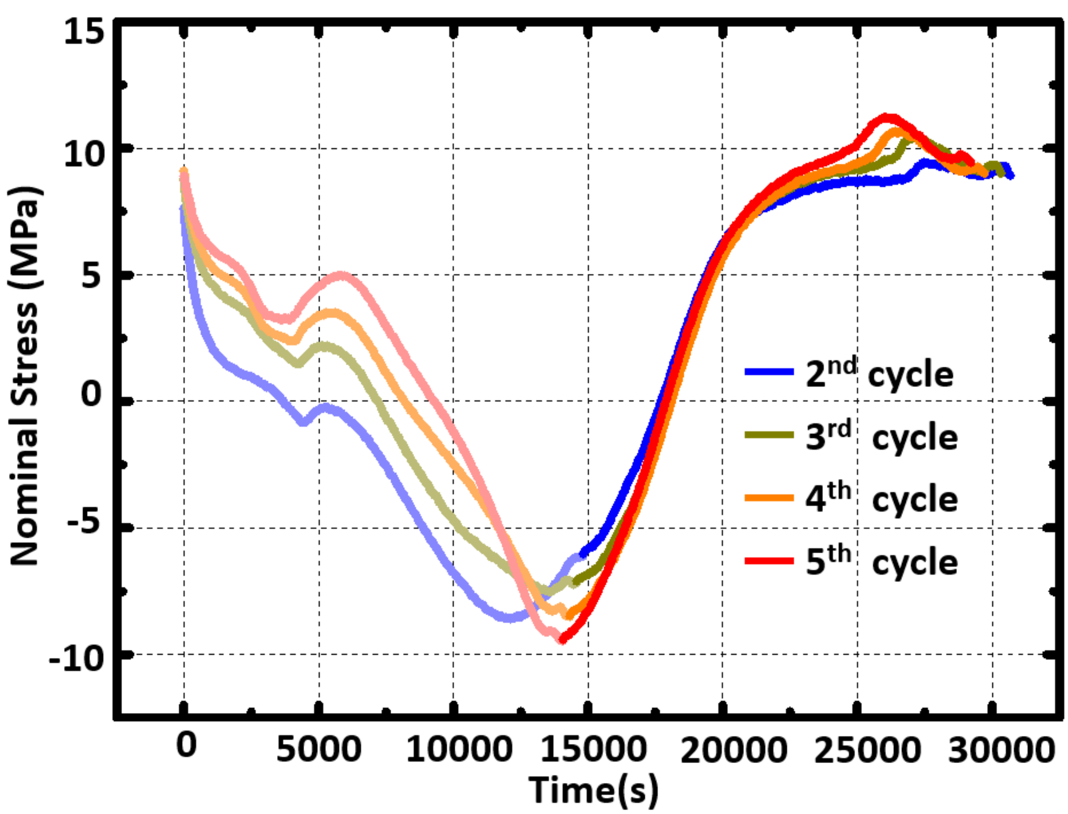

Figure 7 Stress response during cycles 2-5 of a composite sulfur cathode.

Figure 7 displays a zoomed-in view of the stress evolution during cycles 2-5. From Figure 7, the stresses appeared to behave quite repeatably with further cycling. Several trends appeared here that may have significant implications in practical sulfur systems. First and most importantly, the stress exhibited highly recoverable behavior during the thin film nucleation and growth period of these cycles. That is, while the 1st cycle displayed significant hysteresis, the hysteresis appeared to diminish after the 2nd cycle. An explanation is that the significant stresses generated during the first cycle produced plastic deformation in the form of irreversible structural changes (e.g. α-sulfur changes to a mixture of α-sulfur and β-sulfur at the end of de-lithiation during first cycle as mentioned above) but such structural evolution does not significantly occur thereafter. Second, as a related point, the slope from point e to f (figure 5) is negative (near zero) in cycle 1 while this slope becomes positive in cycles 2-5 (Figure 7). Once again, irreversible structural changes that occur during the first cycle likely contribute to this trend (e.g., initially the sample is α sulfur but transforms to α and β sulfur by the end of the first full cycle). Overall, these findings suggest the tantalizing idea that the two polymorphs (α and β) correspond to species favored under different strain conditions and the mechanical stresses thus direct the phase evolution of the materials[114].

Conclusions

In summary, this paper presents the first experimental studies of the mechanical behavior of composite sulfur cathodes during cycling. We observed four major regions of stress generation associated with structural evolution: during discharging: 1) solid-phase conversion of sulfur into electrolyte-soluble polysulfides, followed by 2) deposition of an amorphous solid phase, which ultimately converts to Li_2S, and during charging: 3) dissolution of Li_2S, followed by 4) re-deposition of crystalline sulfur. Different from previously studied intercalative and conversion systems, we conclude that liquid-to-solid phase transformations (nucleation & growth) generate significant stresses during both charging and discharging. Additionally, the measurements indicated that significant hysteresis occurred during the first cycles, which may be attributed to plastic deformation associated with structural transformations. However, subsequent cycles showed nearly elastic and reversible mechanics. As a result, electrodes that withstand the first cycle while retaining active species, which can be engineered through precise mesoscale texturing, hold tremendous promise for structurally robust sulfur-based cathodes. Going forward, we hope our studies will provide fundamental insight into the practical design of mechanically robust sulfur cathodes as well as inspire mechanics-based modeling of coupled electrochemistry, phase transformations, and mechanics.

CHAPTER III

IN-OPERANDO IMAGING OF POLYSULFIDE CATHOLYTES FOR LI-S BATTERIES AND IMPLICATIONS FOR KINETICS AND MECHANICAL STABILITY[2]

Abstract

Enhancing the electrochemical performance of lithium-sulfur batteries requires improved fundamental understanding of the reduction and oxidation of the soluble lithium polysulfide species. To this end, we have designed a 'donut-shaped' cell to enable direct optical observation of phase transformations of a liquid polysulfide catholyte to solid lithium sulfide during electrochemical cycling. We use this technique to image the spatio-temporal distribution of the solid lithium sulfide as it deposits on a carbon matrix at different charging rates. These experiments indicate that the reduction and oxidation of polysulfide catholyte occurs as a thin film deposition and growth process during both lithiation and delithiation. We then investigate the ramifications of these morpological changes in terms of mechanical stability by measuring the evolution of stress during discharge of the polysulfide catholyte. The stress measurements indicate that the average stress during discharging decreases with increasing the charging rate, which we attribute to less dense deposition of lithium sulfide at high discharge rates.

Introduction

With the world's population increasing and technology advancing, demands continue to increase for energy dense storage materials. Lithium sulfur batteries have attracted much attention due to

[2] Reprinted with permission from "In-operando imaging of polysulfide catholytes for Li-S batteries and implications for kinetics and mechanical stability" by Yuwei Zhang, Coleman Fincher, Scott McProuty, Matt Pharr. *Journal of Power Sources* 434 (2019): 226727. Copyright (2019).

their enormous theoretical capacity (1672 mAh/g) and energy density (~2500 Wh/kg), which is an order of magnitude larger than existing transition-metal cathodes (e.g., $LiCoO_2$, $LiFePO_4$, $Li(Ni_xMn_yCo_{1-x-y})O_2$).[19–21,102,115] Combined with its abundance in the earth's crust, sulfur represents a promising low cost, light weight, and relatively environmentally benign candidate material for cathodes of Li-based batteries.[25,27,94]

Despite these promising attributes, a host of issues exist that result in degradation of sulfur batteries, from the loss of active material due to shuttling of electrolyte-soluble polysulfides to the insulating nature of both sulfur and Li_2S (both electronically and ionically) resulting in poor utilization of active material.[91,116] Additionally, as a high-capacity electrode, sulfur suffers severe structural distortions (solid-to-liquid, liquid-to-liquid, and solid-to-liquid phase transformations) intrinsic to the discharge/charge process.[23,91] Correspondingly, the complicated conversion reactions produce an enormous volume expansion (~80%), which can lead to a loss of contact between the insulating active materials and the conductive carbon matrix.[117] These inactive layers eventually spread, producing a barrier for further lithium ion transport, and ultimately leading to capacity fade. [118]

To address these issues, recent studies have implemented soluble lithium polysulfides encapsulated by porous carbon frameworks as an alternative to using solid sulfur as the active material. These systems have demonstrated more uniform distribution of active material and more intimate contact to the carbon-based matrices.[119–121] This configuration will also likely leads to enhanced kinetics since it avoids the initial solid to liquid phase transformation from S_8 to Li_2S_8.[122] Overall utilizing a modified conductive carbon matrix as the host material and dissolved lithium polysulfides as the active material, several groups have demonstrated high-performance batteries with low polarization, high areal capacity, and promising cycling performance.[123–126]

Despite these advances, a full understanding of the conversion from soluble polysulfides to solid lithium sulfide is lacking. In particular, direct observation of when/where solid species form during discharge would provide insight into the conversion process. Likewise, the details of the morphological evolution are intimately connected to stresses that develop during cycling. Understanding these links would provide guidance into the design of host materials and cycling conditions that mitigate mechanical damage, thereby promoting stable cycling. To fill these gaps in knowledge, we construct a simple in-operando lithium-sulfur ‘donut cell’ design, which enables the user to directly image the spatio-temporal distribution of solid lithium sulfide species during electrochemical cycling. We also perform in-situ measurements of mechanical stresses generated during electrochemical discharge of a polysulfide catholyte, i.e., during deposition of lithium sulfide onto a host carbon matrix. These experiments provide key insight into the lithiation/delithiation process of polysulfide catholytes and establish a technique for future characterization of various catholytes under various electrochemical cycling conditions.

Materials and methods

Electrochemical cell preparation

A spin coating process prepared conductive matrices, using carbon nanoparticles (99.99% US Research Nanomaterials, Inc.) as the conductive component, and polyvinylidene fluoride (PVDF, MTI Corporation) as the binder in a 6:1 (C: PVDF) mass ratio. Mixing these components into solution using N-Methyl-2-pyrrolidone (NMP, MTI Corporation) as a solvent, followed by magnetic stirring for 3 hours produced a slurry. Spin coating at 1000 rpm for 1 minute deposited the slurry onto mirror-finished T304 stainless steel (Metals Depot). After spin coating, the resulting film dried at 45ºC for 3 hours. A profilometer (Veeco Dektak 150 Profilometer) provided measurements of the thickness of the composite carbon matrix. We should note that by integrating C-nanoparticles in a manner that produces overall porosity, we are implementing shapes (interconnected porous structure) and sizes (nanometer scale features) that are representative of typical geometries used in Li-S systems.[120,127–131]

To prepare the polysulfide catholyte, sulfur nanoparticles (99.99% US Research Nanomaterials Inc) and lithium sulfide (Li_2S, 99.98% trace metals basis) were mixed in an appropriate molar ratio in a solution of 1,3-dioxolane (DOL, Sigma-Aldrich) and 1,2-dimethoxyethane (DME, Sigma-Aldrich) (volume ratio=1:1) with the addition of 0.5 wt.% $LiNO_3$ (Sigma-Aldrich) as an additive, thereby rendering a 1M Li_2S_6 solution (molar concentration calculated based on the mass of sulfur). Heating this mixture at 55ºC overnight produced a dark brown solution. For the blank electrolyte (i.e., the one with no dissolved polysulfide), dissolving 1.0 M lithium bis-trifluoromethanesulphonylimide (LiTFSI, Sigma-Aldrich) in a 1:1 by volume solution of 1,3-dioxolane (DOL, Sigma-Aldrich): 1,2-dimethoxyethane (DME, Sigma-Aldrich), with the addition of 0.5 wt.% $LiNO_3$ as an additive (Sigma-Aldrich) produced the blank electrolyte. We used a precision electronic single channel pipette (MTI Inc.) to withdraw 20 µL of catholyte for each test. As such, the equivalent mass we used for each test is 0.64 mg.

A two-electrode electrochemical test cell with a quartz viewing window (MTI Corporation) facilitated simultaneous electrochemical and mechanical measurements, as depicted in Figure 8. We assembled this cell in an argon-filled glovebox with oxygen and moisture levels less than 0.1 ppm. Adding polysulfide catholyte (1M Li_2S_6) into the composite carbon matrix produced the C-PVDF-Li_2S_6 composite electrode. We then put a Celgard 2400 separator (MTI Corporation) on top of the cathode following by adding blank electrolyte. Finally, placing a lithium metal ribbon (99.9% trace metals basis, Sigma-Aldrich) on top of the separator produced the anode.

Electrochemical measurements

A PARSTAT MC Multichannel Potentiostat (Princeton Applied Research) conducted galvanostatic cycling at various current densities between the open circuit potential to 1.8 V vs Li/Li+. All experiments occurred at room temperature (25ºC).

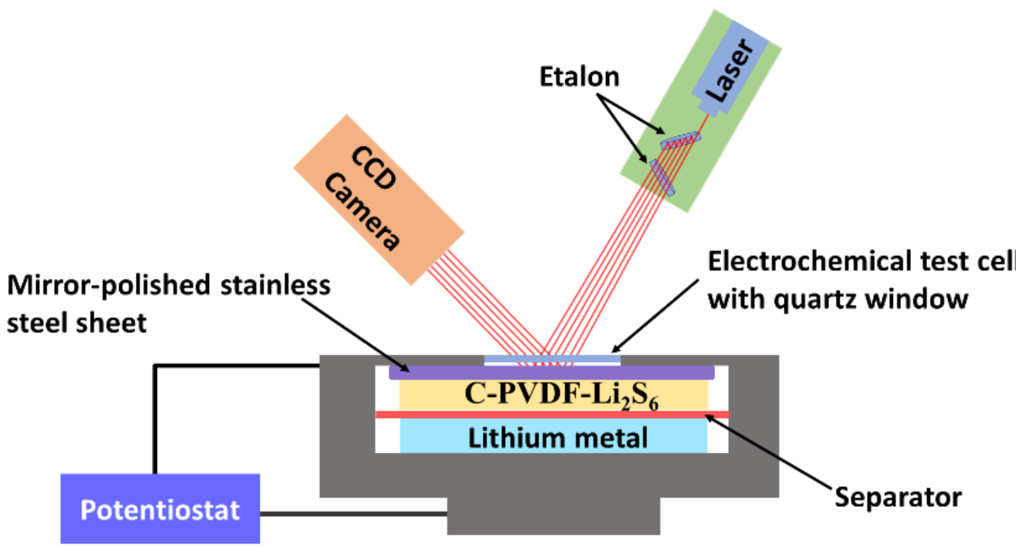

Figure 8 A schematic representation of the electrochemical test, which employs a split cell with a quartz viewing window through which the use of an in-situ multibeam optical sensor enables measurements of stress during electrochemical cycling.

Mechanical characterization

A multibeam optical stress sensor (MOS) from k-Space Associates monitored the curvature of the substrate (ΔK) during electrochemical cycling, as shown in Figure 8. The MOS employs an array of parallel laser beams to measure the curvature of the substrate of the composite cathode. The array of laser beams allows simultaneous illumination and detection, which in turn greatly reduces noise in the measurements caused by fluid motion in the electrochemical cell or by ambient vibrations. The cell is also placed on an antivibration table during testing. Using Stoney's equation, we deduced the average stress change in the composite cathode during cycling[97,98],

$$\Delta\sigma = \frac{E_s\, h_s^2}{6h_f(1-\nu_s)}\Delta K,$$

where E_s is the elastic modulus of the substrate ($E_s = 203$ GPa), h_s is the thickness of the substrate ($h_s = 0.736$ mm), ν_s is the Poisson's ratio of the substrate ($\nu_s = 0.29$), and h_f is the thickness of electrode film (measured via profilometry before the test). In this study, we take h_f as constant for each test, such that the stress calculated is the nominal in-plane stress. A previous study has shown that the thickness of a similar porous composite sulfur thin film cathode fabricated through a slurry method remains constant during electrochemical cycling.[132]

In-operando optical imaging

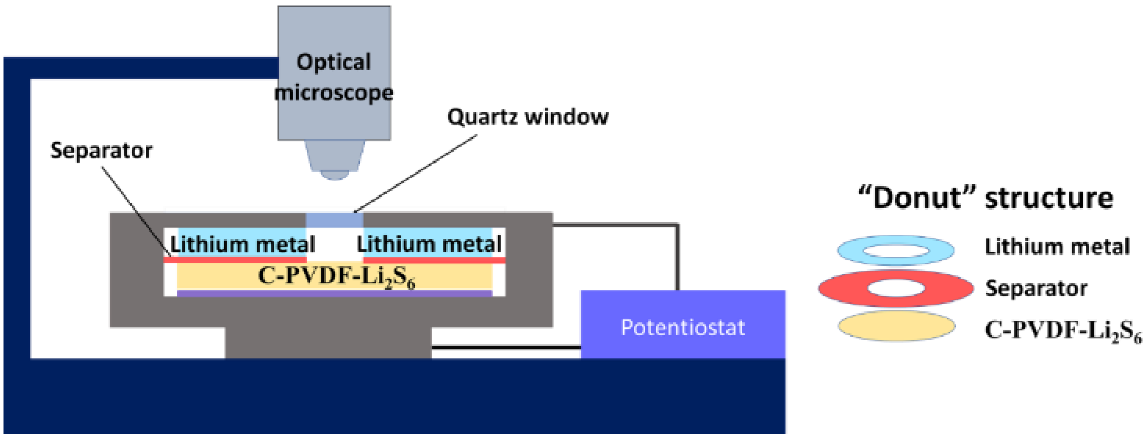

Figure 9 A schematic representation of the electrochemical setup in which in-operando optical microscopy enables imaging of morphological changes during electrochemical cycling. Cutting the Li metal and separator in to a 'donut' shape opened an optical viewing path to the surface of the cathode.

Assembly of the batteries for these studies occurred as in Section 2.1 except that cutting the separator and lithium foil into a 'donut' shape opened an optical viewing path to the surface of the cathode (see Figure 9). A VHX-600 Digital Microscope captured images every 15 s to monitor the evolution of the surface morphology during electrochemical cycling at various charging rates.

Results and discussion

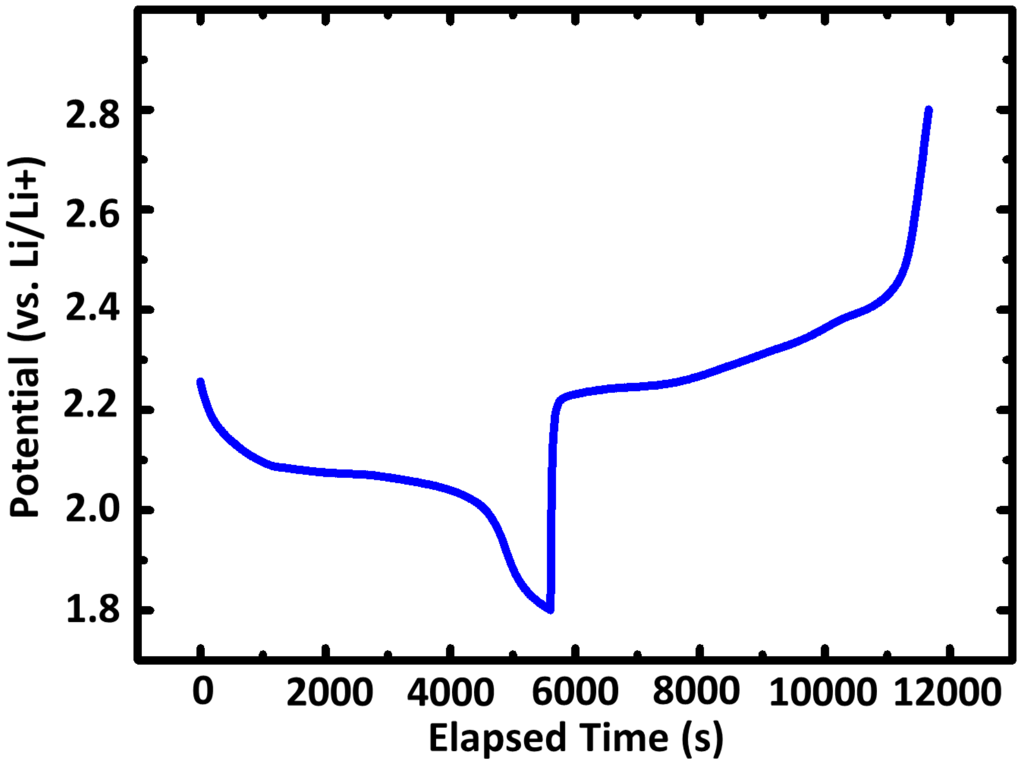

Figure 10 Representative potential response of Li_2S_6 polysulfide catholyte during galvanostatic lithiation/de-lithiation at a current density of 165 μA/cm^2.

Figure 10 shows the change in potential during galvanostatic cycling of a lithium polysulfide catholyte (Li_2S_6) at 165 μA/cm^2. During both discharge and charge, a number of phase transformations occur (as indicated by voltage plateaus), which are substantially more complex than standard intercalation cathodes, such as $LiFePO_4$, $LiCoO_2$, and $Li(Ni_xMn_yCo_{1-x-y})O_2$.[15,102,115] To better understand this complicated cycling process, we monitored the changes in morphology of the surface of the C-PVDF-Li_2S_6 cathode during lithiation/de-lithiation at two different charging rates. Additionally, to connect this morphological evolution to potential mechanical issues, we measured the evolution of mechanical stresses during discharge at various current densities to paint a full picture of how kinetics, morphology, and mechanics interact during operation of polysulfide catholytes.

Morphological evolution during lithiation at different current densities

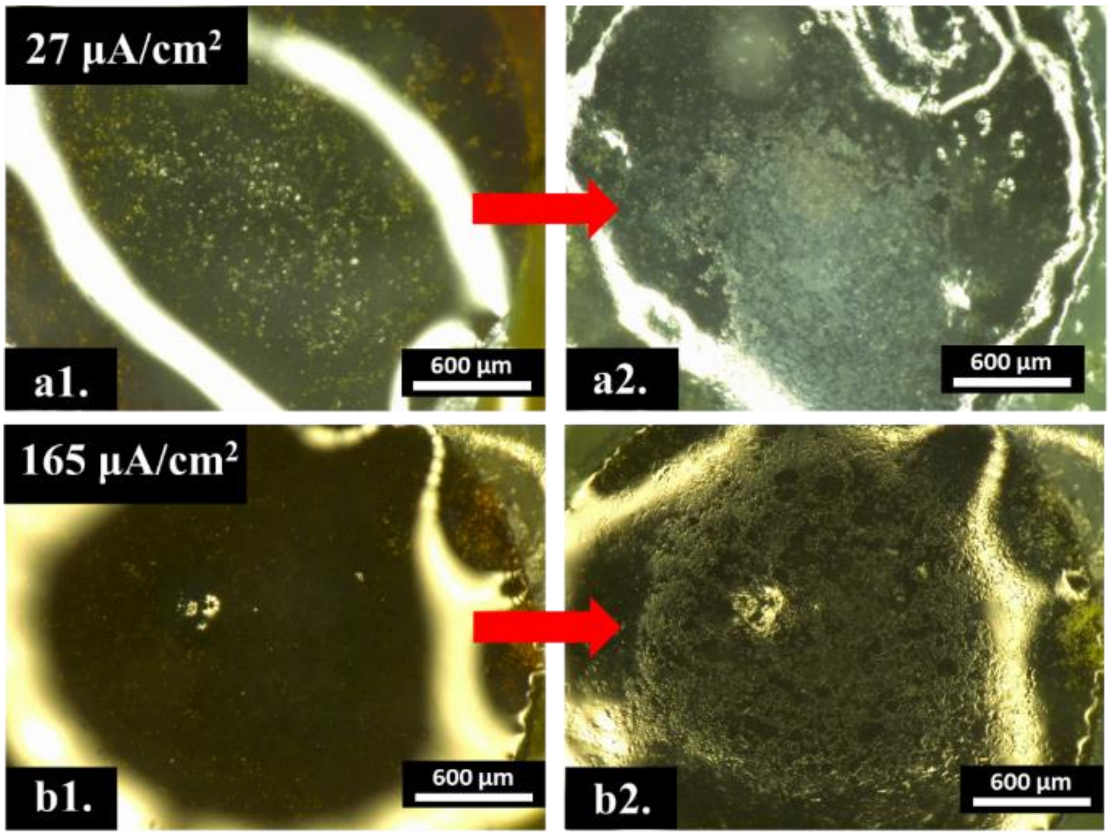

Figure 11 Optical microscopy images of C-based matrices soaked with polysulfide catholyte during the first lithiation. (a1) Before (a2) after lithiation at a current density of 27 μA/cm^2. (b1) Before and (b2) after lithiation at a current density of 165 μA/cm^2.

Figure 9 shows the experimental setup used to monitor the morphological evolution during electrochemical cycling of a carbon matrix soaked with polysulfide catholyte (C-PVDF-Li_2S_6). Using this setup, Figure 11 shows optical images of the morphology of the polysulfide catholyte before and after the first lithiation at current densities of 27 μA/cm^2 (a1-a2) and 165 μA/cm^2 (b1-b2) (for the full-time evolution, see the Videos S1 and S2 in the supporting information). The curved bright lines around the periphery of these images occur from light reflecting off of the separator in the battery. In these two sets of images (and the corresponding videos), we observe that the solid phase deposited as islands, which gradually grew and coalesced into a relatively large region that covers the majority of the center region. Within the deposited regions, the lithium sulfide generally packed less densely at higher current densities, i.e., less densely in Figure 11-b2 as compared to Figure 11-a2. Several papers have discussed the phase transformation corresponding to the 2.1 V voltage plateau, which represents a liquid-to-solid phase transformation with relatively slow kinetics.[133–135] In this study, Figure 11 and Videos S1 and S2 (supporting information) show direct evidence that lithiation of the polysulfide catholyte at a voltage plateau near 2.1 V occurs via a thin film nucleation and growth process of the solid phase. Moreover, using a larger current density results in the system having insufficient time for the growth process to fully occur, thereby producing a relatively low density of lithium sulfide and correspondingly low capacities. As such, our studies underscore the importance of understanding the precise mechanisms of this growth process. Doing so would provide insight into defining host matrix chemistries and geometries, charging conditions, and catholyte chemistries (e.g., additives) that would enhance the kinetics of the growth process, and thereby should represent a key area of research going forward.

As a final note, although we believe our experimental setup accurately mimics a realistic environment of oxidation and reduction of polysulfides, the reaction process in a more standard electrochemical cell (without ‘donut’ holes in the center of separator and lithium metal ribbon) may vary somewhat since the kinetics for polysulfide deposition and dissolution may differ between the region near the edge of the ‘donut’ and in the center of the ‘donut’. However, based on general similarity observed herein to morphologies seen in previous studies, we believe our technique provides useful information regarding the general changes in morphology under various conditions.[132,136] For instance, in a previous study[132], we surmised that the 2.1 V voltage plateau corresponds to a nucleation and growth type phase transformation. Videos S1-S3 (supporting information) provide direct evidence of the time evolution of this nucleation and growth process. Also, compared to in-situ TEM studies, our technique is relatively simple in terms of sample preparation and provides a much larger field of view.[137,138]

Morphological evolution during de-lithiation

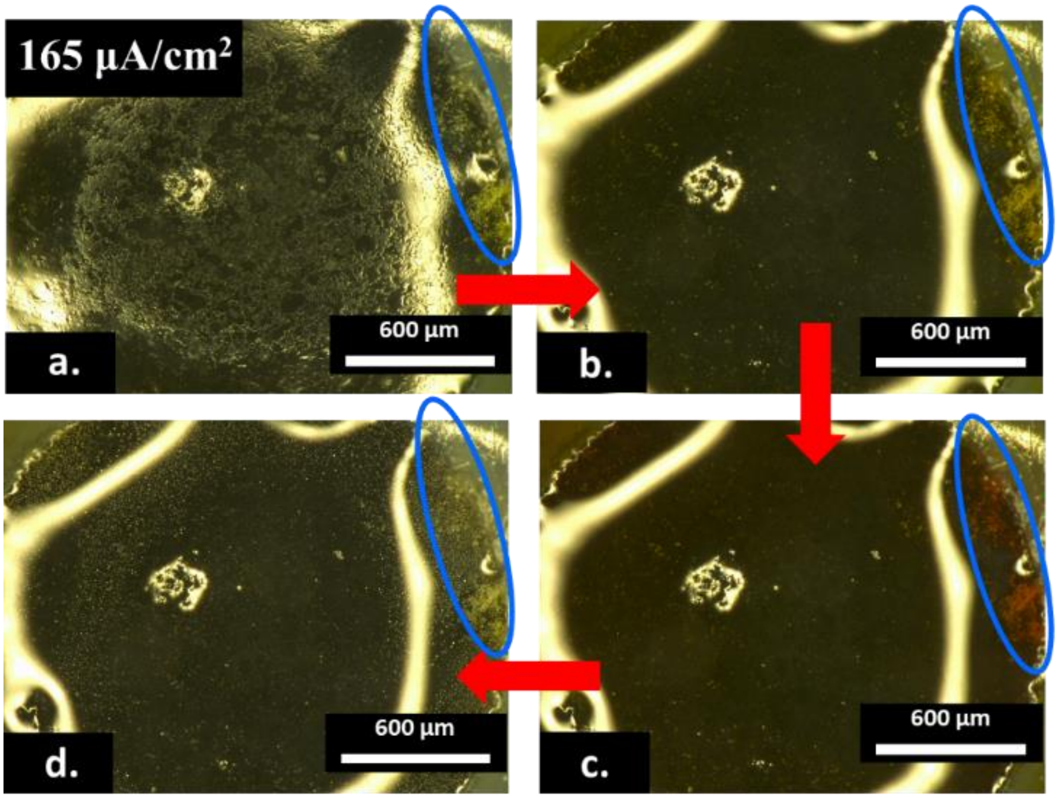

Figure 12 Optical microscopy images of C-based matrices soaked with polysulfide catholyte at different states during delithiation at a current density of 165 μA/cm^2. (a) represents the start and (d) represents the end of delithiation. (b) and (c) are intermediate points chosen based on interesting morphological features. The blue circles highlight an area of interest.

Figure 12 shows the morphological evolution of a polysulfide catholyte during delithiation at a current density of 165 μA/cm^2. These images correspond to the same electrode as shown in Figure 11 b1-b2. The full time-lapsed Video S3 of this reaction is also included in the supporting information. In a previous study[132], we surmised that near the end of de-lithiation, a solid phase of sulfur will deposit back onto the carbon matrix in a thin film nucleation and growth type process. Figure 12 and Video S3 (supporting information) provide direct observation of the time evolution of this nucleation and growth process. Specifically, at the beginning of delithiation, solid lithium sulfide exists on the carbon matrix (Figure 12a). Upon delithiation, the solid phases disappeared completely, indicating their dissolution into the electrolyte (see Figure 12b). With further delithiation, different dissolved polysulfides form (Li_2S_4, Li_2S_6, Li_2S_8) in the center region, such that Figure 12c appears similar to that of Figure 12b. However, in the circled region near the top right corner in Figure 12c, some reddish liquid appears, different from that of the previous images. As reported in several previous studies, with further delithiation, the color of polysulfide will change from light yellow to dark red upon conversion from low chain polysulfides (Li_2S_4) to high chain polysulfides (Li_2S_8), which appears to be happening here as well.[139–142] At the end of de-lithiation (Figure 12d), the reddish liquid (Li_2S_8) disappears completely and solid particles (solid sulfur) deposit onto the carbon matrix. This final phase transformation again appears to occur through a thin film nucleation and growth process (see Video S3), as we have hypothesized in a previous study.[132]

Stress evolution during lithiation at various current densities

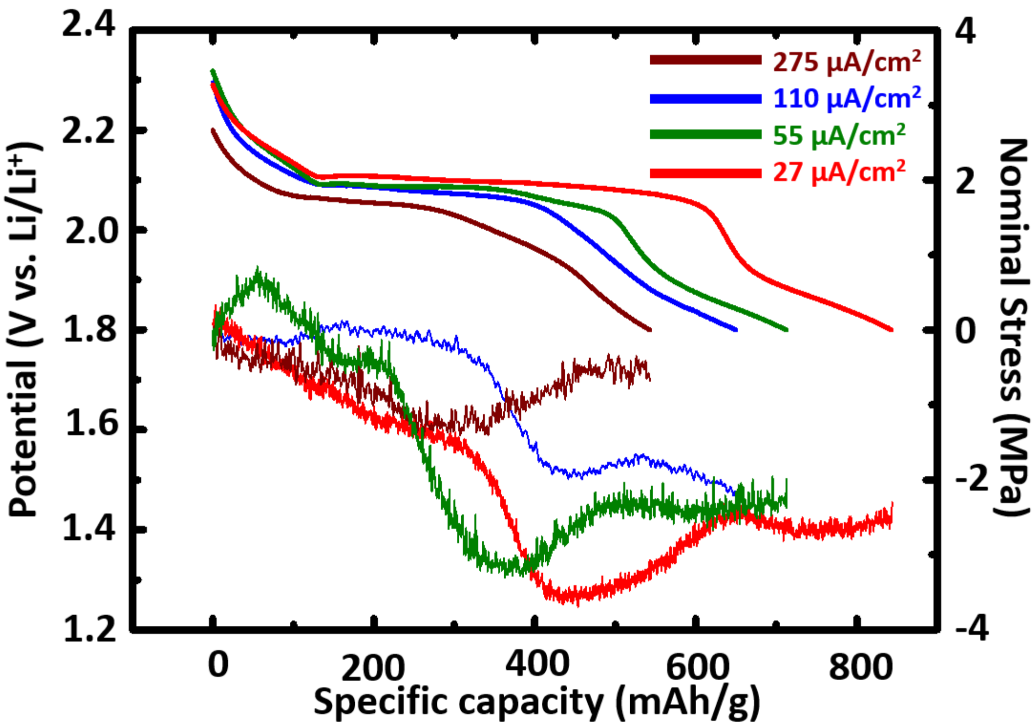

Figure 13 Stress response during the first lithiation of C-based matrices soaked with polysulfide catholyte at different current densities.

We performed stress measurements in polysulfide-soaked carbon matrices, as to demonstrate the potential ramifications of kinetic effects in terms of mechanical stability. Figure 13 shows the experimental setup used to measure the stress changes during electrochemical cycling. A multibeam stress sensor (MOS) monitored the change in curvature (ΔK) of the composite cathode during the process. Figure 13 shows potential and the corresponding changes in nominal stress in the polysulfide-soaked carbon matrices during lithiation at various current densities. We conducted multiple additional tests to confirm these trends for varying current densities. Additionally**,** we should note that these stresses represent the average stress through the thickness of the composite cathode during lithiation. They do not provide locally differentiable information (e.g., stress in Li_2S vs. stress in PVDF), as discussed in a previous paper.[132] However, these measurements do provide useful information regarding the overall mechanics in the system during electrochemical reactions. In a previous paper[132], we performed a systematic study related to stresses that develop during cycling of solid composite sulfur cathodes. Herein, we will focus on how the current density influences stress generated during lithiation of polysulfide catholytes. The stress profiles demonstrate a similar general trend (i.e., shape of the curve) at various current densities. In particular, an incubation period occurs first in which the stress does not change significantly or changes with a relatively small slope. This period likely occurs due to liquid-to-liquid phase transformations or side reactions occurring during the initial stages of lithiation. This period is followed by a region in which the compressive stress increases quickly (with a relatively large slope). In this stage, nucleation and growth of the solid Li_xS phases occurs, which induces stress in the matrix. Toward the end of lithiation, the stress again appears relatively flat. This stage may occur due to additional side reactions occurring or may stem from plastic deformation occurring in the Li_xS solid phase that forms, i.e., further lithiation (i.e., straining) does not induce much additional stress. Additionally, we found that the maximum nominal stress decreased with increasing current density. This phenomenon has the opposite trend compared to that reported in Si anodes.[106] In many other systems (such as Si), the electrode remains a solid during cycling and also exhibits strain-rate sensitive constitutive behavior.[12,13,35,102] As such, larger charging rates produce larger strain rates and thus larger stresses.[15] By comparison, in our polysulfide catholyte battery system, when the current density increases, less of the solid phase deposits on the host matrix due to the previously discussed kinetic limitations of the growth process. With less solid phase depositing, the average stress in the system will be smaller. As a result, slower charging rates will undoubtedly increase the capacity but will also produce larger stresses, thereby again underscoring the importance of microstructural/geometric design of the host matrix to prevent mechanical damage.

Conclusions

In summary, this paper develops a novel technique to observe the morphological evolution in-operando during electrochemical cycling of polysulfide catholytes. We used this technique to monitor the morphological evolution of a C-PVDF matrices soaked in a polysulfide catholyte during lithiation/delithiation. These studies clearly demonstrate that solid lithium sulfide deposits onto the host C-PVDF matrices by a thin film nucleation and growth type process during lithiation. Likewise, solid sulfur deposits through a similar process during delithiation. Moreover, this growth process depends on the charging rate, with larger charging rates leading to a more inhomogeneous distribution of the deposited solid species, and thus lower capacities. We further connect these effects to potential consequences in terms of mechanical stability by performing in-operando stress measurements during lithiation of C-PVDF matrices soaked in polysulfide catholytes at various charging rates. We find that slower charging rate produces higher capacities but larger stresses, thereby underscoring the importance of microstructural/geometric design of the host matrices to prevent mechanical damage. Overall, these studies provide connections between electrochemistry and the corresponding kinetics, mechanics, and morphological phenomena associated with soluble lithium polysulfides. As such, we hope our studies will inspire future electro-chemo-mechanical models of sulfur-based batteries.

CHAPTER IV

CHEMO-MECHANICAL DEGRADATION IN V2O5 THIN FILM CATHODES OF LI-ION BATTERIES DURING ELECTROCHEMICAL CYCLING[3]

Abstract

We have devised an approach to fabricate dense textured V_2O_5 thin films, which allows us to scrutinize the root cause of capacity fade in V_2O_5 cathodes of Li-ion batteries. Specifically, we performed in-situ measurements of stress of V_2O_5 thin films during 50 electrochemical cycles. Surprisingly, electrochemical cycling appears to induce elastic and rate-independent deformation over a voltage range relevant to battery operation (4 - 2.8 V). However, the compressive stresses gradually increase with cycle number during the first few cycles, likely due to side reactions and/or residual Li left in the V_2O_5, even after delithiation (to 4 V). Further cycling leads to accumulated mechanical damage (e.g., fracture, delamination) and structural damage (e.g., amorphization), which ultimately result in severe capacity fade.

Introduction

The vast majority of studies on Li-ion batteries have focused on improving their electrochemical characteristics. Mechanics-based issues have been largely overlooked. Moreover, of the existing mechanics-based studies, relatively few have targeted cathode materials, likely due to their small volume expansion (~2-8%), compared to those of anodes (up to ~300%).[1–8] However, it is important to note that a strain larger than 0.1-1% is considered severe for brittle ceramics, such

---

[3] Reprinted with permission from “Chemo-Mechanical Degradation in V2O5 Thin Film Cathodes of Li-ion Batteries during Electrochemical Cycling” by Yuwei Zhang, Yuting Luo, Cole Fincher, Sarbajit Banerjee, Matt Pharr. *Journal of Materials Chemistry A* 7.41 (2019): 23922-23930. Copyright (2019).

as are many of the cathode materials.[1] Thus, stresses generated during electrochemical cycling may result in fragmentation, disintegration and fracturing, and/or loss of contact to the current collectors, all of which can lead to severe capacity fade.[9–15] Indeed, even volume changes during electrochemical cycling of commercialized cathode materials, such as $LiCoO_2$ (2.6% volume change), $LiFePO_4$ (6.8% volume change), and $LiMnO_2$ (7.5% volume change) have been shown to produce mechanical degradation.[1–6,16]

Vanadium oxide (V_2O_5) is a promising material for next-generation cathodes and can be stabilized as different polymorphs with varying atomic connectivities.[42–47] Indeed, recent studies have suggested that several polymorphs of V_2O_5 are ideal candidates for hosting multivalent metal-ions with large volumes while maintaining excellent electrochemical performance.[48–51] Likewise, ion-stabilized V_2O_5 with large interlayer spacing has shown enhanced electrochemical performance using pre-intercalation.[50,52–56] The theoretical capacity of V_2O_5 is an enormous 442 mAh/g, as it can host up to 3 Li atoms per formula unit (V_2O_5).[43,47] However, the extent of reversible intercalation has been found to be much lower.[43] The crystal structure of V_2O_5 remains intact if a voltage window is set such that cycling occurs only between the orthorhombic α-V_2O_5 and the δ-$Li_xV_2O_5$ phase.[43,44] As such, pristine α-V_2O_5 presents a model system to study discharging/charging-induced mechanical loading during electrochemical cycling, potentially without conflating the influence of crystal structure degradation.

To this end, we investigated the electrochemical and mechanical performance of V_2O_5 cathodes during electrochemical cycling. To deconvolute the influence of binders and carbon matrices on their mechanical response (i.e., to measure intrinsic properties of V_2O_5), we fabricated dense textured thin films of V_2O_5 by plasma sputtering. We then performed in-situ measurements of mechanical stresses generated during cycling under various electrochemical conditions. Post-mortem observation of samples cycled to different extents allowed for understanding the damage evolution in these systems. Likewise, we investigated the evolution of electrochemical properties, crystal structure, and morphology during extended cycling. Overall, this paper links electrochemical, structural, and mechanical observations to develop mechanistic understanding of the root cause of capacity fade in V_2O_5 cathodes of Li-ion batteries.

Experimental details

Sample preparation of V_2O_5 thin film

We implemented two side mirror-polished T304 stainless steel (Metals Depot) as the substrates for the working electrodes. The sputtering process was performed at room temperature (25ºC). The substrate was cleaned with acetone and isopropanol and placed into a sputtering system (AJA Inc.) with a base pressure of ~3×10^{-8} Torr. First, the machine sputtered 15 nm of titanium onto the stainless-steel substrate using a pressure of 3 mTtorr of argon and a DC power of 100 W for 5 min. The Ti underlayer is used to improve the adhesion between the V_2O_5 thin film and the stainless steel substrate. Next, the sputtering system deposited 330 nm of material from a vanadium target using a pressure of 2 mTorr with a mixture of argon and oxygen (Ar: 20 sccm, O_2: 4.4 sccm) and a DC power of 123 W for 5 hours. After deposition, we transferred the sample to a furnace (Thermo Fisher Scientific Inc.) and annealed it in air at 350°C for 10 hours. The working area of the electrode is 1.69 cm^2. A profilometer (Veeco Dektak 150 Profilometer) provided measurements of the thickness of the fabricated electrode.

Structural and morphological characterization

A parallel beam geometry using a Bruker-AXS D8 X-ray diffractometer with a Cu Kα (wavelength λ = 0.154 nm) radiation source produced X-ray diffraction patterns and pole figures. A scanning electron microscope (SEM, JEOL JSM-7500F) operating at 10 kV captured the surface morphology. An atomic force microscope (AFM, Bruker-Dimension Icon) determined the morphology and roughness of the surface of the electrode. An MPLN 100× microscope equipped with a Jobin-Yvon HORIBA Labram HR instrument was used to acquire Raman spectra with excitation from a 514.5 nm Ar-ion laser. A DXS 500 optical microscope captured images of the surface of sample after cycling to different extents.

Electrochemical cell preparation

A two-electrode electrochemical test cell with a quartz viewing window (MTI Corporation) facilitated simultaneous electrochemical and mechanical measurements (see our previous work for detailed information regarding configuration of the cell[143,144]). We assembled this cell in an argon-filled glovebox with oxygen and moisture levels less than 0.1 ppm. In addition to the V_2O_5 thin film described above, the battery consisted of a lithium metal ribbon (99.9% trace metals basis, Sigma-Aldrich) anode and a Celgard 2400 separator (MTI Inc.). The electrolyte was 1M $LiPF_6$ (MTI Inc.) in a 3:7 ratio (volume ratio) of ethylene carbonate : dimethyl carbonate. Using a PARSTAT MC Multichannel Potentiostat (Princeton Applied Research), we conducted galvanostatic cycling at various current densities (C rate) as well as measurements using electrochemical impedance spectroscopy. The C rate is based on the theoretical capacity of V_2O_5 (294 mAh/g) between 4-2 V vs. Li/Li^+.[43,47]. All experiments were conducted at room temperature (25°C).

Mechanical characterization

A multibeam optical stress sensor (MOS) from k-Space Associates monitored the curvature of the substrate (ΔK) during electrochemical cycling. The cell was placed on an antivibration table during testing. Using Stoney's equation, we deduced the average stress change in the thin film during cycling[97,98]:

$$\Delta\sigma = \frac{E_s\, h_s^2}{6h_f(1-\nu_s)}\Delta K,$$

where E_s is the elastic modulus of the substrate ($E_s = 203$ GPa), h_s is the thickness of the substrate ($h_s = 0.736$ mm), ν_s is the Poisson's ratio of the substrate ($\nu_s = 0.29$), and h_f is the thickness of thin film electrode ($h_f = 330$ nm). In this study, we take h_f as constant for each test, such that the stress represents the nominal in-plane engineering stress. Throughout this study, the sign convention for compressive stress is negative and for tensile stress is positive.

Results

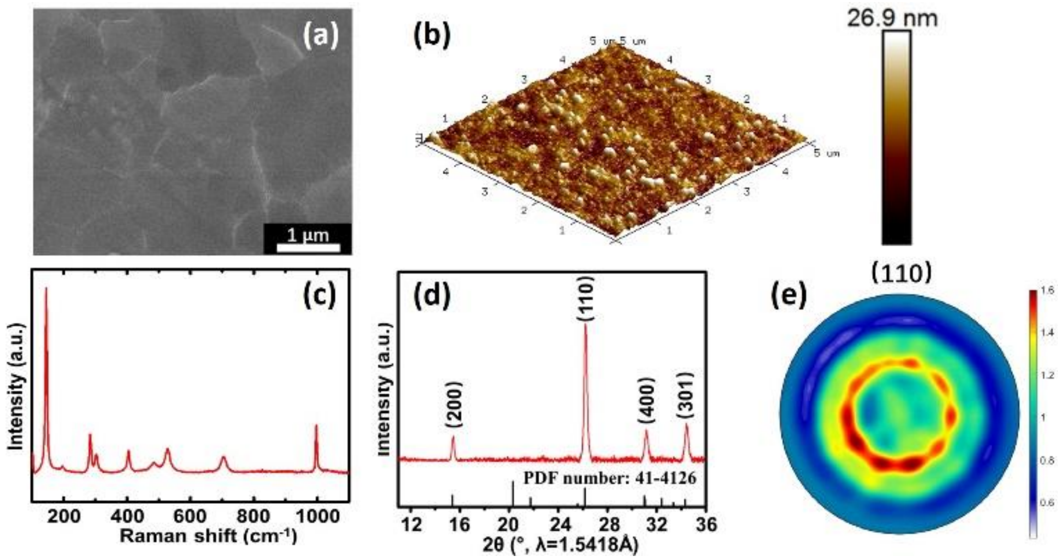

Figure 14 Surface morphology and structural characterization of V_2O_5 thin films: (a) SEM image, (b) AFM image, (c) Raman spectroscopy, (d) X-ray diffraction pattern of as-deposited film on a stainless steel substrate, and (e) corresponding pole figure of V_2O_5 thin film, indicating high texture in the (110) direction.

In Figure 14, we show the surface morphology and crystal structure of polycrystalline V_2O_5 thin films via different characterization techniques. In Figure 14a, the SEM image shows that the film is flat without discernible any bulges or pits. The contrast (white lines) in the SEM image likely indicates the location of grain boundaries. Likewise, in Figure 14b, an AFM measured the surface roughness and morphology over a 5 µm by 5 µm region. Raman spectroscopy in Figure 14c shows eight bands that match with a previous study of polarized Raman spectra of V_2O_5, based on phonon state calculations and several experimental results.[42,43,145,146] Figure 14d displays the x-ray diffraction pattern of a V_2O_5 film grown on a stainless steel substrate with a PDF of powder V_2O_5 for comparison. In Figure 14e, we conducted XRD pole figure analysis using the MTEX toolkit, which indicated a high texture of the V_2O_5 films in the (110) direction.

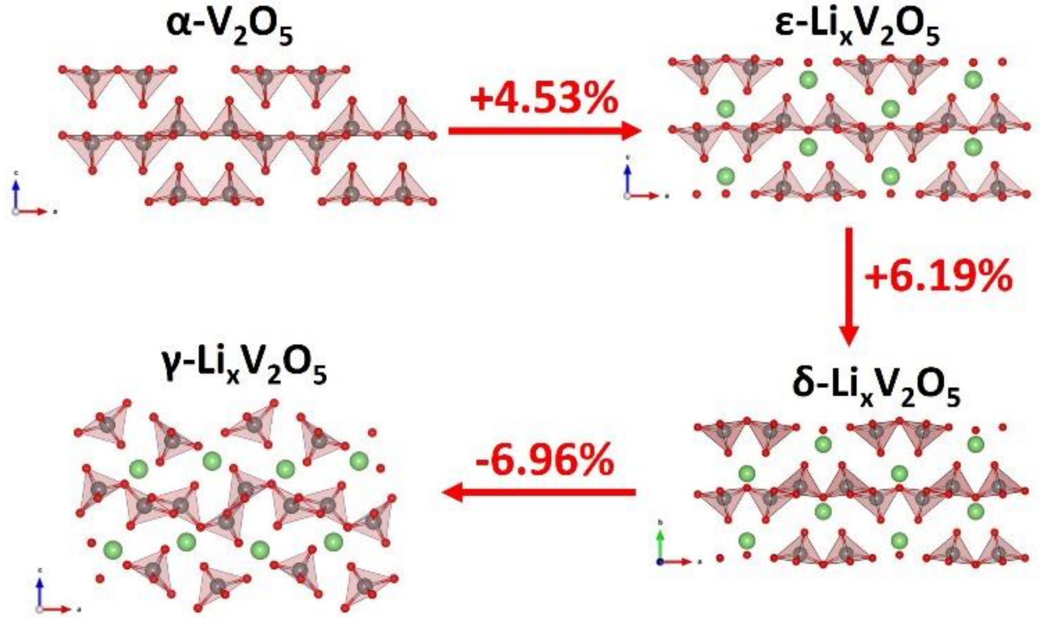

Figure 15 Crystal structures of various phases during lithiation of V_2O_5: α-V_2O_5, ε-$Li_xV_2O_5$, δ-$Li_xV_2O_5$, and γ-$Li_xV_2O_5$, and the corresponding volume expansion during each phase transformation.

Figure 15 shows the crystal structures of various phases in this system. The structures shown have been rendered using Vesta based on structures derived from the ICSD database. Overall, lithiation-induced volume expansion from α-V_2O_5 to δ-$Li_xV_2O_5$ is near 11%. It is important to note that the subsequent intercalation-induced phase transformation from δ-$Li_xV_2O_5$ to γ-$Li_xV_2O_5$ induces volume contraction. In Table S1, we further detail the dimensional parameters associated with the different phases.

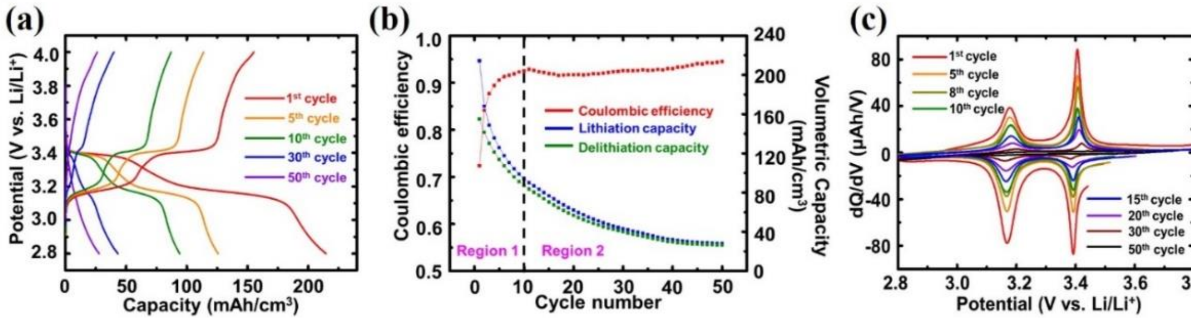

Figure 16 Electrochemical tests of V_2O_5 thin films. (a) Galvanostatic discharge/charge profiles measured during 50 cycles between 4.0 – 2.8 V vs. Li/Li^+ at a current density of 5.92 μA/cm^2 (0.2 C). (b) Corresponding coulombic efficiency and volumetric capacities. (c) Corresponding differential capacity curve at selected cycles.

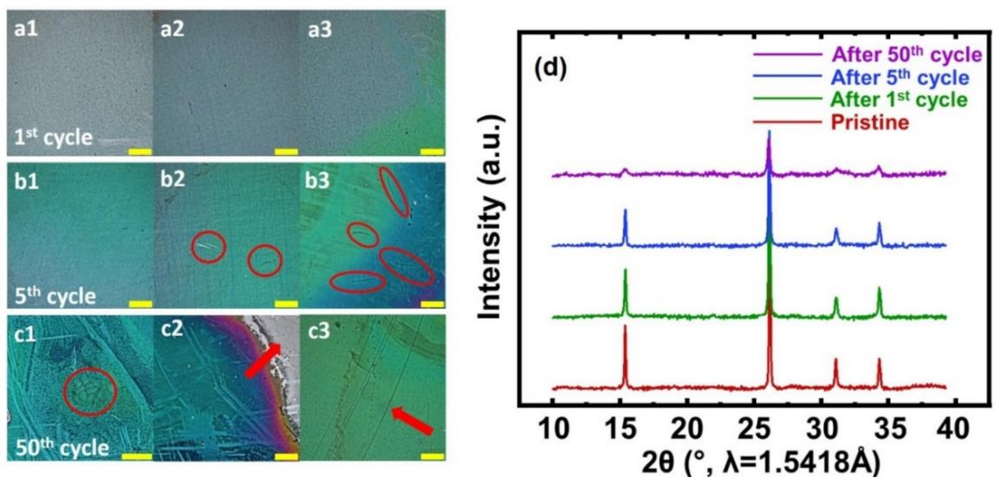

Figure 17 Optical microscopy images of V_2O_5 thin films after galvanostatic cycling between 4.0 – 2.8 V vs. Li/Li^+ at a current density of 5.92 μA/cm^2 (0.2 C). The scale bar in the figures indicates 300 μm. (a1-a3) Optical images of V_2O_5 thin film after 1 cycle, (b1-b3) after 5 cycles, and (c1-c3) after 50 cycles. (d) Evolution of XRD patterns of a V_2O_5 thin film during cycling.

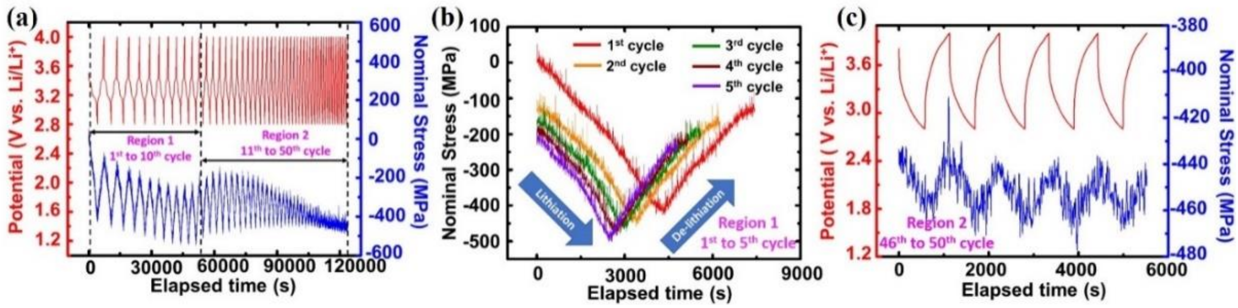

Figure 18 (a) Potential and corresponding stress response during 50 galvanostatic cycles of a V_2O_5 thin film between 4.0 – 2.8 V vs. Li/Li^+ at a current density of 5.92 µA/cm^2 (0.2 C). (b) Enlarged view of stress response during cycles 1-5. (c) Enlarged view of potential and corresponding stress response during cycles 46-50.

Figure 16 shows the electrochemical performance of a V_2O_5 thin film during galvanostatic cycling at a current density of 5.92 µA/cm^2 (0.2 C). In Figure 16a, we lithiated a pristine V_2O_5 thin film from the open circuit voltage to 2.8 V as a cutoff voltage, which corresponds to the δ-$Li_xV_2O_5$ phase, followed by de-lithiation back to 4 V. We cycled the battery 50 times. Through the lithiation process, we found two voltage plateaus at 3.4 V (α-$Li_xV_2O_5$ to ε-$Li_xV_2O_5$) and 3.16 V (ε-$Li_xV_2O_5$ to δ-$Li_xV_2O_5$). Figure 16b shows the corresponding coulombic efficiency and volumetric capacity variation during cycling. Figure 16c shows the corresponding differential capacity curves during cycling.

Figure 17 (a1-a3), (b1-b3), and (c1-c3) show optical microscope images after galvanostatic cycling of V_2O_5 between 4.0 – 2.8 V vs. Li/Li^+ at a current density of 5.92 µA/cm^2 (0.2 C). The circled regions and arrows indicate some regions of interest. Figure 17d shows XRD patterns of pristine V_2O_5 thin films and after cycling to different extents.

Figure 18 shows the potential and corresponding stress results of galvanostatic cycling a V_2O_5 thin film between 4.0 – 2.8 V vs. Li/Li^+ at a current density of 5.92 µA/cm^2 (0.2 C). By using a dense polycrystalline thin film of V_2O_5, the stress here represents the average in-plane stresses intrinsic to V_2O_5 during electrochemical cycling, i.e., as compared with previous studies that use composite materials (with conductive additives and binders) or fabrication techniques that produce non-dense structures (e.g., as in Figure S2b).[37,101,143] Due to the film having a relatively small thickness on the order of nanometres, we expect that the stress is likely uniform in the film. To analyse the results in details, we delineated two regions based on features of interest in Figure 18a. Figure 18b shows an enlarged view in Region 1 during cycles 1-5. Figure 18c shows an enlarged view in Region 2 during cycles 46-50.

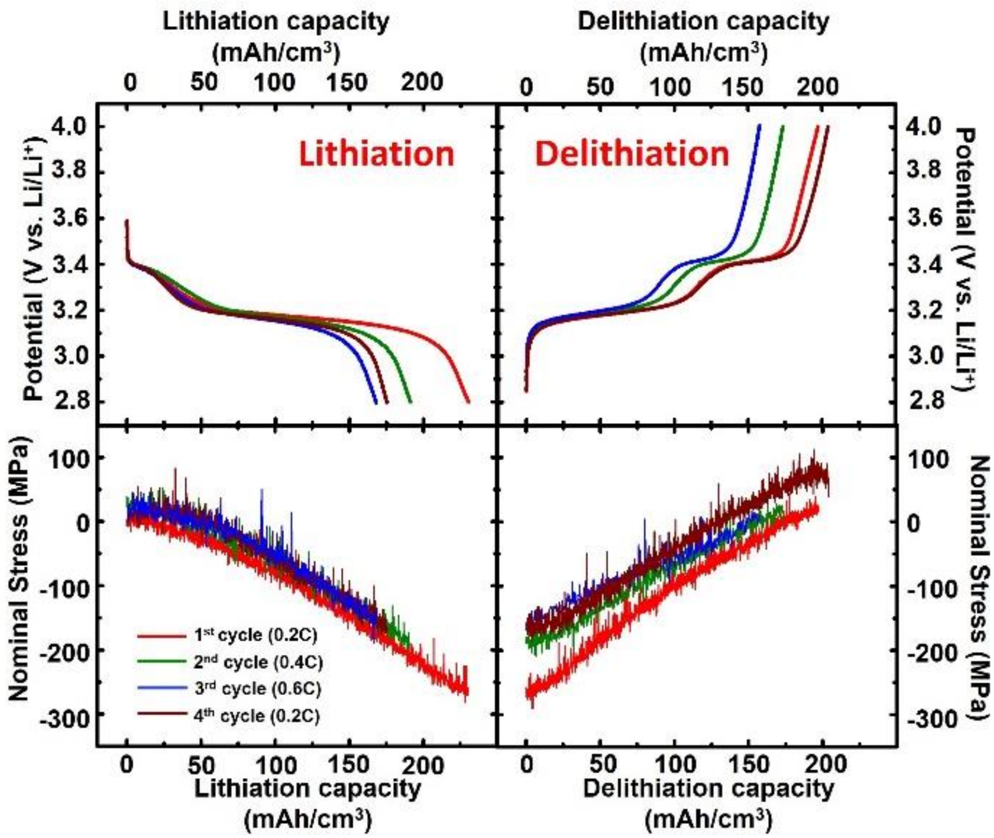

Figure 19 Potential and corresponding stress response during 4 cycles of a V_2O_5 thin film between 4.0 – 2.8 V vs. Li/Li^+ at varying current densities of 5.92 μA/cm^2 (0.2 C), 11.83 μA/cm^2 (0.4 C), 17.75 μA/cm^2 (0.6 C), and 5.92 μA/cm^2 (0.2 C).

To investigate the effects of the charging rate on performance, we cycled a V_2O_5 thin film four times between 4.0 – 2.8 V vs. Li/Li^+ at various current densities (5.92 μA/cm^2 (0.2 C), 11.83 μA/cm^2 (0.4 C), 17.75 μA/cm^2 (0.6 C), and 5.92 μA/cm^2 (0.2 C)), as shown in Figure 19. After the end of the third cycle, we used the same current density as during the first cycle to compare in terms of repeatability.

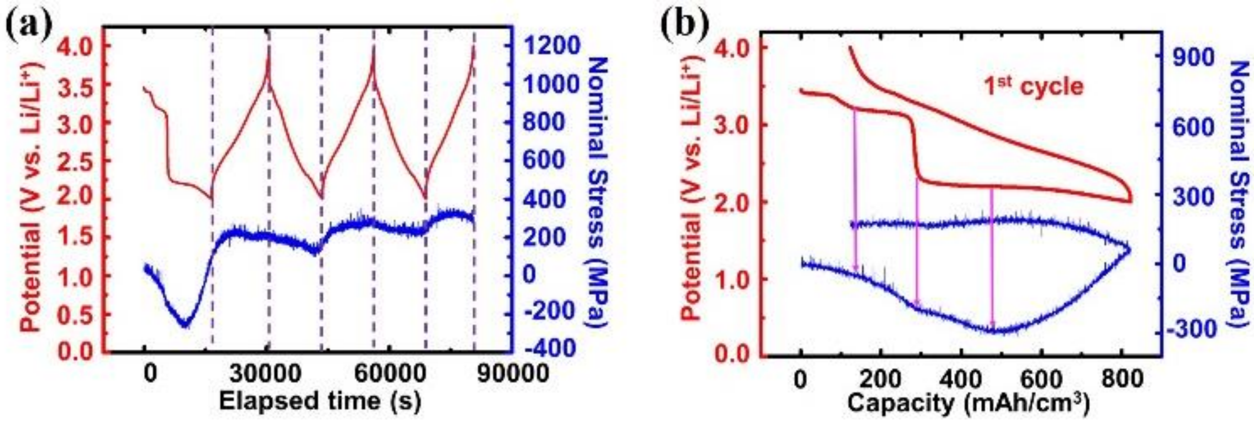

Figure 20 (a) Potential and corresponding stress response during 3 galvanostatic cycles of a V_2O_5 thin between 4.0 – 2.0 V vs. Li/Li^+ at a current density of 5.92 μA/cm^2 (0.2 C). (b) Enlarged view of the first cycle.

Figure 20 shows the potential and corresponding stress during deep galvanostatic cycling of a V_2O_5 thin film between 4.0 – 2.0 V vs. Li/Li^+ at a current density of 5.92 μA/cm^2 (0.2 C). Of particular note, compared with all of the previous results, here we are interested in investigating the stress variation during a transformation from δ-$Li_xV_2O_5$ to γ-$Li_xV_2O_5$, which is known to be an irreversible phase transformation.[47] Likewise, it is important to note that this phase transformation involves volume contraction during lithiation, as indicated in Figure 15.

Discussion

Structure and surface morphology of as-fabricated V_2O_5 thin films

The SEM and AFM studies revealed that the as-fabricated V_2O_5 thin films comprise oriented platelet-like grains spanning a few micrometers. Specifically, over the scans, the variation in height is less than 10% of the total thickness of the film. Figure S1 shows that the roughness of the stainless-steel substrate is on the same order. As such, the roughness of the V_2O_5 thin film likely stems directly from the roughness of the substrate. As a result of this minimal spatial variation in thickness, we can input the thickness of the film measured from profilometery directly into Stoney's equation without any further modifications.[37,101,111] In general, growth of such a flat crystalline thin film is difficult. For instance, by comparison in Figure S2, we show SEM and AFM scans of films fabricated through the more standard approach – high temperature sputtering. The morphology of this latter film produces discrete particles that resemble nanopillars. However, to produce meaningful measurements of intrinsic stress that develop in these systems, we must have thin films that are continuous and as flat as possible, while maintaining crystallinity. As such, our studies show that post-annealing is a key process in fabricating flat thin films from physical vapor deposition.

In addition to surface morphology, we also investigated the crystal structure of the V_2O_5 thin film. Raman spectroscopy provides a means of studying the phase and local structure of V_2O_5 thin films with regard to the structural units and different vibrational modes.[147] As shown in Figure 14c, the low frequency modes at 145 and 196 cm^{-1} are external modes corresponding to the relative motion of $[VO_5]$ square-pyramidal units with respect to each other, thereby reflecting the strength of in-plane bonding vanadium-centered polyhedra. In the medium- and high-frequency regions, Raman bands at 285 and 404 cm^{-1} derive from bond rocking oscillations of the vanadyl oxygen, whereas the Raman band at 304 cm^{-1} can be ascribed to the vibration of intra-ladder oxygen atoms within the lattice. The 485 and 530 cm^{-1} bands are assigned to the bending of O-V-O units and stretching of V-O bonds, respectively. The 707 cm^{-1} band is ascribed to the anti-phase stretching of V-O bonds, whereas the prominent Raman band at 997 cm^{-1} is associated with the stretching mode corresponding to the shortest bond of vanadyl

V=O.[148] Figures 1d and e show results from X-ray diffraction. Figure 14d shows relatively few reflections as compared with the PDF from pristine V_2O_5 powders, thereby suggesting that the sample is a highly-textured V_2O_5 film.[42] The pole figure presented in figure 14e further indicates that the V_2O_5 thin film is indeed highly textured in the (110) direction.

Electrochemical and mechanical performance during galvanostatic cycling between 4.0 - 2.8 V

A multibeam optical stress sensor (MOS) monitored the change in curvature (ΔK) of V_2O_5 thin films during electrochemical cycling. Our previous paper provides details of this experimental setup.[143,144] The results from electrochemical cycling and simultaneous measurements of stresses are shown in Figure 16 and Figure 18. Corresponding results from optical microscopy and XRD characterization are shown in Figure 17. Likewise, Figure S3 (b) shows an SEM image of a V_2O_5 thin film after 50 cycles.

From a structural chemistry perspective, several papers have found that the phase transformations in the 4.0 – 2.8 V range from pristine α-V_2O_5 to δ-$Li_xV_2O_5$ is reversible.[43,44] However, we found that the capacity of the thin film electrode degraded substantially during cycling, as indicated in Figure 16a. Likewise, during the first 10 or so cycles, voltage plateaus occur, which correspond to distinct phase transformations: α-$Li_xV_2O_5$ to ε-$Li_xV_2O_5$ at 3.4 V and ε-$Li_xV_2O_5$ to δ-$Li_xV_2O_5$ at 3.1 V. However, Figure 16a indicates that these plateaus diminish upon extended cycling. From a mechanics perspective, the lithiation-induced volume expansion from pristine V_2O_5 to δ-$Li_xV_2O_5$ is ~11%, as indicated in Figure 15. As such, due to the constraint provided by the substrate, compressive stresses are generated in the thin films during lithiation, as expected (Figure 18). It is important to note that a strain larger than 0.1-1% is considered severe for brittle ceramics, as we expect V_2O_5 may be. However, quite surprisingly, the compressive stress still increases linearly in time (i.e., linearly in capacity), as shown in Figure 18a-c during lithiation during all 50 cycles, thereby suggesting a predominately elastic response of the film. At the end of lithiation, the stress value reached 400-500 MPa, which is on the same order of reported stress values extrapolated from strain measurements via STXM in a previous study.[7] We should note that the absolute value of stress could be somewhat different than the value mentioned above offset by the residual stress induced during fabrication (which was not measured). This value (400-500 MPa) is on the same order of (but smaller than) stressed observed during cycling of Si thin films (~1200 MPa)[12] and Ge thin films (~900 MPa)[35]. These two materials (Si and Ge) are known to exhibit fracture under most conditions during cycling.[9,12,35,101,149–151] Additionally, these two materials represent high-capacity anode systems that undergo much larger volume changes (~300%) than that of V_2O_5 (~11% volume over this capacity range). Despite these differences in volume expansion, the induced stresses are on the same order of magnitude, thereby demonstrating that even in cathode materials with relatively low volume changes, enormous mechanical stresses can be generated during electrochemical cycling. As such, the measurements provided herein underscore the importance of fully characterizing the mechanical performance of all electrode materials in Li-ion batteries prior to practical applications.

With these mechanical issues in mind, we investigated the evolution of mechanical damage in these systems upon cycling. In Figure 17 (a1-a3), we do not observe any obvious evidence of physical damage after the 1st cycle in all of our tested samples (we show images from three such samples in Figure 17). Likewise, as shown in Figure 17d, the diffraction pattern is restored suggesting that the crystal structure appears to remain intact after the first cycle. As shown in Figure 16b, upon further cycling (1-10 cycles, ‘Region 1’), the coulombic efficiency increased significantly from 0.7 to 0.9, which often occurs in lithium-ion batteries during the first few cycles[152–154]. Additionally, the peak heights shown in the differential capacity curves of Figure 16c decreased but without any noticeable shift in the locations (potentials) of the peaks. Additionally, small cracks begin to appear, as shown in locations indicated by the red circles in Figure 17 (b1-b3). Additionally, the color contrast that begins to appear in some regions after 5 cycles may indicate the onset of delamination from the substrate. Still, most of the area of the sample maintains mechanical integrity from cycles 1 to cycle 5 Likewise, our XRD results (Figure 17d) show that after 5 cycles, the reflections are not substantially shifted and only minimal changes in intensity are observed, thereby indicating retention of the integrity of the crystalline phase (α-V_2O_5). Finally, Figure 18b shows that the stress curves maintain the same trend over this cycle range with only a slight downwards shift during each cycle.

During the initial stage of cycling, the battery is still near a "fresh" state of pure V_2O_5. Side reactions, such as the decomposition of electrolyte and growth of solid electrolyte interface on both cathode and anode side may lead to relatively low coulombic efficiencies before reaching a steady value after a few cycles. For instance, Qi et al. found that the electrolyte can decompose, even at ~3.4 V, which can lead to the deposition of so-called cathode electrolyte interface (CEI)[155]. The deposition of CEI on the cathode side may cause the accumulated compression upon cycling observed in Region 1. Additionally, during each cycle, some Li atoms may remain in the cathode after delithiation to 4 V, which would also lead to accumulated compression during cycling. Previous Raman and powder diffraction measurements of nanowires and micron-sized particles have indeed established irreversible lithiation, which results in expansion of the interlayer spacing of V_2O_5.[42] Overall, despite the measured stress indicating nearly linear elastic behavior during each cycle, residual compressive stresses remain after each cycle. In region 1, this produces incrementally increasing levels of compression during cycling.

Upon further cycling (10-50 cycles, ‘Region 2’), the coulombic efficiency seemingly reaches a steady state (Figure 16b). Additionally, as shown in Figure 16c, the peak height from the differential capacity curves not only drops drastically but also shifts (to left during lithiation and to right during de-lithiation). This trend suggests that the internal resistance of the active material increased.[156–158] To further substantiate this trend, we performed electrochemical impedance spectroscopy (EIS), which indicated that the resistance of the active material indeed increases tremendously after 50 cycles (Figure S4). We should note that the majority of the resistance in our battery system comes from the cathode.[159] Additionally, from the optical microscopy images after 50 cycles, (Figure 17 (c1-c3)), active material detaches from the substrate in the form of delamination (e.g., as indicated by the arrow in Figure 17c2). Likewise, large cracks formed (e.g., as indicated by the arrow in Figure 17c3) over large regions of the electrode. Although the phase transformations from pristine α-V_2O_5 to δ-$Li_xV_2O_5$ are commonly regarded as reversible,[43,44] here we observed that mechanical degradation can still occur during these transformations in the form of fracture, delamination, and concomitant loss in contact after extended cycling. Likewise, from the XRD results shown in Figure 17d, the reflections are substantially diminished in intensity after 50 cycles as a result of material loss from the substrate. Additionally, we did not detect any new reflections which would indicate the appearance of any new crystalline phases or local nucleation of highly lithiated domains. Generally speaking, amorphization and/or the observed significant loss of active material via detachment from the substrate (Figure 17c) represent potential sources of this decay of the XRD intensity and the changes in internal resistance. Correspondingly, in Region 2 of Figure 18a, the amplitude of the stress change decreases with increasing cycle number. Figure 18c shows an enlarged view of the behavior for cycles 46-50. Fracture, delamination, and concomitant loss in contact with the current collector all lead to this observed decrease in the measured levels of changes in stresses during each cycle (Figure 18). We should also note that delamination and fracture can also influence our measured values of the stresses. As such, quantitative interpretation of the data at large cycle numbers is somewhat convoluted by the mechanical damage. However, it is still quite indicative of what is occurring qualitatively (e.g., the changes in stress during each cycle get smaller with further cycling).

In summary, despite the relatively small volume changes (e.g., as compared to anode materials) and phase transformations that are generally regarded as reversible in literature (i.e., reversible structure/chemistry), extensive structural and mechanical damage can still occur in V_2O_5 thin films, thereby leading to loss of active material and associated capacity fade during extended electrochemical cycling.

Effects of varying current density on electrochemical and mechanical performance

Upon changing the current density, we did not observe any changes in the slope of the stress profile, as shown in Figure 6. Using different current densities effectively imposes different strain rates on the material, i.e., larger current densities induce larger volumetric changes per time. As such, for current densities of practical relevance to real battery systems, this material does not exhibit any marked mechanical strain-rate sensitivity, despite such effects having been observed in other materials.[106,160,161] Additionally, during 4th cycle, when we changed the current density back to the initial value (5.92 μA/cm^2 (0.2 C)), the stress at the end of lithiation is smaller than at the end of the initial lithiation. However, the slopes of the curves are still almost identical.

This trend occurs due to the fading of the capacity during cycling. During the 4th cycle, the material exhibits a smaller capacity, i.e., it is lithiated less, and as such, a smaller stress is induced. We also note that a moderate level of tension occurs (Figure 6) after subjecting this sample to various current densities. This tension may stem from a number of sources including slight plastic deformation, additional CEI formation at larger current densities, or delamination releasing residual compressive stresses induced during fabrication.

Effects of deep discharge (4.0 - 2.0 V vs. Li/Li$^+$) on electrochemical and mechanical performance

We examined the effects of deep discharge of the pristine V_2O_5 thin film battery to a voltage range (4.0 – 2.0 V) known to induce an irreversible phase transformation (to γ-$Li_xV_2O_5$)[47]. The phase transformation from δ-$Li_xV_2O_5$ to γ-$Li_xV_2O_5$ is predicted to induce ~7% volume contraction as a result of the orthogonal rotation of two square-pyramidal VO_5 units in opposite directions, despite additional lithium insertion, as indicated in Figure 15. Such a phase transformation defines tetrahedral environments for Li-ions. Interestingly, the phase transformation from δ-$Li_xV_2O_5$ to γ-$Li_xV_2O_5$ (observed at ~2.2 V) initially induces relative compression of the film, followed by relative tension upon further lithiation. De-lithiation initially induces relative tension, followed by a stress profile that is nearly flat. The difference of stresses after the first cycle is indicative of plastic deformation, i.e., a relatively large residual tensile stress remains after the first cycle. Such large tensile stresses can potentially induce fracture, particularly in relatively brittle materials (as we expect V_2O_5 to be). In the following cycles, no obvious voltage plateaus exist, thereby suggesting that subsequent lithiation/delithiation occurred in solid solution (no two-phase coexistence), attesting to irreversible transformation to a γ-$Li_xV_2O_5$ phase followed and cycling between this discharged phase and the empty γ' metastable phase of V_2O_5[44]. Additionally, the stresses are relatively small in these cycles as compared to the first cycle. It appears likely that significant mechanical and structural damage occurs during deep discharge as a result of the energy dissipative distortive structural transformation, which warrants further investigation but is beyond the scope of this paper.

Conclusions

In this work, we have shown that significant stresses arise during electrochemical cycling of V_2O_5 thin film cathodes. Extended cycling leads to accumulated mechanical damage (e.g., fracture, delamination) and structural changes (e.g., amorphization), which ultimately result in severe capacity fade. Despite the relatively small volume changes in cathodes during cycling, the observations provided herein highlight the intimate coupling between electrochemistry and mechanics in cathodes of lithium-ion batteries. Our results imply that mechanical and/or electrochemical processes can lead to their degradation, ultimately producing capacity fade. Specifically, in terms of electrochemistry, parasitic reactions during cycling (decomposition of electrolyte, deposition of CEI and SEI, etc.) may consume active materials or lead to irreversible structural changes (e.g., amorphization). In terms of mechanics, stresses generated during cycling may produce fracture or delamination, increasing resistivity and/or directly leading to loss of active materials. Likewise, stresses may accumulate during extended cycling, ultimately becoming large enough to induce chemo-mechanical damage in the system and correspondingly leading to significant capacity fade. Overall, beyond presenting fundamental behavior specific to V_2O_5 systems, we hope that this study will provide a general cautionary message to battery researchers in designing next-generation cathodes. In particular, in characterizing new materials, we believe that in addition to performing standard chemical and electrochemical analysis, it is equally as important to perform comprehensive mechanical evaluation, thereby ensuring that the battery is robust over extended cycling.

CHAPTER V

EVOLUTION OF STRESS AND MECHANICAL PROPERTIES OF VO2 THIN FILMS DURING METAL-INSULATOR TRANSITIONS

Abstract

Vanadium dioxide has emerged as a promising candidate material to emulate neuronal logic and memory functions for neuromorphic computing applications, owing to its pronounced metal-insulator transition near around 340K. For viable implementation into practical devices, it is important to understand the mechanical behavior of VO_2 during this phase transition, e.g., as to mitigate damage. In this work, we perform comprehensive mechanical testing on polycrystalline VO_2 thin films. We implement nanoindentation to quantify the hardness and elastic modulus of the VO_2-M and VO_2-R thin films at two representative temperatures (25°C and 85°C). We also measure stresses that arise in VO_2 thin films during its metal-insulator transition using a multibeam optical sensor in-situ during temperature sweeps. We observe that tensile stresses develop in the film upon heating through the phase transformation, which is somewhat counterintuitive given the known volumetric expansion associated with this transformation. We explain this phenomenon through structural analysis. Also informed by these experimental results, we use linear elastic fracture mechanics to predict a critical film thickness, below which our sputter-deposited polycrystalline VO_2 films will not fracture. This analysis has implications in highly constrained systems, as are often encountered in packaged electronic devices, e.g., in layered structures. We also investigated the influences of thermal cycle rate, partial (incomplete) thermal cycles, and extended cycling on the stress accumulation during the phase transformation. Overall, this detailed mechanical study can provide practical guidance towards implementing VO_2 in devices while maintaining structural integrity during operation.

Introduction

Electron-correlated transition metal oxides exhibiting pronounced metal-insulator transitions (MIT) are excellent candidates to emulate the spiking behavior of biological neurons. VO_2 undergoes a first-order diffusionless and hysteretic transition from a high-symmetry rutile R phase to a low-symmetry stable M_1 (or metastable M_2/M_3) phase around T_c=340K.[57–61] Stemming from this behavior, Yi *et al.* demonstrated 23 types of biological neuronal behaviors through two channel devices of VO_2 as active memristors[62]. Much attention has focused on tuning the transition temperature, e.g., through adding dopants, tuning epitaxy, and changing film thickness[63–66] Still, VO_2 often suffers severe mechanical damage during thermal cycling.[67–73,162] For instance, Nagashima et al. has reported fracture of epitaxial VO_2 thin films on TiO_2 (001) substrates.[162] Implementation of VO_2 into robust devices of practical utility requires a comprehensive understanding of the mechanical properties, as to ensure extended service life. A few studies have measured the mechanical properties of VO_2 thin films and nanowires. Swain et al. reported the "composite" modulus of polycrystalline VO_2 thin films on silicon as 140-170 GPa and epitaxial VO_2 films on sapphire of 240-260 GPa using nanoindentation at room temperature.[163] The "composite" modulus in Swain's studies includes contributions from both the film of interest (VO_2) and the substrate (Si or sapphire). Minor et al. estimated the elastic moduli of VO_2-M_1 and M_2 nanowires to be 128±10 GPa and 156±10 GPa through tensile tests inside a TEM.[164] Singh et al. surveyed literature and found the elastic modulus of the insulating M_1 phase as ranging from 100 GPa to 308 GPa from various experiments and first-principles studies.[165] Herein (in contrast to the existing data from nanoindentation), we utilize the Hay-Crawford thin film model that can remove the influence from the substrate on nanoindentation data.[166] Beyond determining basic mechanical properties of VO_2, it is also important to determine stress levels that develop in physically constrained environments during the metal-insulator transitions, as to guide the design of practical devices that avert damage during operation.

In this study, we perform nanoindentation on sputter-deposited thin films of VO_2 in both the VO_2-M (25°C) and VO_2-R (at 85°C) phases. We then implement a multi-beam optical stress sensor technique to monitor evolution of stress in-situ during thermal cycling through the metal-insulator phase transition. Informed by the measured elastic modulus and accumulated stress during the thermal cycle, we implement an analysis from fracture mechanics to predict a critical film thickness, below which fracture will not occur during a thermal cycle. We compare these predictions to experimental observations by thermal cycling VO_2 films of varying thickness while simultaneously monitoring damage evolution. We also investigate the effects of heating rate and cycle characteristics on the stress history and performed some extended cycling testing while monitoring stress and damage in this system. Overall, our detailed mechanical studies provide insight into the design of mechanically robust neuromorphic computing devices.

Experimental Details

Sample preparation of VO_2 thin film

We utilized two side mirror-polished <100> silicon wafers with 150 nm of thermal oxide (SiO_2) on top (University Wafer) and TEM grids with 18 nm-thick SiO_2 support films as the substrates. The substrates (except TEM grid) were cleaned with acetone and isopropanol and placed into a sputtering system (AJA Inc.) with a base pressure of ~5×10^{-8} Torr. First, we increased the temperature of the substrate holder to 600°C. Next, the sputtering system deposited materials from a pristine vanadium target using a pressure of 2.0 mTorr with a mixture of argon and oxygen gas (Ar: 20 sccm, O_2: 4.1 sccm) and a DC power of 200 W. During the deposition, we monitored the voltage on the metal vanadium target to ensure it remained stable. After deposition, we annealed the sample in the same sputtering chamber without breaking vacuum at 600°C for 3 hours. We measured the film thickness by milling a trench on the as-prepared sample using a focused ion beam source inside a scanning electron microscope (SEM, Tescan LYRA-3 Model).

Structural and morphological characterization

A parallel beam geometry using a Bruker-AXS D8 X-ray diffractometer with a Cu Kα (wavelength $\lambda = 0.154$ nm) radiation source produced X-ray diffraction patterns. A scanning electron microscope (SEM, JEOL JSM-7500F) operating at 10 kV captured the surface morphology. An atomic force microscope (AFM, Bruker-Dimension Icon) determined the morphology and roughness of the surface of the electrode. We conducted XPS analyses with an Omicron XPS/UPS system. The system maintained at a base pressure of $1*10^{-9}$ mBar during operation. A DXS 500 optical microscope captured images of the surface of the sample after thermal cycling to determine damage evolution. An Olympus BX 41 microscope equipped with Horiba Jobin-Yvon LabRam HR instrument was used to acquire Raman spectra with excitation from a 633 nm laser excitation line.

Mechanical characterization

A multibeam optical stress sensor (MOSS) from k-Space Associates monitored the curvature of the substrate (ΔK) during thermal cycling. The experimental setup is shown in the graphical abstract. We spread thermal paste on a heating stage (TMS 94, Linkam Scientific Instruments

Ltd) prior to mounting the sample, as to increase heat conduction. Using Stoney's equation, we deduced the average in-plane stresses in the thin film during thermal cycling[143,167]:

$$\sigma_f = \sigma_r + \frac{E_s h_s^2}{6h_f(1-\nu_s)}\Delta K \quad (1)$$

where E_s is the elastic modulus of the substrate ($E_s = 190$ GPa), h_s is the thickness of the substrate ($h_s = 325$ µm), ν_s is the Poisson's ratio of the substrate ($\nu_s = 0.2$), h_f is the thickness of the VO_2 film ($h_f = 150$ nm), and σ_r is the residual stress in the film from sputter deposition and annealing, which was measured through x-ray diffraction, and can be expressed as[168,169]

$$\sigma_r = \frac{E_f}{(1+\nu_f)}\frac{1}{d_0}\left(\frac{\partial d_{\phi\psi}}{\partial sin^2\psi}\right) \quad (2)$$

where E_f is the elastic modulus of the VO_2 thin film, ν_f is the Poisson's ratio of the thin film (ν_f = 0.2) we assume the value of Poisson's ratio equals to 0.2 as it is a common value for ceramic, d_0 is the lattice spacing in an unstressed condition (d_0(011) = 3.20672 Å),[170] and $d_{\phi\psi}$ is the d-spacing measured in a stressed sample that was tilted by an angle ψ. In this study, the stress σ_f represents the average in-plane engineering stress. Any expansion or contraction out of plane will not contribute to the stress measurement. We use the sign convention for compressive stress as being negative and for tensile stress as being positive.

Nanoindentation

We measured mechanical properties with a Nanomechanics Nanoflip indentation system operated in a temperature chamber. Specimens from Si wafers (only) as well as specimens from VO_2 films sputtered onto Si wafers were mounted using cyanoacrylate adhesive prior to indentation. All measurements of hardness, H, and elastic modulus, E, were performed with a Berkovich triangular pyramid indenter using the continuous stiffness measurement technique

(CSM) with a target dynamic root-mean-square amplitude of 2 nm and loading rate by load ($\dot{P}/P$) value of 0.05 s^{-1}. The tip area function was calculated based on fused silica at indentation depths between 100 nm and 450 nm. The machine frame stiffness was calculated based on indentation of a reference Si substrate at the same temperatures of the relevant measurements. Holding the indenter tip against the sample and measuring the displacement versus time enabled assessment of thermal equilibrium for the tip and sample. All indentation measurements were taken only after the thermal drift was measured as less than 0.05 nm/s. Hardness and apparent elastic modulus values were calculated using the Oliver-Pharr approach.[171] The elastic modulus of the VO_2 film on the Si substrate was calculated based upon the Hay-Crawford thin film model.[166] To this end, the Si substrate's elastic modulus versus depth was measured directly over 50 individual tests, with the average elastic modulus interpolated at 5 nm increments in depth. This substrate modulus versus depth was then applied in calculating the film modulus versus depth using the Hay-Crawford model, adopting a film thickness of 1.63 μm measured from FIB cross section images, and a substrate and film Poisson ratio of $\nu = 0.2$.[166] This technique was applied independently at 25°C and 85°C.

Results

Morphological and Structural Characterization

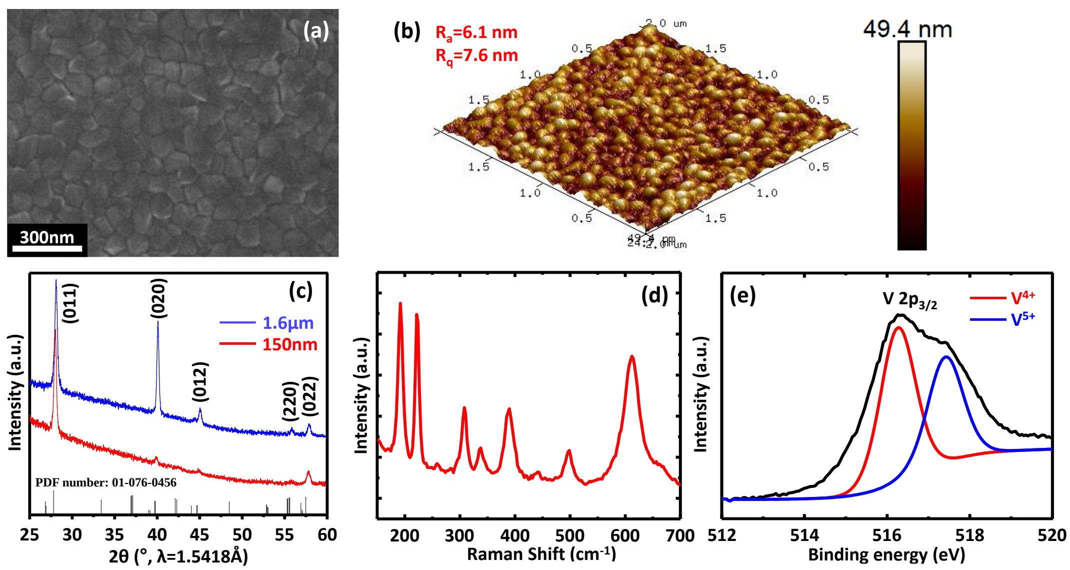

Figure 21 Surface morphology and crystal structural characterization of 1.63 µm-thick VO_2 thin films: (a) SEM image, (b) AFM scan over a 2 µm by 2 µm region, (c) X-ray diffraction patterns of as-deposited films of two thicknesses on silicon substrates with SiO_2 thermal oxides, (d) Raman spectroscopy, (e) X-ray photoelectron spectroscopy.

Figure 21 shows the surface morphology and crystal structure of 1.63 µm-thick sputter-deposited polycrystalline VO_2 thin films through various characterization techniques. In Figure 21a, the SEM image shows a grain size of approximately 100 nm. AFM results in Figure 1b show the surface roughness over a 2 µm by 2 µm region. The R_a value and R_q value are 6.1 nm and 7.6 nm, respectively. The roughness values indicate the film roughness is three orders of magnitude smaller than the total film thickness. This information ensures that Equation (1) is valid without any required modification.[111] Figure 21c displays the x-ray diffraction pattern of both a 1.63 µm-thick and a 150 nm-thick VO_2 thin film. The vertical black lines in Figure 21c indicate the diffraction pattern of powder VO_2-M with PDF number: 01-076-0456. All the indexed crystal peak shift to the right, as compared with results from powder VO_2; this finding indicates residual stress in the sample that arises from the entire deposition process, which includes deposition (film growth) itself, thermal mismatch between the substrate and the film during cooling to room temperature, and the phase transformation that occurs during cooling. For the thinner film, the VO_2-M (011) reflection became more dominant relative to the (020) reflection. Raman spectroscopy in Fig. 21d shows eight bands that match with a previous study of polarized Raman spectra of VO_2, based on phonon state calculations and several experimental results.[172–174] Figure 21e provides x-ray photoelectron spectroscopy (XPS) analysis of the V2p spectral doublet ($V2p_{1/2}$ and $V2p_{3/2}$). The $V2p_{3/2}$ peak found near 517 eV indicates the presence of VO_2. We quantified the oxidation states of V utilizing $V2p_{3/2}$, which indicates a dominate V^{4+} oxidation state (78$\pm$1%), and the remainder being the V^{5+} state. Since XPS only captures information several nm deep from the surface of the film, the V^{5+} state was possibly due to a native oxide after the films were exposed to air. Figure S5 displays the resistance change of a VO_2 thin film during the heating/cooling process. The results indicate nearly two orders of magnitude of switching in resistance during the phase transformation. The relatively low on/off ratio compared with single crystal VO_2 thin film may stem from some current leakage through pinholes in the 150 nm thermal oxide layer on top of silicon wafer or from grain boundaries in the polycrystalline sample, which serve as scattering sites during electron transport.

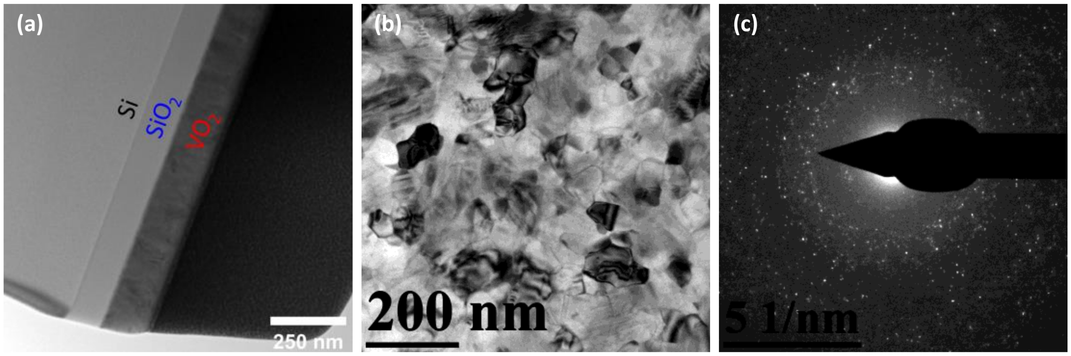

Figure 22 Transmission electron microscopy and electron diffraction pattern of a 150 nm-thick VO_2 thin film grown on an SiO_2/Si substrate. (a) Cross-sectional bright-field transmission electron microscopy (BF-TEM) image of the VO2 sample prepared by focused ion beam (FIB). (b) Top-view of a polycrystalline VO_2 thin film grown on TEM grid with a 18 nm-thick amorphous-SiO_2 layer as a support. (c) Corresponding selected area electron diffraction (SAED) pattern of VO_2 thin film, indicating the nanocrystalline nature of our as-deposited films.

Figure 22 displays the morphology and diffraction pattern of a 150 nm-thick VO_2 thin film from transmission electron microscopy (TEM). Figure 22a shows the cross section of a 150nm-thick VO_2 thin film deposited on Si wafer with 150 nm thermal oxide (SiO_2). This image indicates the film is flat without any discernible bulges or pits. Figure 22(b) shows a top-view of a film deposited on a TEM grid. The selected area electron diffraction (SAED) patter in Figure 22(c) indicates the nanocrystalline nature of the as-deposited film.

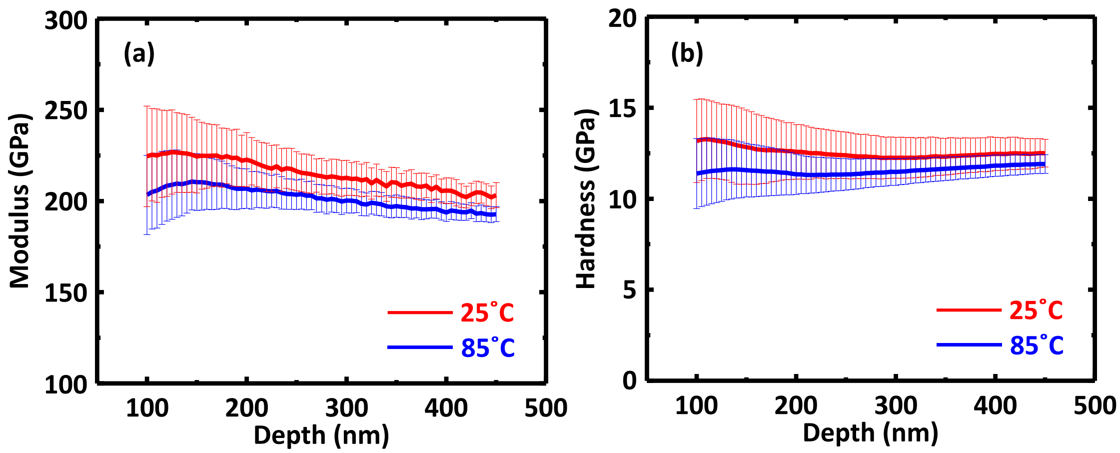

Figure 23 Nanoindentation tests with the curves representing the average of 16 and 50 tests at 25°C and 85˚C, respectively and the error bars representing the standard deviation. (a) the elastic modulus of the VO_2 film. (b) The hardness of the film.

Figure 23 displays the modulus and hardness of the VO_2 film as a function of the indenter depth. Representative load and depth curves for both room temperature (25˚C) and high temperature (85˚C) are shown in Figure S2. At an indentation depth of 150 nm, the elastic modulus is 224 $\pm$ 20.0 GPa at 25 ˚C and 210 $\pm$ 15.5 GPa at 85˚C. An unpaired t-test gives a p-value of 0.0048, meaning that despite the error bars appearing similar in magnitude to the difference between the mean values for the two temperatures, the modulus is indeed statistically different for the two sample sets.

Indentation hardness measurements at 150 nm depth yielded values of 12.8$\pm$2.0 GPa at 25˚C and 11.6 $\pm$1.5 GPa at 85 ˚C. An unpaired t-test for this data produces a p value of 0.0084, indicating that this data is again statistically distinct. Given that the moduli for the film and substrate are similar (~195 GPa versus ~220 GPa), and that Si's hardness was measured as near 13.5 GPa, we can reasonably assume that the apparent hardness represents that of the film to better than 5% accuracy.[175]

Morphological Evolution during Thermal Cycling

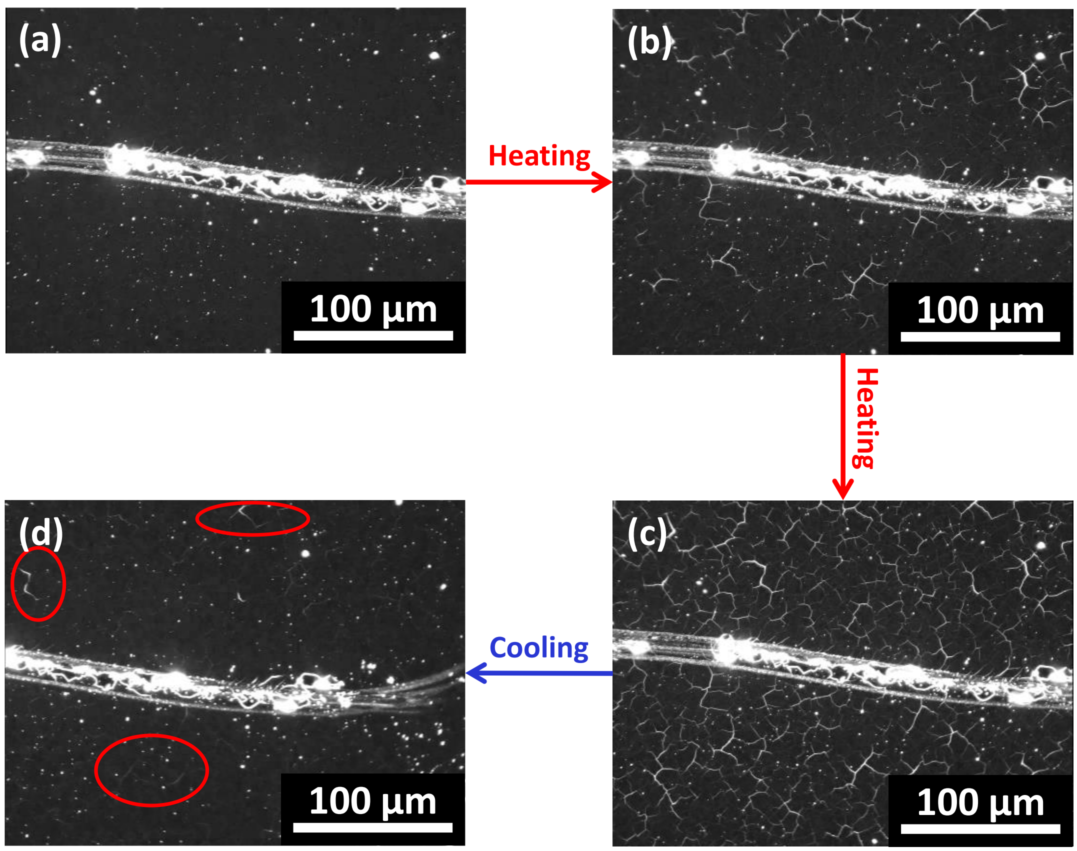

Figure 24 Optical microscopy images of a 1.63 µm-thick VO2 thin film during the first thermal cycle ranging from 40˚C to 90˚C to 40˚C. A scratch made with a diamond scribe to nucleate cracks from its sidewalls runs through the middle of each image. (a) represents the start of heating, and (d) represents the end of cooling. (b) and (c) are the intermediate points chosen based on observations of interesting morphological features. The red circles in Figure 24(d) highlight areas of interest.

Fig. 24 shows optical images of the morphology evolution of a 1.63 μm-thick VO_2 thin film during heating and cooling. We used a diamond scribe to create a scratch in the sample with cracks emanating from its sidewalls, as seen as running left-to-right in the images. This pre-cracking ended up being unnecessary as cracks nucleated and propagated not only near the scratches induced by diamond scribe but also regions further away from the scratches, as shown in Figures 24b-d. At the end of the cooling process (Figure 24d), the fractured regions seem to largely disappear. However, they actually remain, as highlighted by the red circles in the figure. Gaps between the crack faces likely fill in during cooling but actual chemical bonding does not occur between the two crack faces, i.e., the damage persists.

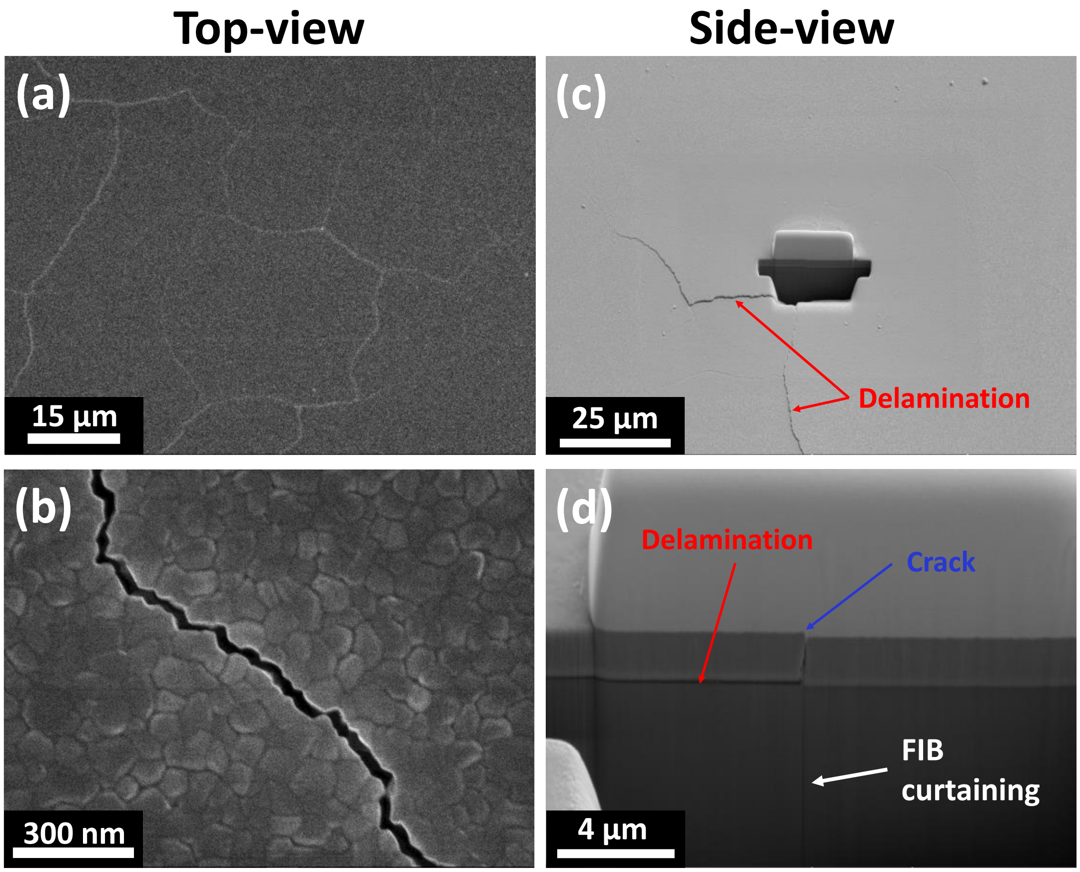

Figure 25 Scanning electron microscope images of 1.63 µm-thick film after the first thermal cycle. (a) and (b) show the top-view morphology. (c) and (d) show the side-view morphology cut by focused ion beam.

Figure 25 shows top-view and side-view images of a 1.63 µm-thick VO_2 film that fractured during a thermal cycle. The top view image indicates the film fracture is predominately intergranular. More top-view images of cracked films are included in Figure S3. The side-view image revealed both fracture and delamination between the VO_2 film and the underlying substrate in the damaged regions.

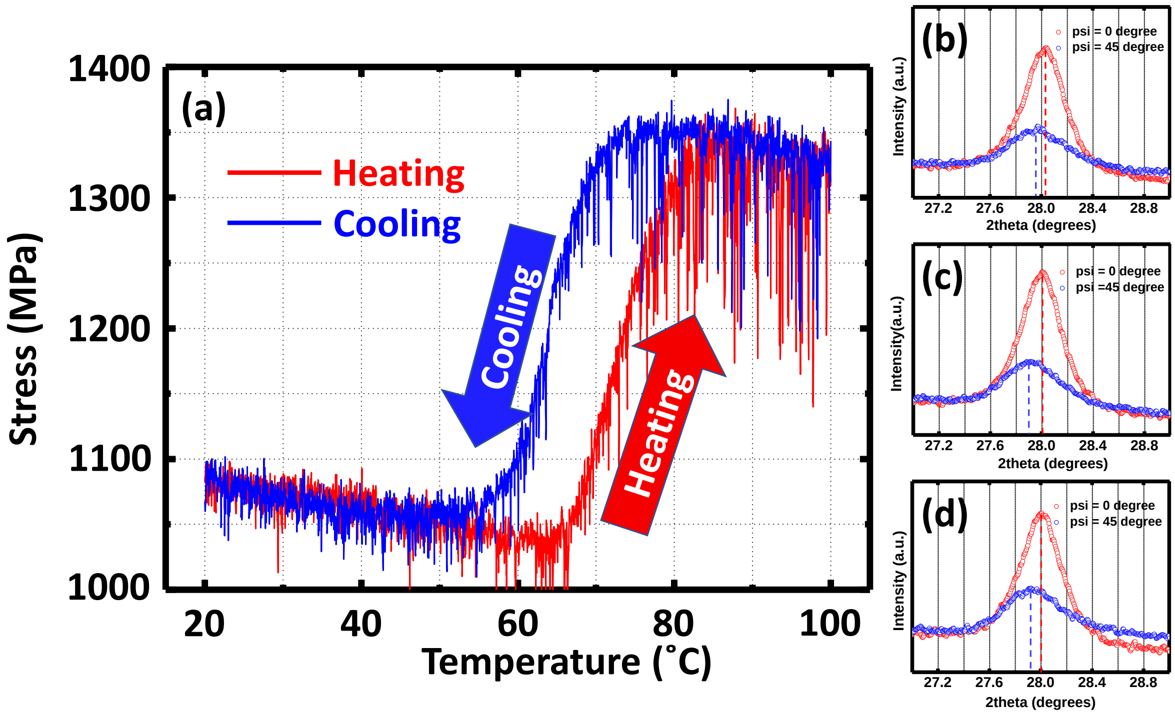

Figure 26 (a) In-situ evolution of stress during a thermal cycle from 20˚C to 100˚C to 20°C at a heating and cooling rate of 4˚C /min. (b)-(c) Three representative XRD coupled scans of VO_2 thin films at two different chi angles (psi = 0˚ and psi = 45˚).

Figure 26(a) shows an in-situ measurement of stress evolution of 150 nm VO_2 thin film during a thermal cycle at a heating/cooling rate of 4˚C /min. Figure 26(b)-(c) displays XRD coupled scans of the VO_2-M (011) plane at psi = 0˚ and psi = 45˚. We adopted $\sin^2\psi$ method (Equation 2) to measure the residual stress of the as-deposited film.[168,169] The films we fabricated are textured polycrystalline thin films. In our 150-nm thick films, the major set of crystal planes that are parallel to the surface of the substrate (in-plane) are the VO_2-M (011) planes as indicated in

Figure 21(c). The peak shifts of the XRD coupled scans in rotating to two different psi angles indicate a residual stress of $\sigma_r = 1.083 \pm 0.076$ GPa through Equation (2). The indentation hardness was measured as around 12 GPa in Section 3.2. As per the Tabor relation,[176] $\sigma_y \sim H/3$, the yield stress is around 4 GPa. As such, we note that the residual stress in the film is quite large here but still well below the yielding point.

Figure 26(a) shows that upon heating from 40˚C to 65˚C, small compressive stresses are generated in the VO_2 films due to the thermal mismatch of VO_2 and the Si substrate[177,178]. Upon further heating, significant tensile stresses (around 300 MPa) build up in heating from 65 ˚C to 80 ˚C through the metal-insulator transition. Upon completion of the phase transformation (above ~85˚C), the thermal mismatch between VO_2 and the Si substrate again produces further compression. Likewise, the stress evolution during cooling shows a similar trend, albeit with the metal-insulator transition temperature during cooling being located at a lower temperature range. The stress accumulation during phase transformation is near 300 MPa. The resistance/thermal hysteresis of VO_2 thin film/powder has been well studied using probe stations and differential scanning calorimetry during thermal cycling.[57,63–66] Our results similarly indicate that VO_2 displays stress hysteresis during thermal cycling through the phase transition.

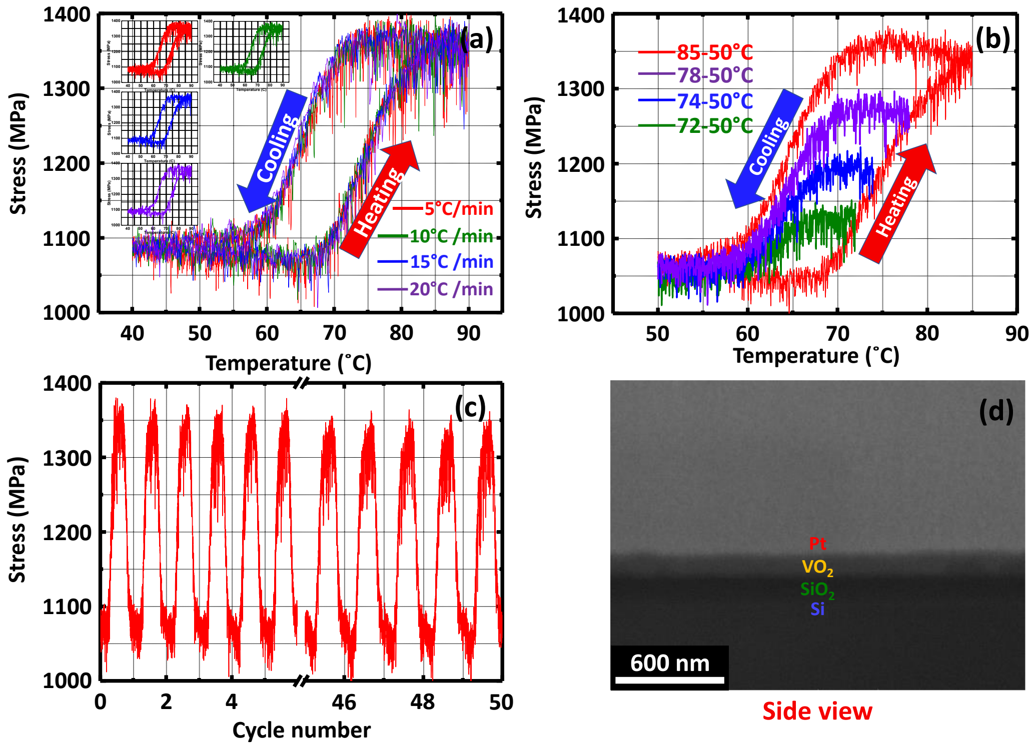

Figure 27 (a) In-situ stress evolution of a VO_2 thin film during thermal cycling from 40˚C to 90˚C at various heating/cooling rates. (b) Stress evolution upon heating and cooling at different temperatures T_c (incomplete heating) at a heating/cooling rate of 1˚C /min. (c) Stress evolution during 50 thermal cycles. (d) Cross section SEM image of the as-cycled sample from (c).

Figure 27(a) shows thermal cycling of a 150 nm-thick VO_2 thin film at various heating and cooling rates, ranging from 5˚C/min to 20˚C/min. The inset in the top left corner shows the four discrete cycling curves. No significant differences exist among the curves at different thermal cycle rates.

Figure 27(b) shows experiments in which we heated up a VO_2 thin film to different temperatures, T_c, (72˚C, 74˚C, 78˚C, and 85˚C), followed by cooling down the sample to 50˚C at 1˚C /min. During the cooling period, all curves are relatively flat at first (indicative of hysteresis), after which the stress starts to decrease with various slopes. The temperature range of the flat region during cooling increases with larger T_c, as does the slope of the stress-strain curve upon cooling below the flat (hysteretic) region.

Figure 27(c) shows 50 thermal cycles of a VO_2 thin film between 50˚C to 85˚C at a rate of 10˚C/min. The stress evolution during a cycle did not show any obvious changes after 50 thermal cycles. In Figure 27(d), we utilized FIB to examine a cross section of the as-cycled sample. The side view reveals no obvious mechanical damage either in terms of fracture or delamination, e.g., as compared with the damage produced during thermal cycling of the 1.63 μm-thick film shown Figure 25.

Discussion

Crystal Structure Analysis

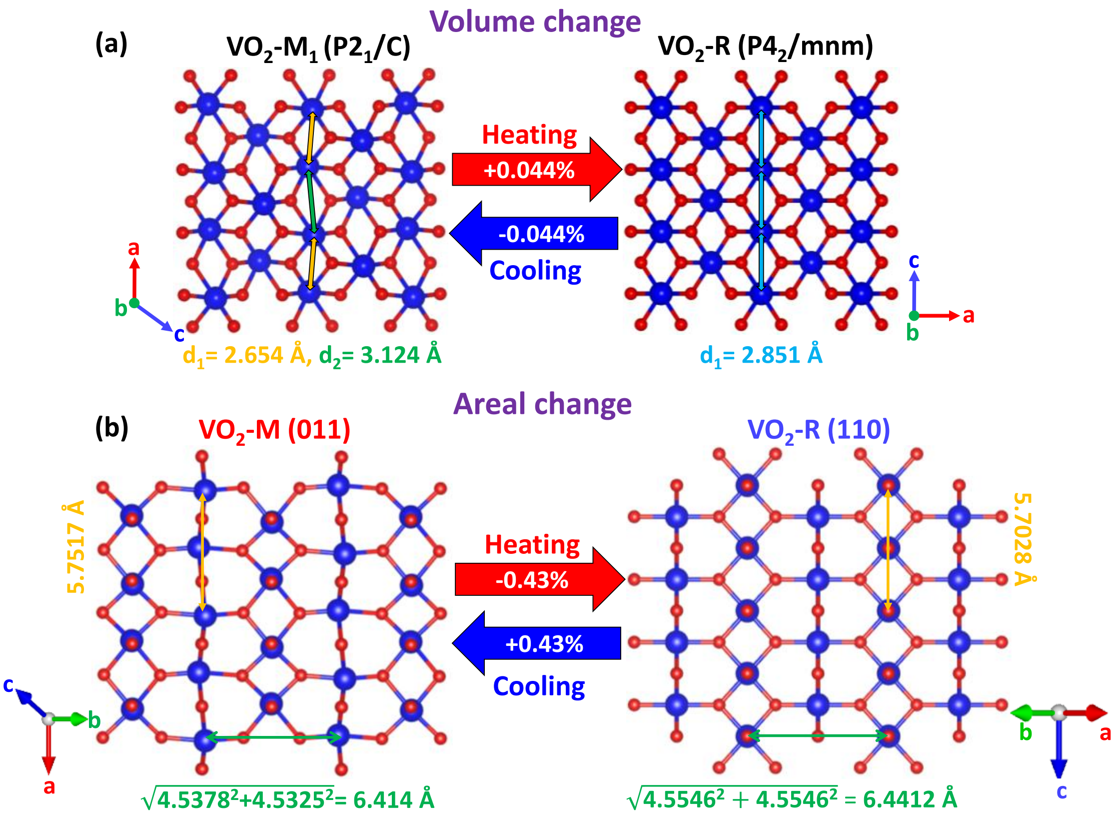

Figure 28 (a) Volume changes between the VO_2-M and VO_2-R phases during the phase transformation. The crystal structures of the VO_2-M is from reference[[170]] and VO_2-R phases is from reference[[179]]. (b) Areal changes between the VO_2-M (011) plane and the corresponding VO_2-R (110) plane during the phase transformation. These planes correspond to the primary orientation of the VO_2 film that are parallel to the substrate (i.e., the in-plane orientation of the film), as indicated through XRD results.

Figure 28(a) shows that the high temperature rutile phase VO_2-R ($P4_2/mnm$) has a singular V-V bond distance (d_1=2.851Å), as compared with the low temperature monoclinic phase VO_2-M ($P2_1/c$), which has alternating dimerized V-V chains (d_2=3.124 Å and d_1=2.654 Å).[59] During heating through the phase transition during, the volume expansion has been reported as

0.044%[177,180]. However, the XRD results (Figure 21c) show that we have a textured film, with most of the crystal planes that lie parallel to the substrate being $(011)_M$, particularly for the thinner film (150 nm). Indeed, several other studies have demonstrated that deposition of VO_2 most commonly results in a textured film with the VO_2-M(011) planes being predominately parallel to the substrate, [181–186] likely because the $(011)_M$ plane possesses the lowest surface energy in the VO_2 crystal system. [187–189] As shown in Figure 28, the a-axis in VO_2-M (denoted as the c-axis in VO_2-R) contracts by 0.85% upon transforming to VO_2-R, while the corresponding in-plane direction perpendicular to this direction (also in the plane of interest, as shown as the vertical direction in Figure 9) expands by only 0.424%. Overall, Figure 28(b) shows that VO_2 $(011)_M$ produces in-plane areal shrinkage during the transition. To reiterate, the stress we measured through the MOS technique represents the average in-plane stress. The expansion/contraction out of plane will not contribute to the stresses that develop in this film/substrate geometry. As mentioned above, the majority of the crystal planes in the VO_2 film that are parallel to the substrate undergo areal contraction during phase transformation. This crystal structure analysis explains our stress evolution measured in Figure 26 and 27, in which we observe relative tension during heating through the phase transition. This analysis highlights the importance of texturing of films in its corresponding influence on stresses that will develop during thermal cycling, which has key implications in practical devices. In terms of crystal structures of VO_2, the relative orientation in-plane and out-of-plane will govern whether tensile or compressive stresses build up in these constrained geometries, e.g., as are typical of multi-layered structures in devices. Delamination between VO_2 and surrounding layers may be driven by either compression or tension in the VO_2. Fracture of VO_2 itself will be driven by tensile stresses. As such, damage may be mitigated or prevented by strategically texturing film/layers of

VO_2 in devices. We will elaborate on designing a mechanically robust thin film in the following section.

Prediction of Critical Film Thickness to Avert Fracture

The nanoindentation and MOS studies provide two important mechanical properties (E_f and σ_f) that can help quantify the critical conditions for fracture of a thin film of VO_2 on a constraining substrate (or correspondingly of such a film surrounded by other materials in a device). For a given stress, σ_f, that develops in the film, there exists a critical film thickness, h_{cr}, below which growth of a pre-existing channel crack becomes energetically unfavorable. To determine the critical thickness, we adopt the fracture mechanics analysis of Beuth[12,190],

$$h_{cr} = \frac{E_f \Gamma_f}{Z(1-\upsilon_f{}^2)\sigma_f{}^2} \tag{3}$$

E_f is the elastic modulus of the film, υ_f is Poisson ratio of the film, Γ_f is the fracture energy of the film, σ_f is the stress in the film (that arises from fabrication (which includes deposition, annealing, and cooling to room temperature) and from heating through the phase transformation), and Z is a dimensionless factor that depends on the material properties of the film and the substrate, as well as the geometry of the crack. For a single channel crack through the thickness of a film, Z is given by

$$Z = \frac{1}{2}\pi g(\alpha, \beta) \tag{4}$$

where $g(\alpha, \beta)$ is a function of Dundurs parameters, α and β, which are defined as

$$\alpha = \frac{\bar{E}_f - \bar{E}_s}{\bar{E}_f + \bar{E}_s}, \ \beta = \frac{\mu_f(1-2\upsilon_s) - \mu_s(1-2\upsilon_f)}{2\mu_f(1-\upsilon_s) + 2\mu_s(1-\upsilon_f)} \tag{5}$$

where the $\bar{E}_i = \frac{E_i}{1-\upsilon_i^2}$ represent the plane-strain moduli, and the $\mu_i = \frac{E_i}{2(1+\upsilon_i)}$ represent the shear moduli.

For an estimate of the critical film thickness for fracture based on Equation (3), we implement the material properties and stresses of the VO_2 film that we measured in this study and representative values for the Poisson's ratio (which is relatively unimportant in the analysis) and the fracture energy for a brittle ceramic: E_f = 224 GPa, σ_f = 1350 MPa, ν_f ~0.2, and Γ_f ~10 J/m^2. The value of the function g(α,β) was determined by interpolating the values reported by Beuth, which gives a value of 1.35, which through Equation (4) gives a value of Z = 2.1. Substituting these values into Equation (3) gives a critical film thickness of h_{cr} = 600 nm, which agrees with our experiments in that our 150 nm films did not fracture while our 1.63 µm films fractured.

Our analysis provides quantitative insight into averting fracture. First, Equation (3) shows that decreasing the film thickness is an effective technique to avert fracture, as it reduces the crack driving force.[12,13] Additionally, it is important to note that the critical thickness value will be strongly influenced by the residual stress σ_r from fabrication, which in our case was measured to be nearly four times that of the stress induced by the phase transformation itself. As such, fabrication techniques that induce less residual stress (particularly less tensile residual stress) are desirable in preventing fracture. Reducing residual stresses may be accomplished by implementing substrates that are conducive to smaller deposition-induced stress (e.g., lattice matched epitaxial films) and implementing substrates that have similar coefficients of thermal expansion to that of the VO_2 film, as to minimize thermal stresses that arise in cooling down from the high-temperature deposition. Likewise, deposition techniques that occur at lower temperatures and/or subsequent annealing to remove/reduce residual stresses are desirable.

Finally, we should note that in this study we did not explicitly study the effects of fatigue. We did determine that our relatively thin (150 nm) VO_2 films are resilient to several (50) cycles without any evidence of damage. However, in real computing devices, after many orders of magnitude more on/off cycles and the corresponding stresses that occur through the metal-insulator transition,VO_2 films may undergo damage from effects of fatigue, i.e., they may still eventually fracture even if thinner than the critical film thickness predicted from Equation (3). These effects warrant future studies.

Conclusions

In this work, we have performed detailed mechanical characterization of sputter-deposited polycrystalline VO_2 thin films. Significant stresses arise during thermal cycling of VO_2 thin films due to its metal-insulator phase transition. Despite VO_2 exhibiting overall volume expansion upon heating through this transition, our sputter-deposited films develop tension upon heating through the transition. We attribute this seemingly counterintuitive observation to the highly textured nature of our sputter-deposited films and the corresponding areal shrinkage of $(011)_M$ crystal plane through the transition. These observations highlight the importance of the fabricated crystal orientation on stresses that develop during operation. Next, combining our measurements of the elastic modulus E_f = 224 GPa and the stresses developed during the deposition and subsequent thermal cycling (which produces an overall tensile stress of 1350 MPa), we predicted a critical film thickness for our VO_2 films of 600 nm, below which we do not expect fracture. This prediction was corroborated by experiments and highlights the key ingredients to mitigate damage. Namely, decreasing film thickness, strategic crystal structure design of textured/epitaxial films, matching of coefficients of thermal expansion of the substrate to the film, performing deposition at lower temperatures, and annealing after deposition will all aid in producing VO_2 films that are robust during operation.

CHAPTER VI

CONCLUSIONS

This thesis has explored the chemo-mechanics of functional thin films in the application of lithium-ion batteries and neuromorphic computing devices. We focused on the intimate coupling between mechanics and other fields, such as chemical reactions, crystal structure variation from synthesis, and electron transport.

First, we presented the mechanical behavior of composite sulfur cathodes during cycling. We observed four major regions of stress generation associated with structural evolution: during discharging: 1) solid-phase conversion of sulfur into electrolyte-soluble polysulfides, followed by 2) deposition of an amorphous solid phase, which ultimately converts to Li_2S, and during charging: 3) dissolution of Li_2S, followed by 4) re-deposition of crystalline sulfur. Different from previously studied intercalative and conversion systems, we conclude that liquid-to-solid phase transformations (nucleation & growth) generate significant stresses during both charging and discharging. Additionally, the measurements indicated that significant hysteresis occurred during the first cycle, which may be attributed to plastic deformation associated with structural transformations. However, subsequent cycles showed nearly elastic and reversible mechanics. As a result, sulfur cathodes that withstand the first cycle while retaining active species, which can be engineered through precise mesoscale texturing, hold tremendous promise for structurally robust sulfur-based cathodes.

We then turned our attention to develop a novel technique for observing the morphological evolution in-operando during electrochemical cycling of polysulfide catholytes. We used this technique to monitor the morphological evolution during lithiation/delithiation of C-PVDF matrices soaked in a polysulfide catholyte. These studies clearly demonstrated that solid lithium sulfide deposits onto the host C-PVDF matrices by a thin film nucleation and growth type process during lithiation. Likewise, solid sulfur deposited through a similar process during delithiation. Moreover, this growth process depends on the charging rate, with larger charging rates leading to a more inhomogeneous distribution of the deposited solid species, and thus lower capacities. We further connected these effects to potential consequences in terms of mechanical stability by performing in-operando stress measurements during lithiation of C-PVDF matrices soaked in polysulfide catholytes at various charging rates. We found that slower charging rates produced higher capacities but larger stresses, thereby underscoring the importance of microstructural/geometric design of the host matrices to prevent mechanical damage. Overall, these studies provide connections between electrochemistry and the corresponding kinetics, mechanics, and morphological phenomena associated with soluble lithium polysulfides.

To investigate the intrinsic mechanical response of V_2O_5 during electrochemical cycling, we fabricated dense textured V_2O_5 thin film through magnetron sputtering. Using an in-situ multibeam optical sensor approach, we found that significant stresses arise during electrochemical cycling of V_2O_5 thin film cathodes. Extended cycling leads to accumulated mechanical damage (e.g., fracture, delamination) and structural changes (e.g., amorphization), which ultimately result in severe capacity fade. Despite the relatively small volume changes in cathodes during cycling, the observations provided herein highlight the intimate coupling between electrochemistry and mechanics in cathodes of lithium-ion batteries. Our results imply that mechanical and/or electrochemical processes can lead to their degradation, ultimately producing capacity fade. Specifically, in terms of electrochemistry, parasitic reactions during cycling (decomposition of electrolyte, deposition of CEI and SEI, etc.) may consume active materials or lead to irreversible structural changes (e.g., amorphization). In terms of mechanics, stresses generated during cycling may produce fracture or delamination, increasing resistivity and/or directly leading to loss of active materials. Likewise, stresses may accumulate during extended cycling, ultimately becoming large enough to induce chemo-mechanical damage in the system and correspondingly leading to significant capacity fade. Overall, beyond presenting fundamental behavior specific to V_2O_5 systems, we hope that this study will provide a general cautionary message to battery researchers in designing next-generation cathodes. In particular, in characterizing new materials, we believe that in addition to performing standard chemical and electrochemical analysis, it is equally as important to perform comprehensive mechanical evaluation, thereby ensuring that the battery is robust over extended cycling. Lastly, we turned our attention to materials for neuromorphic computing, and investigated the mechanical response of sputter-deposited VO_2 thin films during phase transformation from VO_2-M to VO_2-R during thermal cycling. We found that significant stresses arise during thermal cycle of VO_2 thin film due to its metal-insulator phase transition. Despite VO_2 exhibiting overall volume expansion upon heating through this transition, our textured VO_2-M thin films displayed relative tension upon heating through the transition due to texture of the deposited films and the corresponding areal shrinkage of $(011)_M$ crystal plane. Combing our measurements of the elastic modulus E_f = 224 GPa and the stresses accumulated during the deposition and subsequent thermal cycling (which produces a maximum tensile stress of σ_f = 1350 MPa), we predicted a critical film thickness of VO_2 of 600 nm, below which the VO_2 thin film will not fracture. This result was indeed corroborated through studies on VO_2 films with varying thickness. Overall, beyond presenting extensive mechanical characterization specific to VO_2 systems, we hope that this study will provide a general cautionary message to electronic device researchers in designing next-generation memory/computing devices. In particular, in characterizing new materials, we believe that in addition to performing standard chemical and electrical analysis, comprehensive mechanical evaluation should also be performed, thereby ensuring that the thin film device is robust over extended cycling.

REFERENCES

1. Mukhopadhyay, A. & Sheldon, B. W. Deformation and stress in electrode materials for Li-ion batteries. *Prog. Mater. Sci.* **63**, 58–116 (2014).

2. Thackeray, M. M. Lithiated Oxides for Lithium Ion Batteries. *J. Electrochem. Soc.* **142**, 2558–2563 (1995).

3. Needham, S. A., Wang, G. X., Liu, H. K., Drozd, V. A. & Liu, R. S. Synthesis and electrochemical performance of doped $LiCoO_2$ materials. *J. Power Sources* **174**, 828–831 (2007).

4. Reimers, J. N. & Dahn, J. R. Electrochemical and In Situ X-Ray Diffraction Studies of Lithium Intercalation in Li_xCoO_2. *J. Electrochem. Soc.* **139**, 2091–2097 (1992).

5. A.K.Padhi, K.S.Nanjundaswamy, and J. B. Goodenough. Phospho-olivines as Positive-Electrode Materials for Rechargeable Lithium Batteries. *J. Electrochem. Soc.* **144**, 1188 (1997).

6. Lin, H. *et al.* A GGA+U study of lithium diffusion in vanadium doped $LiFePO_4$. *Solid State Commun.* **152**, 999–1003 (2012).

7. De Jesus, L. R. *et al.* Striping modulations and strain gradients within individual particles of a cathode material upon lithiation. *Mater. Horizons* **5**, 486–498 (2018).

8. Muralidharan, N. *et al.* Tunable Mechanochemistry of Lithium Battery Electrodes. *ACS Nano* **11**, 6243–6251 (2017).

9. Xiao, X., Liu, P., Verbrugge, M. W., Haftbaradaran, H. & Gao, H. Improved

cycling stability of silicon thin film electrodes through patterning for high energy density lithium batteries. *J. Power Sources* **196**, 1409–1416 (2011).

10. Gabrisch, H., Wilcox, J. & Doeff, M. M. TEM Study of Fracturing in Spherical and Plate-like $LiFePO_4$ Particles. *Electrochem. Solid-State Lett.* **11**, A25 (2008).

11. Wang, D., Wu, X., Wang, Z. & Chen, L. Cracking causing cyclic instability of $LiFePO_4$ cathode material. *J. Power Sources* **140**, 125–128 (2005).

12. Pharr, M., Suo, Z. & Vlassak, J. J. Measurements of the fracture energy of lithiated silicon electrodes of Li-Ion batteries. *Nano Lett.* **13**, 5570–5577 (2013).

13. Hardin, G. R., Zhang, Y., Fincher, C. D. & Pharr, M. Interfacial Fracture of Nanowire Electrodes of Lithium-Ion Batteries. *Jom* **69**, 1519–1523 (2017).

14. Winter, M. & Besenhard, J. O. Electrochemical lithiation of tin and tin-based intermetallics and composites. *Electrochim. Acta* **45**, 31–50 (1999).

15. Zhao, K., Pharr, M., Vlassak, J. J. & Suo, Z. Fracture of electrodes in lithium-ion batteries caused by fast charging. *J. Appl. Phys.* **108**, 1–7 (2010).

16. Padhi, A.K., Nanjundaswamy, K.S., Masquelier, C., Okada, S. and Goodenough, J. . Effect of Structure on the Fe^{3+}/Fe^{2+} Redox Couplein Iron Phosphates. *J. Electrochem. Soc* **144**, 1609–1613 (1959).

17. Peng, H. J., Huang, J. Q., Cheng, X. B. & Zhang, Q. Review on High-Loading and High-Energy Lithium–Sulfur Batteries. *Adv. Energy Mater.* **7**, 1–54 (2017).

18. Manthiram, A., Fu, Y., Chung, S. H., Zu, C. & Su, Y. S. Rechargeable lithium-sulfur batteries. *Chem. Rev.* **114**, 11751–11787 (2014).

19. Ji, X. & Nazar, L. F. Advances in Li–S batteries. *J. Mater. Chem.* **20**, 9821

(2010).

20. Manthiram, A., Chung, S.-H. & Zu, C. Lithium-Sulfur Batteries: Progress and Prospects. *Adv. Mater.* **27**, 1980–2006 (2015).

21. Seh, Z. W., Sun, Y., Zhang, Q. & Cui, Y. Designing high-energy lithium–sulfur batteries. *Chem. Soc. Rev.* **45**, 5605–5634 (2016).

22. Song, M.-K., Cairns, E. J. & Zhang, Y. Lithium/sulfur batteries with high specific energy: old challenges and new opportunities. *Nanoscale* **5**, 2186 (2013).

23. Yin, Y. X., Xin, S., Guo, Y. G. & Wan, L. J. Lithium-sulfur batteries: Electrochemistry, materials, and prospects. *Angew. Chemie - Int. Ed.* **52**, 13186–13200 (2013).

24. Xin, S. *et al.* Smaller sulfur molecules promise better lithium’sulfur batteries. *J. Am. Chem. Soc.* **134**, 18510–18513 (2012).

25. Yuan, L., Yuan, H., Qiu, X., Chen, L. & Zhu, W. Improvement of cycle property of sulfur-coated multi-walled carbon nanotubes composite cathode for lithium/sulfur batteries. *J. Power Sources* **189**, 1141–1146 (2009).

26. Yue, Y. & Liang, H. 3D Current Collectors for Lithium-Ion Batteries : A Topical Review. **1800056**, 1–20 (2018).

27. Pu, X., Yang, G. & Yu, C. Liquid-type cathode enabled by 3D sponge-like carbon nanotubes for high energy density and long cycling life of Li-S Batteries. *Adv. Mater.* **26**, 7456–7461 (2014).

28. Zhao, K., Pharr, M., Hartle, L., Vlassak, J. J. & Suo, Z. Fracture and debonding in lithium-ion batteries with electrodes of hollow core-shell nanostructures. *J. Power*

Sources **218**, 6–14 (2012).

29. McDowell, M. T. *et al.* Studying the kinetics of crystalline silicon nanoparticle lithiation with in situ transmission electron microscopy. *Adv. Mater.* **24**, 6034–6041 (2012).

30. Zhao, K. *et al.* Concurrent Reaction and Plasticity during Initial Lithiation of Crystalline Silicon in Lithium-Ion Batteries. *J. Electrochem. Soc.* **159**, A238–A243 (2012).

31. Ryu, I., Choi, J. W., Cui, Y. & Nix, W. D. Size-dependent fracture of Si nanowire battery anodes. *J. Mech. Phys. Solids* **59**, 1717–1730 (2011).

32. Liu, X. H. *et al.* Size-dependent fracture of silicon nanoparticles during lithiation. *ACS Nano* **6**, 1522–1531 (2012).

33. Boles, S. T., Thompson, C. V., Kraft, O. & Mönig, R. In situ tensile and creep testing of lithiated silicon nanowires. *Appl. Phys. Lett.* **103**, 1–5 (2013).

34. Wang, X., Yang, A. & Xia, S. Fracture Toughness Characterization of Lithiated Germanium as an Anode Material for Lithium-Ion Batteries. *J. Electrochem. Soc.* **163**, A90–A95 (2016).

35. Pharr, M., Choi, Y. S., Lee, D., Oh, K. H. & Vlassak, J. J. Measurements of stress and fracture in germanium electrodes of lithium-ion batteries during electrochemical lithiation and delithiation. *J. Power Sources* **304**, 164–169 (2016).

36. Al-Obeidi, A., Kramer, D., Thompson, C. V. & Mönig, R. Mechanical stresses and morphology evolution in germanium thin film electrodes during lithiation and

delithiation. *J. Power Sources* **297**, 472–480 (2015).

37. Sethuraman, V. A., Van Winkle, N., Abraham, D. P., Bower, A. F. & Guduru, P. R. Real-time stress measurements in lithium-ion battery negative-electrodes. *J. Power Sources* **206**, 334–342 (2012).

38. Mukhopadhyay, A., Tokranov, A., Xiao, X. & Sheldon, B. W. Stress development due to surface processes in graphite electrodes for Li-ion batteries: A first report. *Electrochim. Acta* **66**, 28–37 (2012).

39. Sheth, J. *et al.* In Situ Stress Evolution in Li_{1+x} Mn_2O_4 Thin Films during Electrochemical Cycling in Li-Ion Cells. *J. Electrochem. Soc.* **163**, A2524–A2530 (2016).

40. Woodford, W. H., Chiang, Y.-M. & Carter, W. C. "Electrochemical Shock" of Intercalation Electrodes: A Fracture Mechanics Analysis. *J. Electrochem. Soc.* **157**, A1052 (2010).

41. Luo, Y. *et al.* Roadblocks in Cation Diffusion Pathways: Implications of Phase Boundaries for Li-ion Diffusivity in an Intercalation Cathode Material. *ACS Appl. Mater. Interfaces* acsami.8b10604 (2018).

42. G. A. Horrocks, M. F. Likely, J. M. Velazquez and S. Banerjee. Finite size effects on the structural progression induced by lithiation of V_2O_5 : a combined diffraction and Raman spectroscopy study. *J. Mater. Chem. A* **1**, 15265–15277 (2013).

43. Luo, Y. *et al.* Roadblocks in Cation Diffusion Pathways : Implications of Phase Boundaries for Li-Ion Diffusivity in an Intercalation Cathode Material. *ACS Appl.*

Mater. Interfaces **10**, 30901–30911 (2018).

44. De Jesus, L. R., Andrews, J. L., Parija, A. & Banerjee, S. Defining Diffusion Pathways in Intercalation Cathode Materials: Some Lessons from V_2O_5 on Directing Cation Traffic. *ACS Energy Lett.* **3**, 915–931 (2018).

45. Jung, H., Gerasopoulos, K., Talin, A. A. & Ghodssi, R. A platform for in situ Raman and stress characterizations of V_2O_5 cathode using MEMS device. *Electrochim. Acta* **242**, 227–239 (2017).

46. Scarminio, J., Talledo, A., Andersson, A. A., Passerini, S. & Decker, F. Stress and electrochromism induced by Li insertion in crystalline and amorphous V_2O_5 thin film electrodes. *Electrochim. Acta* **38**, 1637–1642 (1993).

47. Yue, Y. & Liang, H. Micro- and Nano-Structured Vanadium Pentoxide (V_2O_5) for Electrodes of Lithium-Ion Batteries. *Adv. Energy Mater.* **7**, 1–32 (2017).

48. Andrews, J. L. *et al.* Reversible Mg-Ion Insertion in a Metastable One-Dimensional Polymorph of V_2O_5. *Chem* **4**, 564–585 (2018).

49. Gu, S. *et al.* Confirming reversible Al3+ storage mechanism through intercalation of Al^{3+} into V_2O_5 nanowires in a rechargeable aluminum battery. *Energy Storage Mater.* **6**, 9–17 (2017).

50. Kundu, D., Adams, B. D., Duffort, V., Vajargah, S. H. & Nazar, L. F. A high-capacity and long-life aqueous rechargeable zinc battery using a metal oxide intercalation cathode. *Nat. Energy* **1**, 1–8 (2016).

51. Parija, A. *et al.* Topochemically De-Intercalated Phases of V_2O_5 as Cathode Materials for Multivalent Intercalation Batteries: A First-Principles Evaluation.

Chem. Mater. **28**, 5611–5620 (2016).

52. Clites, M. & Pomerantseva, E. Bilayered vanadium oxides by chemical pre-intercalation of alkali and alkali-earth ions as battery electrodes. *Energy Storage Mater.* **11**, 30–37 (2018).

53. Clites, M., Byles, B. W. & Pomerantseva, E. Effect of aging and hydrothermal treatment on electrochemical performance of chemically pre-intercalated Na-V-O nanowires for Na-ion batteries. *J. Mater. Chem. A* **4**, 7754–7761 (2016).

54. He, P. *et al.* High-Performance Aqueous Zinc-Ion Battery Based on Layered $H_2V_3O_8$ Nanowire Cathode. *Small* **13**, 1702551 (2017).

55. Yan, M. *et al.* Water-Lubricated Intercalation in $V_2O_5 \cdot nH_2O$ for High-Capacity and High-Rate Aqueous Rechargeable Zinc Batteries. *Adv. Mater.* **30**, 1–6 (2018).

56. Yang, Y. *et al.* Li^+ intercalated V_2O_5 nH_2O with enlarged layer spacing and fast ion diffusion as an aqueous zinc-ion battery cathode. *Energy Environ. Sci.* **11**, 3157–3162 (2018).

57. Jian, J. *et al.* Continuous Tuning of Phase Transition Temperature in VO_2 Thin Films on c-Cut Sapphire Substrates via Strain Variation. *ACS Appl. Mater. Interfaces* **9**, 5319–5327 (2017).

58. Clarke, H. *et al.* Nucleation-controlled hysteresis in unstrained hydrothermal VO_2 particles. *Phys. Rev. Mater.* **2**, 1–8 (2018).

59. Andrews, J. L., Santos, D. A., Meyyappan, M., Williams, R. S. & Banerjee, S. Building Brain-Inspired Logic Circuits from Dynamically Switchable Transition-Metal Oxides. *Trends Chem.* **1**, 711–726 (2019).

60. Park, J. H. *et al.* Measurement of a solid-state triple point at the metal-insulator transition in VO_2. *Nature* **500**, 431–434 (2013).

61. Cao, J. *et al.* Extended mapping and exploration of the vanadium dioxide stress-temperature phase diagram. *Nano Lett.* **10**, 2667–2673 (2010).

62. Yi, W. *et al.* Biological plausibility and stochasticity in scalable VO_2 active memristor neurons. *Nat. Commun.* **9**, (2018).

63. Jian, J. *et al.* Broad Range Tuning of Phase Transition Property in VO_2 Through Metal-Ceramic Nanocomposite Design. *Adv. Funct. Mater.* **1903690**, 1–12 (2019).

64. Sellers, D. G. *et al.* Atomic Hourglass and Thermometer Based on Diffusion of a Mobile Dopant in VO_2. *J. Am. Chem. Soc.* **142**, 15513–15526 (2020).

65. Braham, E. J. *et al.* Modulating the Hysteresis of an Electronic Transition: Launching Alternative Transformation Pathways in the Metal-Insulator Transition of Vanadium(IV) Oxide. *Chem. Mater.* **30**, 214–224 (2018).

66. Alivio, T. E. G. *et al.* Postsynthetic Route for Modifying the Metal-Insulator Transition of VO_2 by Interstitial Dopant Incorporation. *Chem. Mater.* **29**, 5401–5412 (2017).

67. Yajima, T., Ninomiya, Y., Nishimura, T. & Toriumi, A. Drastic change in electronic domain structures via strong elastic coupling in VO_2 films. *Phys. Rev. B - Condens. Matter Mater. Phys.* **91**, 1–6 (2015).

68. Kawatani, K., Kanki, T. & Tanaka, H. Formation mechanism of a microscale domain and effect on transport properties in strained VO_2 thin films on TiO_2

(001). *Phys. Rev. B - Condens. Matter Mater. Phys.* **90**, 1–5 (2014).

69. Abreu, E. *et al.* THz spectroscopy of VO_2 epitaxial films: Controlling the anisotropic properties through strain engineering. *New J. Phys.* **14**, (2012).

70. Liu, M. *et al.* Phase transition in bulk single crystals and thin films of VO_2 by nanoscale infrared spectroscopy and imaging. *Phys. Rev. B - Condens. Matter Mater. Phys.* **91**, (2015).

71. Rodríguez, L. *et al.* Self-Pixelation Through Fracture in VO_2 Thin Films . *ACS Appl. Electron. Mater.* **2**, 1433–1439 (2020).

72. Nagashima, K., Yanagida, T., Tanaka, H. & Kawai, T. Stress relaxation effect on transport properties of strained vanadium dioxide epitaxial thin films. *Phys. Rev. B - Condens. Matter Mater. Phys.* **74**, 13–16 (2006).

73. Paik, H. *et al.* Transport properties of ultra-thin VO_2 films on (001) TiO_2 grown by reactive molecular-beam epitaxy. *Appl. Phys. Lett.* **107**, 1–6 (2015).

74. Cuisinier, M. *et al.* Sulfur speciation in Li-S batteries determined by operando X-ray absorption spectroscopy. *J. Phys. Chem. Lett.* **4**, 3227–3232 (2013).

75. Wang, Q. *et al.* Direct Observation of Sulfur Radicals as Reaction Media in Lithium Sulfur Batteries. *J. Electrochem. Soc.* **162**, A474–A478 (2015).

76. Xiao, J. *et al.* Following the transient reactions in lithium-sulfur batteries using an in situ nuclear magnetic resonance technique. *Nano Lett.* **15**, 3309–3316 (2015).

77. Hagen, M. *et al.* In-Situ Raman Investigation of Polysulfide Formation in Li-S Cells. *J. Electrochem. Soc.* **160**, A1205–A1214 (2013).

78. Yeon, J.-T. *et al.* Raman Spectroscopic and X-ray Diffraction Studies of Sulfur

Composite Electrodes during Discharge and Charge. *J. Electrochem. Soc.* **159**, A1308–A1314 (2012).

79. Wu, H. L., Huff, L. A. & Gewirth, A. A. In situ raman spectroscopy of sulfur speciation in lithium-sulfur batteries. *ACS Appl. Mater. Interfaces* **7**, 1709–1719 (2015).

80. Patel, M. U. M. *et al.* Li-S battery analyzed by UV/vis in operando mode. *ChemSusChem* **6**, 1177–1181 (2013).

81. Zou, Q. & Lu, Y. C. Solvent-Dictated Lithium Sulfur Redox Reactions: An Operando UV-vis Spectroscopic Study. *J. Phys. Chem. Lett.* **7**, 1518–1525 (2016).

82. Conder, J. *et al.* Direct observation of lithium polysulfides in lithium-sulfur batteries using operando X-ray diffraction. *Nat. Energy* **2**, 1–7 (2017).

83. Waluś, S. *et al.* New insight into the working mechanism of lithium–sulfur batteries: in situ and operando X-ray diffraction characterization. *Chem. Commun.* **49**, 7899 (2013).

84. Nelson, J. *et al.* In operando X-ray diffraction and transmission X-ray microscopy of lithium sulfur batteries. *J. Am. Chem. Soc.* **134**, 6337–6343 (2012).

85. Zhu, W. *et al.* Investigation of the reaction mechanism of lithium sulfur batteries in different electrolyte systems by in situ Raman spectroscopy and in situ X-ray diffraction. *Sustain. Energy Fuels* **1**, 737–747 (2017).

86. Yu, X. *et al.* Direct Observation of the Redistribution of Sulfur and Polysufides in Li-S Batteries during the First Cycle by in Situ X-Ray Fluorescence Microscopy. *Adv. Energy Mater.* **5**, 1–6 (2015).

87. Kamphaus, E. P. & Balbuena, P. B. First-principles investigation of lithium polysulfide structure and behavior in solution. *J. Phys. Chem. C* **121**, 21105–21117 (2017).

88. Wang, H. *et al.* Graphene-wrapped sulfur particles as a rechargeable lithium-sulfur battery cathode material with high capacity and cycling stability. *Nano Lett.* **11**, 2644–2647 (2011).

89. Ji, X., Lee, K. T. & Nazar, L. F. A highly ordered nanostructured carbon-sulphur cathode for lithium-sulphur batteries. *Nat. Mater.* **8**, 500–506 (2009).

90. Mikhaylik, Y. V. & Akridge, J. R. Polysulfide Shuttle Study in the Li/S Battery System. *J. Electrochem. Soc.* **151**, A1969 (2004).

91. Zheng, G., Yang, Y., Cha, J. J., Hong, S. S. & Cui, Y. Hollow carbon nanofiber-encapsulated sulfur cathodes for high specific capacity rechargeable lithium batteries. *Nano Lett.* **11**, 4462–4467 (2011).

92. Wu, D. S. *et al.* Quantitative investigation of polysulfide adsorption capability of candidate materials for Li-S batteries. *Energy Storage Mater.* **13**, 241–246 (2018).

93. Yang, Y., Zheng, G. & Cui, Y. Nanostructured sulfur cathodes. *Chem. Soc. Rev.* **42**, 3018 (2013).

94. He, G., Ji, X. & Nazar, L. High “C” rate Li-S cathodes: sulfur imbibed bimodal porous carbons. *Energy Environ. Sci.* **4**, 2878 (2011).

95. Liu, Z., Balbuena, P. B. & Mukherjee, P. P. Revealing Charge Transport Mechanisms in Li_2S_2 for Li–Sulfur Batteries. *J. Phys. Chem. Lett.* **8**, 1324–1330 (2017).

96. Schuster, J. *et al.* Spherical Ordered Mesoporous Carbon Nanoparticles with High Porosity for Lithium-Sulfur Batteries. *Angew. Chemie* **124**, 3651–3655 (2012).

97. Stoney, G. G. The Tension of Metallic Films Deposited by Electrolysis. *Proc. R. Soc. A Math. Phys. Eng. Sci.* **82**, 172–175 (1909).

98. Nix, W. D. Mechanical properties of thin films. *Metall. Trans. A* **20**, 2217–2245 (1989).

99. Kumar, R., Woo, J. H., Xiao, X. & Sheldon, B. W. Internal Microstructural Changes and Stress Evolution in Silicon Nanoparticle Based Composite Electrodes. *J. Electrochem. Soc.* **164**, A3750–A3765 (2017).

100. Nadimpalli, S. P. V., Sethuraman, V. A., Abraham, D. P., Bower, A. F. & Guduru, P. R. Stress Evolution in Lithium-Ion Composite Electrodes during Electrochemical Cycling and Resulting Internal Pressures on the Cell Casing. *J. Electrochem. Soc.* **162**, A2656–A2663 (2015).

101. Sethuraman, V. A. *et al.* Stress Evolution in Composite Silicon Electrodes during Lithiation/Delithiation. *J. Electrochem. Soc.* **160**, A739–A746 (2013).

102. Qi, Z. *et al.* $LiNi_{0.5}Mn_{0.3}Co_{0.2}O_2$/Au nanocomposite thin film cathode with enhanced electrochemical properties. *Nano Energy* **46**, 290–296 (2018).

103. Waluš, S. *et al.* Lithium/Sulfur Batteries Upon Cycling: Structural Modifications and Species Quantification by in Situ and Operando X-Ray Diffraction Spectroscopy. *Adv. Energy Mater.* **5**, 1–5 (2015).

104. Wang, Y. *et al.* Structural change of the porous sulfur cathode using gelatin as a binder during discharge and charge. *Electrochim. Acta* **54**, 4062–4066 (2009).

105. Xiong, S., Xie, K., Diao, Y. & Hong, X. Oxidation process of polysulfides in charge process for lithium-sulfur batteries. *Ionics (Kiel).* **18**, 867–872 (2012).

106. Pharr, M., Suo, Z. & Vlassak, J. J. Variation of stress with charging rate due to strain-rate sensitivity of silicon electrodes of Li-ion batteries. *J. Power Sources* **270**, 569–575 (2014).

107. Sethuraman, V. A., Chon, M. J., Shimshak, M., Srinivasan, V. & Guduru, P. R. In situ measurements of stress evolution in silicon thin films during electrochemical lithiation and delithiation. *J. Power Sources* **195**, 5062–5066 (2010).

108. Cammarata, R. C. & Trimble, T. M. Surface stress model for intrinsic stresses in thin films. *J. Mater. sResearch* **15**, 2468–2474 (2000).

109. Del Vecchio, A. L. & Spaepen, F. The effect of deposition rate on the intrinsic stress in copper and silver thin films. *J. Appl. Phys.* **101**, (2007).

110. Windischmann, H. Intrinsic stress in sputtered thin films. *J. Vac. Sci. Technol. A Vacuum, Surfaces, Film.* **9**, 2431–2436 (1991).

111. Freund, L. & Suresh, S. Thin Film Materials: Stress, Defect Formation and Surface Evolution. 768 (2003). doi:10.1017/CBO9780511754715

112. Feng, Z. *et al.* Unravelling the role of Li_2S_2 in lithium-sulfur batteries: A first principles study of its energetic and electronic properties. *J. Power Sources* **272**, 518–521 (2014).

113. Wang, M., Yu, J. & Lin, S. Lithiation-Assisted Strengthening Effect and Reactive Flow in Bulk and Nanoconfined Sulfur Cathodes of Lithium-Sulfur Batteries. *J. Phys. Chem. C* **121**, 17029–17037 (2017).

114. Parija, A., Waetzig, G. R., Andrews, J. L. & Banerjee, S. Traversing Energy Landscapes Away from Equilibrium: Strategies for Accessing and Utilizing Metastable Phase Space. *J. Phys. Chem. C* (2018).

115. Liu, H. *et al.* High Energy Density $LiFePO_4$/C Cathode Material Synthesized by Wet Ball Milling Combined with Spray Drying Method. *J. Electrochem. Soc.* **164**, A3666–A3672 (2017).

116. Liu, Z., Mistry, A. & Mukherjee, P. P. Mesoscale Physicochemical Interactions in Lithium–Sulfur Batteries: Progress and Perspective. *J. Electrochem. Energy Convers. Storage* **15**, 010802 (2017).

117. Waluś, S. *et al.* Volumetric expansion of Lithium-Sulfur cell during operation – Fundamental insight into applicable characteristics. *Energy Storage Mater.* **10**, 233–245 (2018).

118. Zhang, S. S. Liquid electrolyte lithium/sulfur battery: Fundamental chemistry, problems, and solutions. *J. Power Sources* **231**, 153–162 (2013).

119. Pu, X., Yang, G. & Yu, C. Trapping Polysulfides Catholyte in Carbon Nanofiber Sponges for Improving the Performances of Sulfur Batteries. *J. Electrochem. Soc.* **162**, A1396–A1400 (2015).

120. Cui, Y. & Fu, Y. Enhanced cyclability of Li/polysulfide batteries by a polymer-modified carbon paper current collector. *ACS Appl. Mater. Interfaces* **7**, 20369–20376 (2015).

121. Qie, L., Zu, C. & Manthiram, A. A High Energy Lithium-Sulfur Battery with Ultrahigh-Loading Lithium Polysulfide Cathode and its Failure Mechanism. *Adv.*

Energy Mater. **6**, 1–7 (2016).

122. Sun, Y. *et al.* In-operando optical imaging of temporal and spatial distribution of polysulfides in lithium-sulfur batteries. *Nano Energy* **11**, 579–586 (2015).

123. Chung, S. H., Han, P., Singhal, R., Kalra, V. & Manthiram, A. Electrochemically Stable Rechargeable Lithium-Sulfur Batteries with a Microporous Carbon Nanofiber Filter for Polysulfide. *Adv. Energy Mater.* **5**, 1–12 (2015).

124. Zu, C. & Manthiram, A. High-performance Li/dissolved polysulfi de batteries with an advanced cathode structure and high sulfur content. *Adv. Energy Mater.* **4**, 2–7 (2014).

125. Zu, C., Fu, Y. & Manthiram, A. Highly reversible Li/dissolved polysulfide batteries with binder-free carbon nanofiber electrodes. *J. Mater. Chem. A* **1**, 10362–10367 (2013).

126. Zhou, G., Zhao, Y., Zu, C. & Manthiram, A. Free-standing TiO_2 nanowire-embedded graphene hybrid membrane for advanced Li/dissolved polysulfide batteries. *Nano Energy* **12**, 240–249 (2015).

127. Cui, Y. & Fu, Y. Polysulfide transport through separators measured by a linear voltage sweep method. *J. Power Sources* **286**, 557–560 (2015).

128. Zhou, G., Zhao, Y., Zu, C. & Manthiram, A. Free-standing TiO_2 nanowire-embedded graphene hybrid membrane for advanced Li/dissolved polysulfide batteries. *Nano Energy* **12**, 240–249 (2015).

129. Fu, Y., Su, Y. S. & Manthiram, A. Highly reversible lithium/dissolved polysulfide batteries with carbon nanotube electrodes. *Angew. Chemie - Int. Ed.* **52**, 6930–

6935 (2013).

130. Zhou, G., Paek, E., Hwang, G. S. & Manthiram, A. Long-life Li/polysulphide batteries with high sulphur loading enabled by lightweight three-dimensional nitrogen/sulphur-codoped graphene sponge. *Nat. Commun.* **6**, 1–11 (2015).

131. Zu, C., Fu, Y. & Manthiram, A. Highly reversible Li/dissolved polysulfide batteries with binder-free carbon nanofiber electrodes. *J. Mater. Chem. A* **1**, 10362–10367 (2013).

132. Zhang, Y. *et al.* In-situ measurements of stress evolution in composite sulfur cathodes. *Energy Storage Mater.* **16**, 491–497 (2018).

133. Ye, H., Yin, Y. X. & Guo, Y. G. Insight into the loading temperature of sulfur on sulfur/carbon cathode in lithium-sulfur batteries. *Electrochim. Acta* **185**, 62–68 (2015).

134. Busche, M. R. *et al.* Systematical electrochemical study on the parasitic shuttle-effect in lithium-sulfur-cells at different temperatures and different rates. *J. Power Sources* **259**, 289–299 (2014).

135. Park, J. W. *et al.* Solvent effect of room temperature ionic liquids on electrochemical reactions in lithium-sulfur batteries. *J. Phys. Chem. C* **117**, 4431–4440 (2013).

136. Yuan, L., Qiu, X., Chen, L. & Zhu, W. New insight into the discharge process of sulfur cathode by electrochemical impedance spectroscopy. *J. Power Sources* **189**, 127–132 (2009).

137. Tang, W. *et al.* In Situ Observation and Electrochemical Study of Encapsulated

Sulfur Nanoparticles by MoS2Flakes. *J. Am. Chem. Soc.* **139**, 10133–10141 (2017).

138. Kim, H. *et al.* In Situ TEM Observation of Electrochemical Lithiation of Sulfur Confined within Inner Cylindrical Pores of Carbon Nanotubes. *Adv. Energy Mater.* **5**, 1–7 (2015).

139. Yuan, Z. *et al.* Powering Lithium-Sulfur Battery Performance by Propelling Polysulfide Redox at Sulfiphilic Hosts. *Nano Lett.* **16**, 519–527 (2016).

140. Huang, J. Q. *et al.* Ionic shield for polysulfides towards highly-stable lithium-sulfur batteries. *Energy Environ. Sci.* **7**, 347–353 (2014).

141. Bai, S., Liu, X., Zhu, K., Wu, S. & Zhou, H. Metal-organic framework-based separator for lithium-sulfur batteries. *Nat. Energy* **1**, (2016).

142. Yao, H. *et al.* Improved lithium-sulfur batteries with a conductive coating on the separator to prevent the accumulation of inactive S-related species at the cathode-separator interface. *Energy Environ. Sci.* **7**, 3381–3390 (2014).

143. Zhang, Y. *et al.* In-situ measurements of stress evolution in composite sulfur cathodes. *Energy Storage Mater.* **16**, 491–497 (2018).

144. Zhang, Y., Fincher, C., McProuty, S. & Pharr, M. In-operando imaging of polysulfide catholytes for Li–S batteries and implications for kinetics and mechanical stability. *J. Power Sources* **434**, 226727 (2019).

145. Baddour-hadjean, R. Raman Microspectrometry Applied to the Study of Electrode Materials for Lithium Batteries. 1278–1319 (2010).

146. Marzouk, A. Structural modifications of $Li_xV_2O_5$ in a composite cathode ($0 \leq x <$

2) investigated by Raman microspectrometry. doi:10.1002/jrs.2984

147. Ramana, C. V., Smith, R. J., Hussain, O. M., Massot, M. & Julien, C. M. Surface analysis of pulsed laser-deposited V_2O_5 thin films and their lithium intercalated products studied by Raman spectroscopy. *Surf. Interface Anal.* **37**, 406–411 (2005).

148. Baddour-Hadjean, R., Raekelboom, E. & Pereira-Ramos, J. P. New structural characterization of the $Li_xV_2O_5$ system provided by Raman spectroscopy. *Chem. Mater.* **18**, 3548–3556 (2006).

149. Haftbaradaran, H., Xiao, X. & Gao, H. Critical film thickness for fracture in thin-film electrodes on substrates in the presence of interfacial sliding. *Model. Simul. Mater. Sci. Eng.* **21**, (2013).

150. Chon, M. J., Sethuraman, V. A., McCormick, A., Srinivasan, V. & Guduru, P. R. Real-time measurement of stress and damage evolution during initial lithiation of crystalline silicon. *Phys. Rev. Lett.* **107**, 1–4 (2011).

151. Laforge, B., Levan-Jodin, L., Salot, R. & Billard, A. Study of Germanium as Electrode in Thin-Film Battery. *J. Electrochem. Soc.* **155**, A181 (2007).

152. Dahn, J. R., Burns, J. C. & Stevens, D. A. Importance of Coulombic Efficiency Measurements in R&D Efforts to Obtain Long-Lived Li-Ion Batteries. *Interface Mag.* **25**, 75–78 (2016).

153. Smith, A. J., Burns, J. C., Trussler, S. & Dahn, J. R. Precision Measurements of the Coulombic Efficiency of Lithium-Ion Batteries and of Electrode Materials for Lithium-Ion Batteries. *J. Electrochem. Soc.* **157**, A196 (2009).

154. Yang, F., Wang, D., Zhao, Y., Tsui, K. L. & Bae, S. J. A study of the relationship between coulombic efficiency and capacity degradation of commercial lithium-ion batteries. *Energy* **145**, 486–495 (2018).

155. Qi, Z. *et al.* Li_2MnO_3 Thin Films with Tilted Domain Structure as Cathode for Li-Ion Batteries. *ACS Appl. Energy Mater.* acsaem.9b00259 (2019). doi:10.1021/acsaem.9b00259

156. Smith, A. J. & Dahn, J. R. Delta Differential Capacity Analysis. *J. Electrochem. Soc.* **159**, A290–A293 (2012).

157. Jehnichen, P., Wedlich, K. & Korte, C. Degradation of high-voltage cathodes for advanced lithium-ion batteries–differential capacity study on differently balanced cells. *Sci. Technol. Adv. Mater.* **20**, 1–9 (2019).

158. Dubarry, M., Svoboda, V., Hwu, R. & Yann Liaw, B. Incremental Capacity Analysis and Close-to-Equilibrium OCV Measurements to Quantify Capacity Fade in Commercial Rechargeable Lithium Batteries. *Electrochem. Solid-State Lett.* **9**, A454 (2006).

159. Song, J. Y., Lee, H. H., Wang, Y. Y. & Wan, C. C. Two- and three-electrode impedance spectroscopy of lithium-ion batteries. *J. Power Sources* **111**, 255–267 (2002).

160. Nadimpalli, S. P. V., Tripuraneni, R. & Sethuraman, V. A. Real-Time Stress Measurements in Germanium Thin Film Electrodes during Electrochemical Lithiation/Delithiation Cycling. *J. Electrochem. Soc.* **162**, A2840–A2846 (2015).

161. Zhao, K., Pharr, M., Cai, S., Vlassak, J. J. & Suo, Z. Large plastic deformation in

high-capacity lithium-ion batteries caused by charge and discharge. *J. Am. Ceram. Soc.* **94**, 226–235 (2011).

162. Nagashima, K., Yanagida, T., Tanaka, H. & Kawai, T. Stress relaxation effect on transport properties of strained vanadium dioxide epitaxial thin films. *Phys. Rev. B - Condens. Matter Mater. Phys.* **74**, 13–16 (2006).

163. Jin, P. *et al.* Characterization of mechanical properties of VO_2 thin films on sapphire and silicon by ultra-microindentation. *Thin Solid Films* **343**–**344**, 134–137 (1999).

164. Guo, H. *et al.* Mechanics and dynamics of the strain-induced M_1-M_2 structural phase transition in individual VO_2 nanowires. *Nano Lett.* **11**, 3207–3213 (2011).

165. Singh, D. & Viswanath, B. In situ nanomechanical behaviour of coexisting insulating and metallic domains in VO_2 microbeams. *J. Mater. Sci.* **52**, 5589–5599 (2017).

166. Hay, J. & Crawford, B. Measuring substrate-independent modulus of thin films. *J. Mater. Res.* **26**, 727–738 (2011).

167. Zhang, Y., Luo, Y., Fincher, C., Banerjee, S. & Pharr, M. Chemo-mechanical degradation in V_2O_5 thin film cathodes of Li-ion batteries during electrochemical cycling. *J. Mater. Chem. A* **7**, 23922–23930 (2019).

168. Ma, B., Liu, S., Tong, S., Narayanan, M. & Balachandran, U. Enhanced dielectric properties of $Pb_{0.92}La_{0.08}\,Zr_{0.52}Ti_{0.48}O_3$ films with compressive stress. *J. Appl. Phys.* **112**, 0–9 (2012).

169. Prevéy, P. S. X-Ray Diffraction Residual Stress Techniques. *Lambda Technol.*

(2018).

170. John M. Longo, P. K. A Refinement of the Structure of VO_2. *Acta Chem. Scand.* **24**, 420–426 (1970).

171. Oliver, W. C. & Pharr, G. M. An improved technique for determining hardness and elastic modulus using load and displacement sensing indentation experiments. *J. Mater. Res.* **7**, (1992).

172. Jones, A. C., Berweger, S., Wei, J., Cobden, D. & Raschke, M. B. Nano-optical investigations of the metal-insulator phase behavior of individual VO_2 microcrystals. *Nano Lett.* **10**, 1574–1581 (2010).

173. Zhang, S., Chou, J. Y. & Lauhon, L. J. Direct correlation of structural domain formation with the metal insulator transition in a VO_2 nanobeam. *Nano Lett.* **9**, 4527–4532 (2009).

174. Kim, H. T. *et al.* Raman study of electric-field-induced first-order metal-insulator transition in VO_2 -based devices. *Appl. Phys. Lett.* **86**, 1–3 (2005).

175. Chen, X. & Vlassak, J. J. Numerical study on the measurement of thin film mechanical properties by means of nanoindentation. *J. Mater. Res.* **16**, 2974–2982 (2001).

176. TABOR, D. The hardness of solids. *Surf. Physics, Cavendish Lab. Cambridge*

177. Kawakubo, T. & Nakagawa, T. Phase Transition in VO_2. *J. Phys. Soc. Japan* **19**, 517–519 (1964).

178. Watanabe, H., Yamada, N. & Okaji, M. Linear thermal expansion coefficient of silicon from 293 to 1000 K. *Int. J. Thermophys.* **25**, 221–236 (2004).

179. McWhan, D. B., Marezio, M., Remeika, J. P. & Dernier, P. D. X-ray diffraction study of metallic VO_2. *Phys. Rev. B* **10**, 490–495 (1974).

180. Kucharczyk, D. & Niklewski, T. Accurate X-ray Determination of the Lattice Parameters and the Thermal Expansion Coefficients of VO_2 near the Transition Temperature Institute for Low Temperature and Structure Research , Polish Academy of Sciences , 50-950 Wroctaw , Poland. *J. Appl. Cryst.* **12**, 370–373 (1979).

181. Huang, C., Zhang, Z., Ramanathan, S. & Weinstein, D. VO_2 Phase-Transition-Based Vertical. **66**, 4380–4386 (2019).

182. Balakrishnan, V., Ko, C. & Ramanathan, S. In situ studies on twinning and cracking proximal to insulator-metal transition in self-supported VO_2/Si_3N_4 membranes. *J. Mater. Res.* **27**, 1476–1481 (2012).

183. Rajeswaran, B., Viannie, L. R., Rajanna, K., Jayanth, G. R. & Umarji, A. M. Phase transition induced micromechanical actuation in VO_2 coated cantilever. *J. Appl. Phys.* **124**, (2018).

184. Lin, T., Wang, L., Wang, X., Zhang, Y. & Yu, Y. Influence of lattice distortion on phase transition properties of polycrystalline VO_2 thin film. *Appl. Surf. Sci.* **379**, 179–185 (2016).

185. Yang, Y. *et al.* Transmittance change with thickness for polycrystalline VO_2 films deposited at room temperature. *J. Alloys Compd.* **791**, 648–654 (2019).

186. Zhang, K. *et al.* Synthesis of VO_2 Thin Films by Atomic Layer Deposition with TEMAV as Precursor. *ECS Trans.* **50**, 175–182 (2013).

187. Guiton, B. S., Gu, Q., Prieto, A. L., Gudiksen, M. S. & Park, H. Single-crystalline vanadium dioxide nanowires with rectangular cross sections. *J. Am. Chem. Soc.* **127**, 498–499 (2005).

188. Haras, A., Witko, M., Salahub, D. R., Hermann, K. & Tokarz, R. Electronic properties of the VO_2 (011) surface: Density functional cluster calculations. *Surf. Sci.* **491**, 77–87 (2001).

189. Sohn, J. I. *et al.* Direct observation of the structural component of the metal-insulator phase transition and growth habits of epitaxially grown VO_2 nanowires. *Nano Lett.* **7**, 1570–1574 (2007).

190. Beuth, J. L. Cracking of thin bonded films in residual tension. *Int. J. Solids Struct.* **29**, 1657–1675 (1992).

APPENDIX A

SUPPORTING INFORMATION FOR CHAPTER IV

Phase	Space group	Unit cell parameter (Å)			Volume (Å^3)
		a	b	c	
α-V_2O_5	Pmmn	11.5440	3.5710	4.3830	180.6831
ε-V_2O_5	Pmmn	11.3552	3.5732	4.6548	188.8657
δ-V_2O_5	Amam	11.2423	4.9527	3.6018	200.5473
Υ-V_2O_5	Pnma	9.7020	3.6070	5.3320	186.5939

Table S1 Dimensional parameters of different phases during lithiation

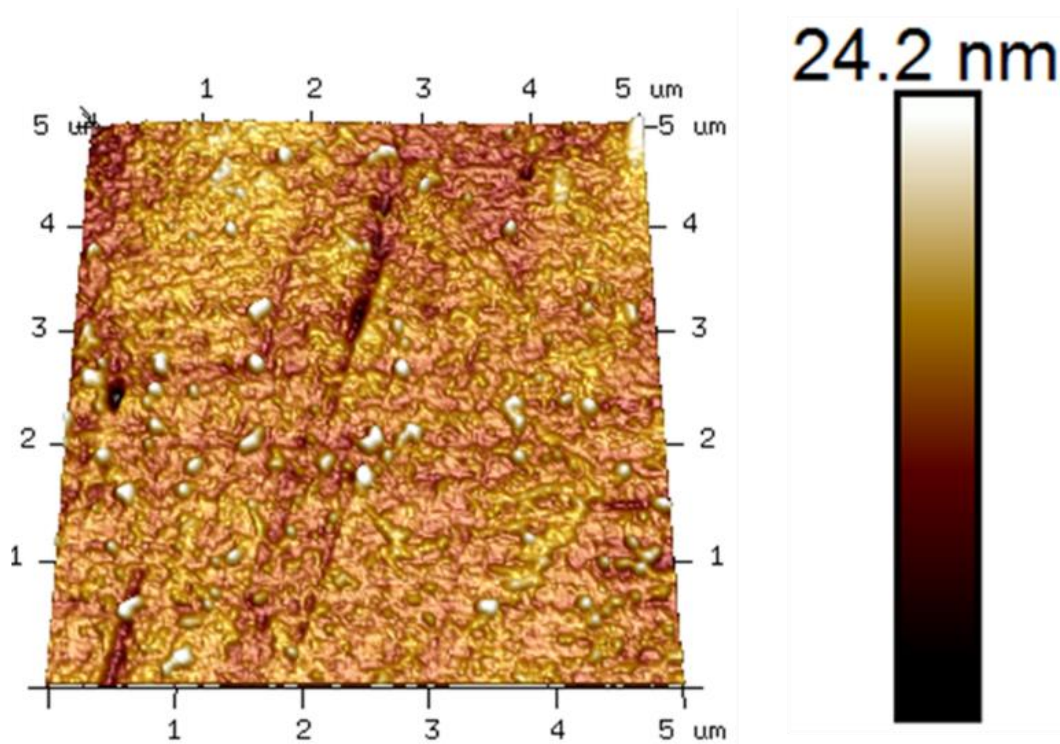

Figure S 1 AFM image of a stainless-steel substrate which was used as the substrate for a V_2O_5 thin film battery.

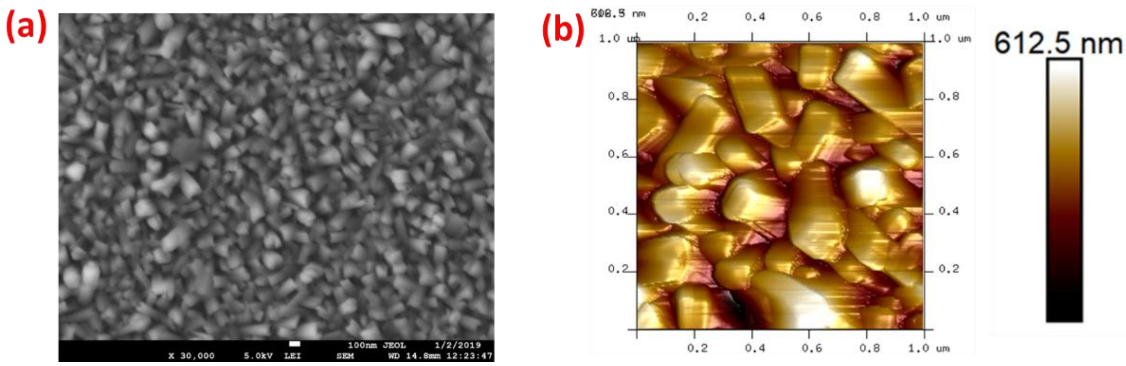

Figure S 2 V_2O_5 thin film fabricated through high temperature sputtering. (a) SEM image. (b) AFM image.

The film mentioned above were fabricated using the same parameters mentioned in experimental details expect the film were annealed at 350 °C during the sputtering process.

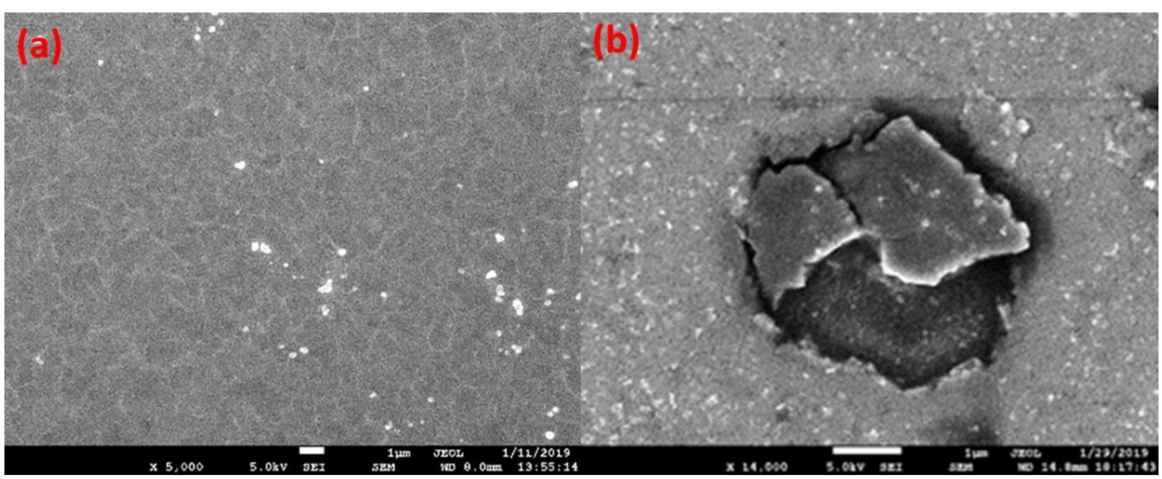

Figure S 3 SEM image of pristine V_2O_5 thin film with large field of view. (b) SEM image of V_2O_5 thin film after 50 cycles.

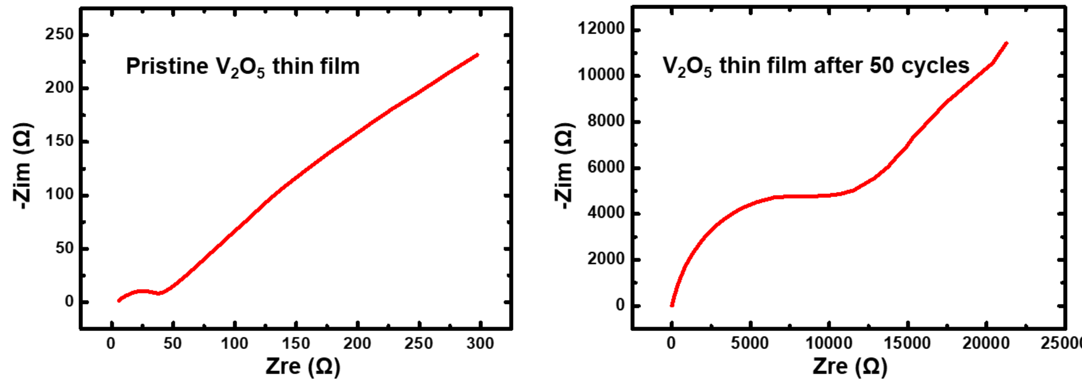

Figure S 4 EIS measurement before (left) and after (right) cycling

APPENDIX B

SUPPORTING INFORMATION FOR CHAPTER V

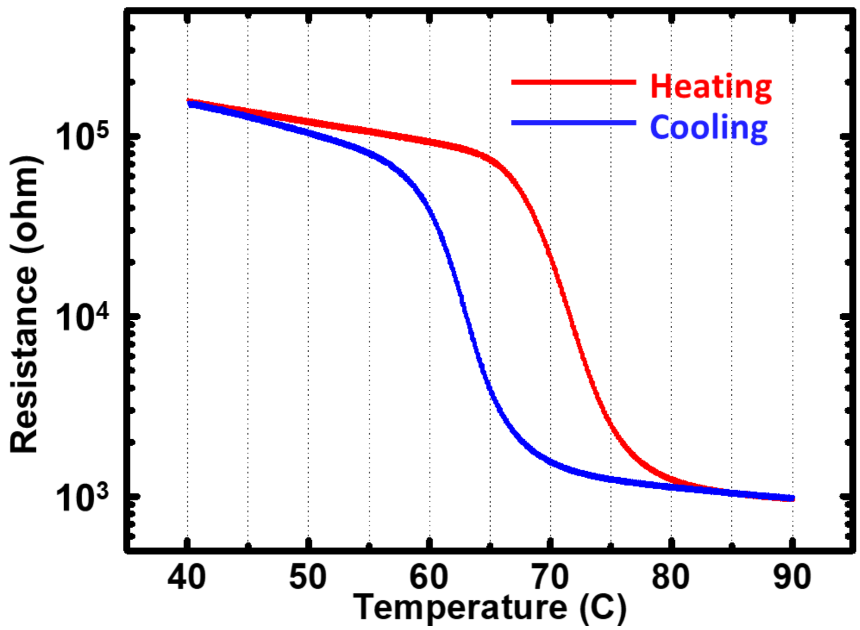

Figure S 5 Resistance measurement of polycrystalline VO2 deposited on SiO_2/Si

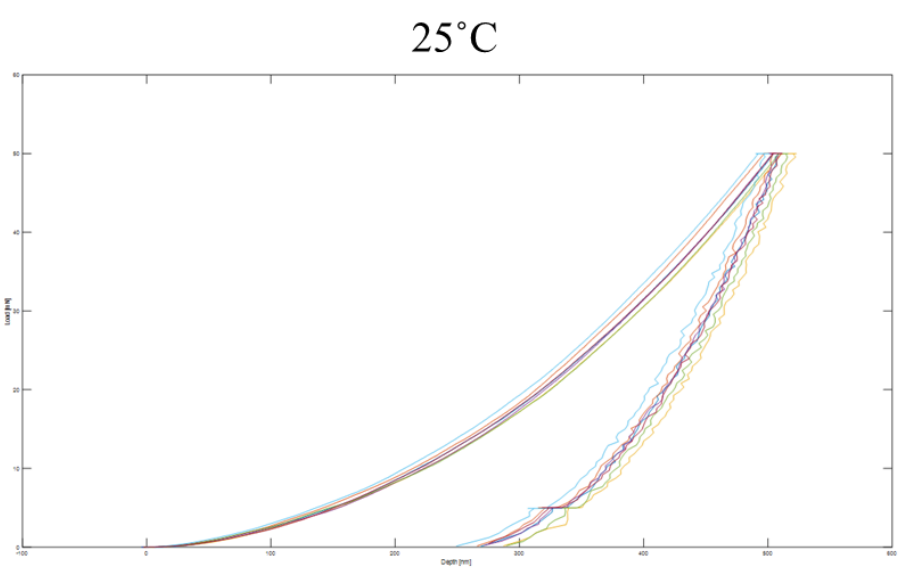

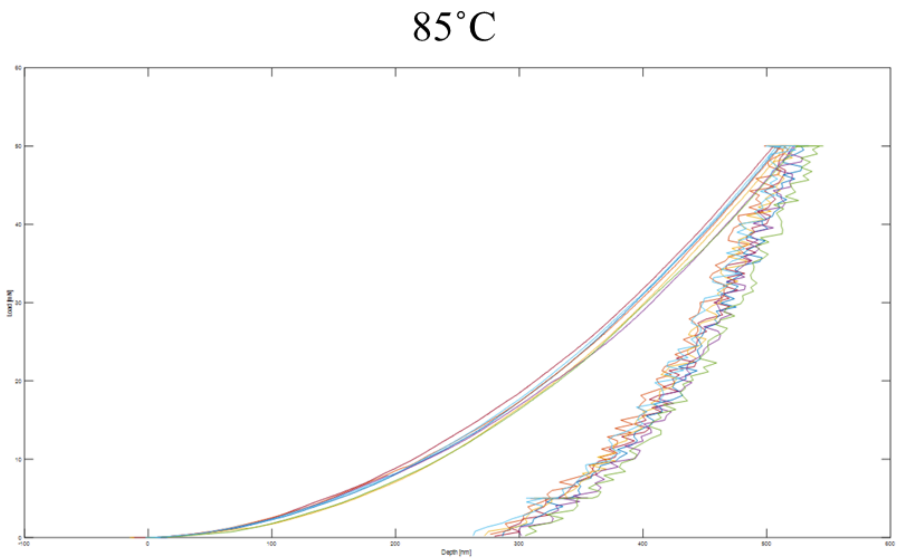

Figure S 6 Load and depth curve from indentation measurement at 25°C and 85°C

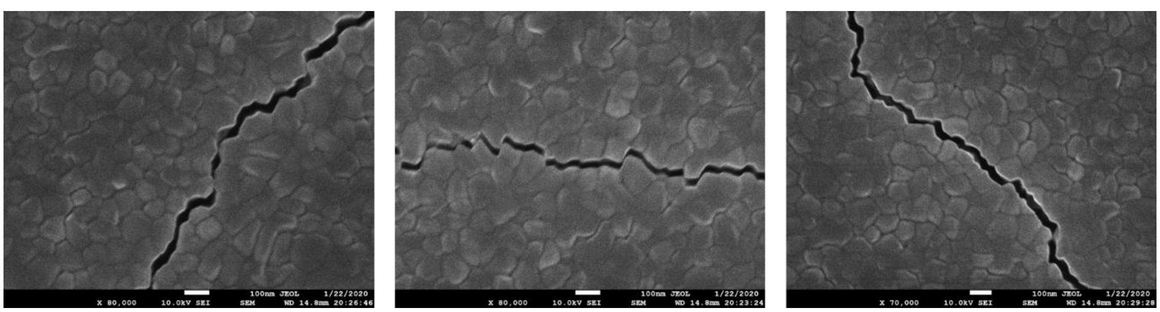

Figure S 7 SEM images of 1.6um thick VO_2 polycrystalline thin films